Coordination Chemistry Reviews 541 (2025) 216822

Contents lists available at ScienceDirect

Coordination Chemistry Reviews

journal homepage: www.elsevier.com/locate/ccr

Review

Morphology-controlled metal-organic frameworks for enhanced photocatalytic performance

Hamid Ali [a,b], Obaid Iqbal [c], Basem Al Alwan [d], Amal Abdulrahman [e], Yasin Orooji [f], Eida S. Al-Farraj [g], Muhammad Sadiq [h], Sajid Imran [i], Ahmed M. Abu-Dief [j,k], Dewu Yue [a,*], Asif Hayat [l,*]

[a] Information Technology Research Institute, Shenzhen Institute of Information Technology, Shenzhen 518172, China
[b] School of Resources and Environment, Shensi Lab, University of Electronic Science and Technology of China, Chengdu, China
[c] School of Materials Science and Engineering, Institutes of Physical Science and Information Technology, Anhui University, Hefei 230601, Anhui, China
[d] Department of Chemical Engineering, College of Engineering, King Khalid University, Abha 61421, Saudi Arabia
[e] Department of Chemistry, College of Science King Khalid University, Abha 61421, Saudi Arabia
[f] College of Geography and Environmental Sciences, Zhejiang Normal University 688 Yingbin Avenue, Jinhua, Zhejiang Province 321004, China
[g] Department of Chemistry, College of Science, Imam Mohammad Ibn Saud Islamic University (IMSIU), Riyadh, Saudi Arabia
[h] School of Computer Science, Shenzhen Institute of Information Technology, Shenzhen 518172. China
[i] School of Science and Engineering, The Chinese University of Hong Kong, Shenzhen, Guangdong 518172, China
[j] Department of Chemistry, Faculty of Science, Sohag University, Sohag 82524, Egypt
[k] Department of Chemistry, College of Science, Taibah University, P.O. Box 344, Madinah, Saudi Arabia
[l] Department of Chemistry, Lishui University, 323000 Lishui, China

ARTICLE INFO

Keywords:
Metal-Organic Frameworks
Different Synthesis Methods
Different Morphologies
Potential Photocatalytic Applications

ABSTRACT

The development of metal-organic frameworks (MOFs) has transforming the field of photocatalysis due to their tunable structures, high surface areas, and versatile functionalities. However, the systematic investigation of MOFs morphology and its profound influence on photocatalytic performance remains relatively unexplored. For the first time, this review comprehensively highlights the significant role of MOFs morphology in enhancing photocatalytic efficiency. Key factors affecting MOFs morphology, such as defects, porosity, precursors, solvents, surfactants, post-synthesis process, ligands, computational aspects, and various synthesis methods, including hydrothermal, microwave-assisted, solvothermal, and sonochemical techniques, are briefly discussed. Seventeen distinct MOFs morphologies are examined, including nanosheets, nanofilms, nanotubes, nanorods, nanowires, nanoparticles, quantum dots, hollow structures, hierarchical structures, sea urchin-like forms, monoliths, nanocages, core-shell, yolk-shell, aerogels, nanoflowers, and nanoribbons, with a focus on their role in optimizing photocatalytic performance. This review offers a pioneering analysis of the relationship between MOFs morphology and photocatalytic applications, which has not been previously reported. By evaluating the impact of morphology on charge transfer, light absorption, and active site exposure, this work provides new insights into the rational design of high-efficiency and cost-effective MOF-based photocatalysts. Ultimately, this review identifies key research directions for advancing MOFs photocatalysts for energy conversion and environmental remediation.

1. Introduction

The demand for energy has been dramatically increased due to the ever-increasing worldwide population and the recent fast economic expansion. This growth in energy use has increased dependence on conventional fossil fuels [1]. The ongoing reliance on fossil fuels poses serious environmental risks, including air and water pollution, and significantly contributes to the greenhouse effect, thereby accelerating global warming and climate change. The urgent environmental issues stressed the need to develop clean, sustainable, and renewable energy solutions to ease the harmful effects of traditional energy sources [2]. In this perspective, solar energy is an extremely promising solution.

* Corresponding authors.
E-mail addresses: yuedewu@sziit.edu.cn (D. Yue), asifncp11@yahoo.com (A. Hayat).

https://doi.org/10.1016/j.ccr.2025.216822
Received 17 December 2024; Accepted 13 May 2025
Available online 27 May 2025

Sunlight is almost infinite and plentiful, meeting world energy needs for billions of years. In contrast to fossil fuels, solar energy is a clean and renewable resource that generates no direct emissions of pollutants or greenhouse gases during its conversion [3]. Its usage can transform energy systems, facilitating a shift towards more efficient energy generation techniques. Solar energy technologies, such as photovoltaic cells, solar thermal systems, and solar-driven catalytic processes, provide significant potential for meeting increasing energy needs, while protecting the environment for future generations [4]. Photocatalysis is a technique that use solar energy to turn it into chemical energy using light-activated catalysts. This technology has significant potential for addressing important issues in energy production and environmental conservation [5]. Prominent uses of photocatalysis include photocatalytic hydrogen (H_2) production, photocatalytic CO_2 reduction reaction (CO_2RR), and the photosynthesis of small organic compounds. Photocatalysts facilitate the photolytic dissociation of water into hydrogen and oxygen, using solar energy, thus providing a sustainable and eco-friendly method for H_2 fuel generation [6]. Photocatalytic CO_2RR facilitates the conversion of CO_2, a significant greenhouse gas, into valuable fuels or chemical precursors, therefore overcoming energy requirements and environmental issues [7]. The photosynthesis of small organic molecules with sunlight imitates natural processes and presents opportunities for sustainable chemical synthesis. In recent decades, metal-organic frameworks (MOFs) have emerged as potential photocatalytic materials, attracting considerable attention owing to their elevated specific surface area, exceptional porosity, and structural adaptability [8]. The cooperative interaction between organic linkers and metal clusters in MOFs improves the light absorption via ligand-to-metal charge transfer and metal-to-ligand charge transfer [9]. Consequently, MOFs have shown better photocatalytic performance in many energy and environmental applications, surpassing traditional photocatalysts such as metal nitrides [10], metal oxides [11], quantum dots [12], and carbon-based materials [13]. Traditional photocatalysts often encounter issues like limited sunlight absorption, exciton recombination, and inadequate accessibility to active sites [14]. Nonetheless, MOFs mitigate these challenges by providing enhanced photon trapping productivity, increased surface area, and prolonged exciton lifetimes [15]. Furthermore, materials generated from MOFs are being investigated to improve their physical and chemical characteristics, hence expanding their range of applications. Beyond these intrinsic properties, recent advancements highlight that the morphology of MOFs plays a pivotal role in further enhancing their photocatalytic efficiency. Deng et al. [16] demonstrated that the hollow structural configuration of Co-MOF-74, produced by solvothermal transformation, enhances molecular mobility and the accessibility of active sites. The use of silver (Ag) nanoparticles improves shape, hence enhancing charge separation and electron transport, resulting in a photocatalytic CO_2RR activity that is up to 3.8 times greater than that of standard MOFs structures. Kuppusamy et al. [17] revealed that the monolith morphology of MOFs improves photocatalytic performance by assuring uniform dispersion of the MOFs and promoting pollutant interaction with active sites. This configuration facilitates accelerated pollutant degradation and enhances the stability of photocatalysts. Sun et al. [18] emphasize MOFs nanorod morphology for photocatalytic applications. Rod-like MoS_2 nanorods doped with $Bi_4O_5Br_2$ nanosheets in a p-n heterojunction structure increased photocatalytic activity. Light absorption and charge transfer are improved by nanorod, which enhances electron transport and charge separation. In addition, different process have been used to enhance the photocatalytic performance of MOFs, encompassing various synthesis techniques, the development of nanostructures, and the formation of heterojunctions [19,20]. Consequently, the investigation of innovative MOFs morphologies creates opportunities for enhancing the photocatalytic characteristics of these materials, rendering them more competitive in energy conversion and environmental remediation.

In this review, we examine the impact of MOFs on photocatalysis, highlighting how their tunable structures and high surface area enhance efficiency. For the first time, we comprehensively highlighted the significant role of MOFs morphology in enhancing photocatalytic efficiency. Key factors affecting MOFs morphology, such as defects, porosity, precursors, solvents, surfactants, post-synthesis process, ligands, computational aspects, and various synthesis methods, including hydrothermal, microwave-assisted, solvothermal, and sonochemical techniques, are briefly discussed. A detailed examination of 17 distinct MOFs morphologies is presented, encompassing nanosheets, nanofilms, nanotubes, nanorods, nanowires, nanoparticles, quantum dots, hollow structures, hierarchical structures, sea urchin-like forms, monoliths, nanocages, core-shell, yolk-shell, aerogels, nanoflowers, and nanoribbons, with a focus on their role in optimizing photocatalytic performance. This review provides a comprehensive analysis of these diverse MOFs morphologies synthesized through various chemical methods, filling a gap in existing research. The different MOFs morphologies aspects addressed in the review are presented in Scheme 1.

2. Key factors affecting MOFs morphology

Before exploring the role of different MOFs morphologies in enhancing photocatalytic applications, it is very important to first investigate the key factors that influence MOFs morphologies in detail. This foundational understanding provides a basis for systematically optimizing the structural and functional properties of MOFs. This section briefly overviews the important parameters influencing MOFs morphology and highlights their significant roles in improving photocatalytic performance.

2.1. *Effect of defects*

Defects in MOFs morphology significantly enhance photocatalytic applications by creating structural deviations that function as active sites for catalytic processes. Defects, like absent metal nodes, ligand vacancies, or lattice distortions, provide localized electronic states that magnify light absorption and promote charge carrier dynamics [21]. These defects promote the separation and transmission of photoexcited electrons and holes, decreasing recombination losses and enhancing photocatalytic performance [22]. Moreover, defect-laden MOFs often demonstrate elevated porosity surface area, facilitating the diffusion of reactants and the accessibility of active sites [23]. Defects facilitate bandgap adjustment, enabling MOFs to absorb light over a broader spectrum of wavelengths. Defects may optimize photocatalytic performance in water splitting, CO_2RR, and organic pollutant degradation by strategically designing MOFs [24]. For example, Guo et al. [25] showed that structural defects in Zr-MOFs (Zr-MOF-X) markedly improve CO_2 photoreduction during VL. Acid-regulated defect design resulted in defective Zr-MOF-X demonstrating enhanced N_2 uptake, increased pore sizes, and mesoporous structure compared to the defect-free NNU-28. Their results demonstrated that defects improve charge separation and promote the development of stable Zr(III) active sites, which interact with CO_2, thus improving photocatalytic productivity. Similarly, Dong et al. [26] improved Ni-MOF-74 to develop a strongly porous structure (Ni-74-Am) via temperature and solvent modulation (Fig. 1a). Ni-74-Am exhibited improved CO_2 photocatalytic efficiency due to the presence of additional unsaturated Ni active sites resulting from defects. The CO generation rate reached 1380 μmol g^{-1} h^{-1} with a selectivity of 94% under VL, surpassing the performance of most reported MOF-based photocatalysts. Characterization demonstrated enhanced electrons-holes separation and accelerated charge migration, indicating that Ni-74-Am is highly effective for CO_2RR. The SEM analysis indicates distinct catalyst morphologies: Ni-74-175 is characterized by smooth hexagonal rods (~20 μm), Ni-74-100 presents cluster-shaped blocks with rough edges, and Ni-74-Am exhibits fragmented structure (Fig. 1b, c). TEM analysis indicates the consistent distribution of Ni and O elements in the fragmented Ni-74-Am, despite variations in crystalline composition, morphology, and pore structure (Fig. 1d, e). Their research

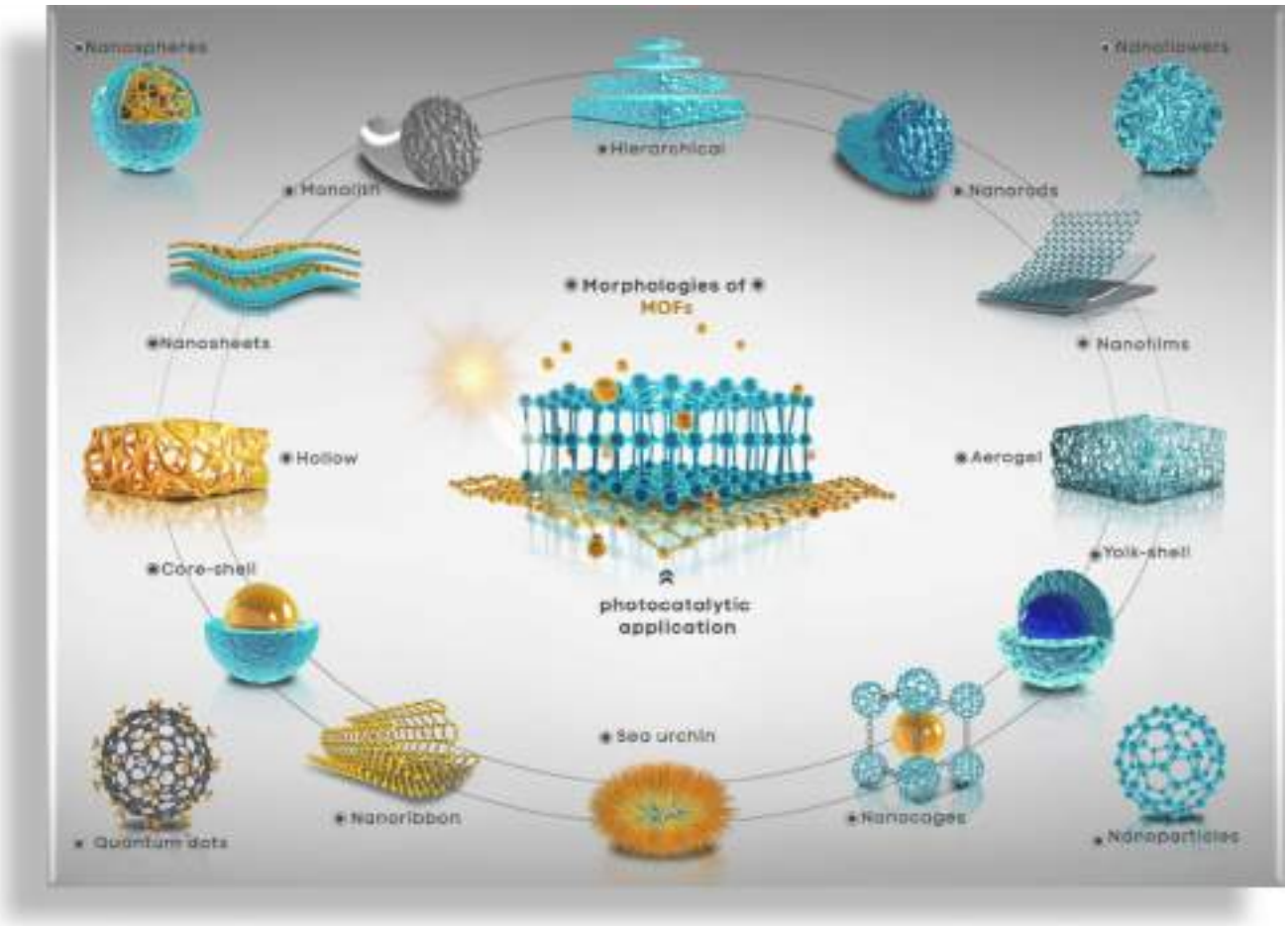

Scheme 1. Graphical illustration of the different aspects of MOFs morphologies addressed in this review.

enhances the engineering of defective MOFs and underscores their potential for sustainable energy and ecological uses.

2.2. Effect of porosity

Porosity significantly influences the photocatalytic efficiency of MOFs by affecting reactant diffusion, light absorption, and the availability of active sites [27]. Significant porosity, encompassing micro-, meso-, and macroporous structure, offers increased surface area and additional routes for the diffusion of reactants and products, thus improving mass transference productivity in photocatalytic processes [28]. Mesopores and macropores enhance the transport of large molecules and increase light penetration, resulting in improved light-matter interaction [29]. The interrelated porous systems increase the availability of active sites for photocatalytic processes, thus improving charge separation and transfer efficiency. Enhanced porosity in MOFs enhances reaction kinetics and reduces charge recombination, thus enhancing photocatalytic productivity [30]. For example, Lan et al. [31] synthesized porous Pt-doped heterojunctions (Pt-ZnO-Co_3O_4, Pt-ZnS-CoS, and Pt-Zn_3P_2-CoP) using ZnCo-ZIF as a template. The porous structure improves light utilization and reveals active sites, whereas Pt nanoparticles function as electron traps to improve charge separation and transfer. The materials demonstrated H_2 generation rates of approximately 7.80, 8.21, and 9.15 μmol h^{-1} g^{-1}, surpassing those of ZIF-based derivatives. Their study illustrates the significance of bimetallic MOF-based heterojunctions in facilitating effective WS. Similarly, Tian et al. [32] designed defect-rich Zn-doped NH_2-MIL-125(Ti) flakes (Zn_xTi_{1-x}-NML) using a one-step solvothermal approach (Fig. 1f). The doping of Zn^{2+} affected the growth of the (001) plane, whereas carboxylate ligands regulated surface texture and pore structure. The flake-shaped discs, measuring 0.5–1.0 μm in size and with thicknesses decreased from 100 to 40 nm, displayed multilevel holes resulting from in situ Zn^{2+} formation, which disrupted the NML structure (Fig. 1g, h). Compared to NML, the TEM analysis of $Zn_{0.15}Ti_{0.85}$-NML exhibited multilevel holes within the flakes, as demonstrated in the magnified views. It further revealed the absence of lattice fringes in both NML and $Zn_{0.15}Ti_{0.85}$-NML, aligning with the intrinsic properties of NML (Fig. 1i, j). Their research elucidates the correlation between the composition of MOFs and their catalytic productivity, offering valuable insights for developing advanced photocatalysts.

2.3. Effect of precursor

The effect of precursors is essential in shaping the morphology of MOFs to improve photocatalytic applications [33]. Precursors, such as metal sources, organic ligands, and solvents, significantly nucleation affect of MOFs, growth, and structural development [34]. Researchers may regulate the size, shape, and porosity of MOFs crystals by carefully selecting or modifying precursors, resulting in morphologies such as nanorods, nanoflakes, or hollow structures [35]. Particular metal salts or ligands can influence the formation of crystal planes, resulting in defects or hierarchical porosities that improve light absorption and boost charge separation [36]. Short-chain organic acids or capping agents serve as expansion modifiers by affecting continuous crystalline structure and incorporating distinct morphologies characterized by larger surface area and active sites [37]. The selection of precursors allows for precise adjustments in MOFs morphology, which enhances photocatalytic performance by improving the availability of catalytic active sites,

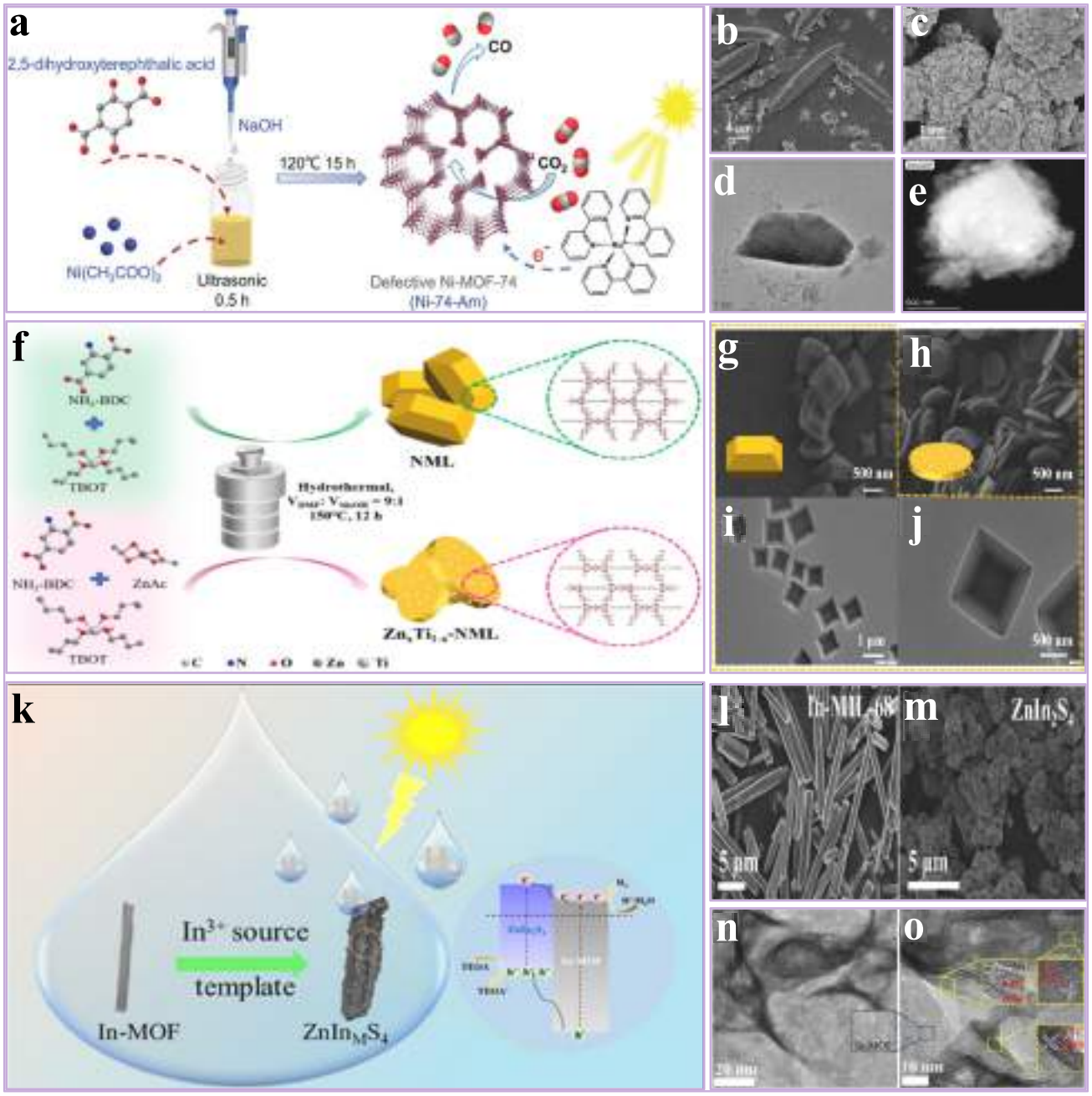

Fig. 1. (a) Synthesis process; (b, c) SEM; (d, e) TEM analysis of defective Ni-MOF-74 (Ni-74-Am), reproduced with permission from ref [26] Copyright © 2024, John Wiley and Sons. (f) Synthetic process; (g, h) SEM; (i, j) TEM analysis of NML and Zn_xTi_{1-x}-NML, reproduced with permission from ref [32] Copyright © 2024, American Chemical Society. (k) Synthetic process; (l, m) SEM; (n) TEM; (o) HRTEM analysis of $ZnIn_2S_4$-InMOF ($ZnIn_MS_4$) photocatalyst, reproduced with permission from ref [40] Copyright © 2024, American Chemical Society.

promoting charge transfer, and boosting light-harvesting productivity [38]. For example, Chen et al. [39] synthesized hollow carbon nanospheres incorporating Cu-TiO_2 by depositing a titanium precursor onto SiO_2@HKUST-1 core-shell nanospheres, subsequently subjecting the material to calcination and template etching. The hollow Cu-TiO_2/C nanospheres demonstrated effective photocatalytic H_2 performance and remarkable recyclability under visible light, presenting a novel approach for the synthesis of hybrid nanospheres for different applications. Similarly, Zang et al. [40] developed a unique $ZnIn_2S_4$-InMOF ($ZnIn_MS_4$) photocatalyst through an *in-situ* method, utilizing In-MOF as a template and In^{3+} as the precursor (Fig. 1k). The heterojunctions developed decreased charge recombination and enhance charge transfer dynamics, with In-MOF acting as an effective transport channel. $ZnIn_MS_4$ attained a cocatalyst-free HER rate of 70 μmol h^{-1} under VL ($\lambda >$ 420 nm), which is 3.2 times greater than that of $ZnIn_2S_4$, and exhibited remarkable stability for 16 hours. SEM and TEM analyses were used to investigate the morphology of the composites. In-MIL-68 displayed a smooth rod-shaped morphology, whereas $ZnIn_2S_4$ manifested as nanoflower structures. $ZnIn_MS_{4-2}$ exhibited a rectangular morphology characterized by flower-shaped $ZnIn_2S_4$ layers on the surface, thereby verifying the effective growth of a hierarchical structure (Fig. 1l, m). TEM analysis demonstrated the close junction between $ZnIn_2S_4$ and In-MOF, with the MOFs morphology maintained in $ZnIn_MS_4$ and distinct $ZnIn_2S_4$ nanosheets observed (Fig. 1n). HRTEM analysis indicated interplanar distances of 0.29, 0.32, and 0.41 nm associated with $ZnIn_2S_4$ planes, whereas the In-MOF was observed to be in an amorphous state

(Fig. 1o). Their study emphasizes the effectiveness of MOFs precursors as viable alternatives for the synthesis of advanced photocatalysts.

2.4. Effect of solvent

The photocatalytic efficiency of MOFs is directly influenced by the effect of solvent, which plays a significant role in regulating their morphology. Solvents influence the growth rate, crystallinity, and surface properties of MOFs by altering the solubility of precursors, coordination interactions, and nucleation process in the synthesis process [41]. Polar solvents facilitate accelerated nucleation and yield smaller particle sizes, whereas nonpolar solvents may stimulate anisotropic growth, leading to the formation of rod, plate, or layered morphologies [42]. The morphological changes influence light absorption, surface area, and the accessibility of active sites, thus boosting photocatalytic performance [43]. Moreover, the choice of solvent affects pore structure and defect growth, which are essential for effective charge separation and transport [44]. For example, Li et al. [45] synthesized vacancy-rich $Bi_4O_5Br_2$ (MBO-x) photocatalysts from Bi-MOF (CAU-17) using an improved double-solvent method. MBO-50, characterized by increased oxygen vacancies, attained 97% CIP and 90.1% HCHO removal in 60 min under visible light. The improved efficiency is due to efficient charge separation, decreased electron-hole recombination, and increased $\bullet O_2^-$ generation. Their research offers insights into the optimization of MOF-based photocatalysts for the degradation of pollutants. Similarly, Kaeosamut et al. [46] present solvent-responsive 2D cationic MOFs of Mn(II) (***1a***) and Zn(II) (***2a***) that exhibit single-crystal-to-single-crystal (SCSC) transformations into 3D MOFs (***1b*** and ***2b***). The transformations induced by solvents such as water, methanol, ethanol, and *n*-propanol involve synergistic interactions between solvent and ligand

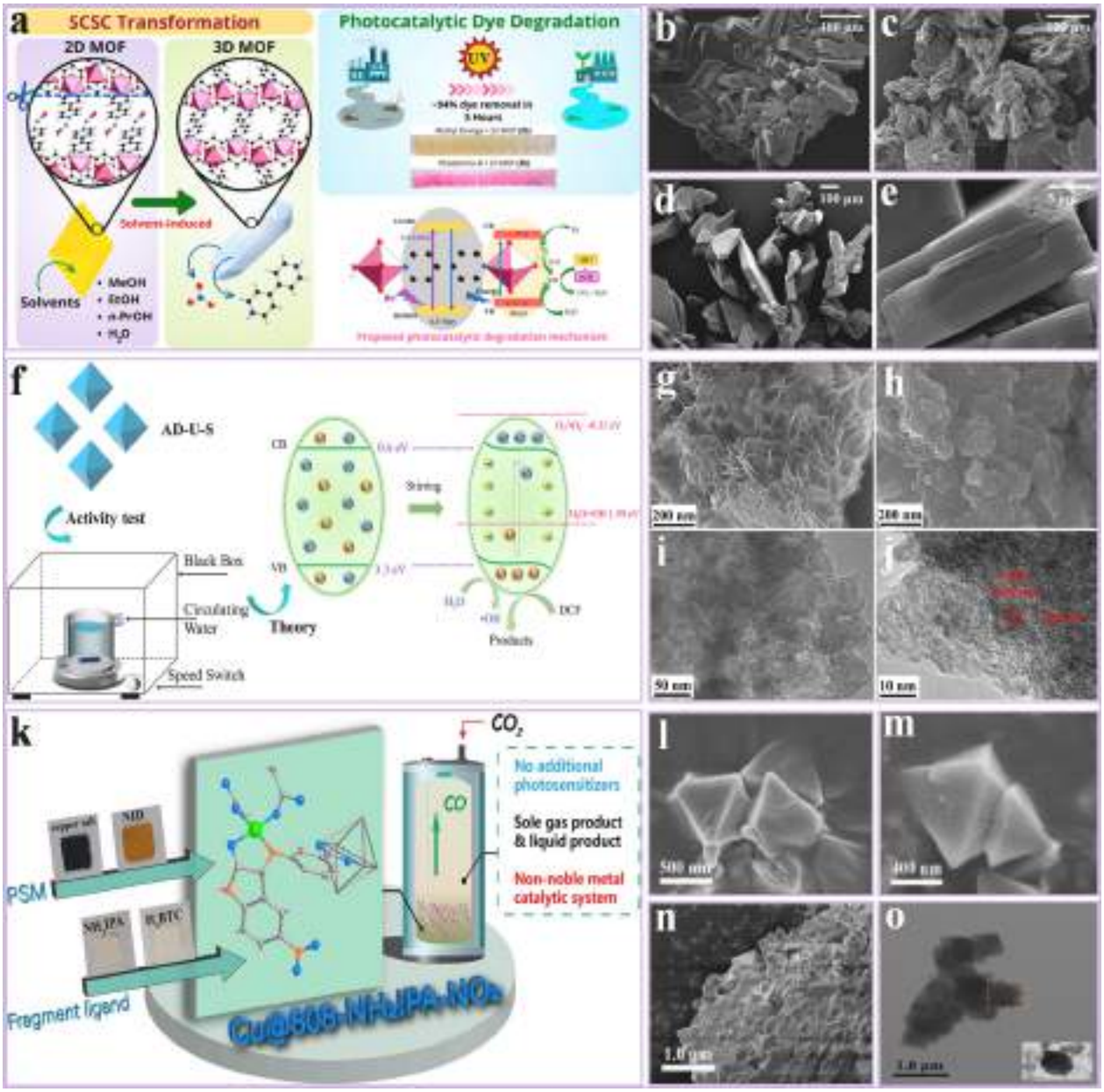

Fig. 2. (a) Synthesis process; (b–e) SEM analysis of 2D cationic MOFs of Mn(II) (***1a***) and Zn(II) (***2a***), reproduced with permission from ref [46] Copyright © 2023, American Chemical Society. (f) Synthetic process; (g, h) SEM; (i, j) HRTEM analysis of adenine-UiO-66 (AD-U) MOFs, reproduced with permission from ref [51] Copyright © 2024, Elsevier. (k) Synthetic process; (l–n) SEM; (o) TEM analysis of Cu@808-NH_2IPA-NO_2, reproduced with permission from ref [59] Copyright © 2024, Elsevier.

substitution. The synthesis of 2D MOFs was obtained swiftly through a microwave-heating method (Fig. 2a). SEM analysis of Mn-MOF (***1a***) and Zn-MOF (***2a***) before and after immersion in DI water demonstrated crystal fragmentation during their conversion to 3D structures (***1b*** and ***2b***). The micrographs validate changes in their physical characteristics and elemental composition, emphasizing the SCSC transformation process (Fig. 2b–e). Their research demonstrated that first-principles calculations assign the substantial photocatalytic performance of ***2b*** to its favorable band-edge position for redox reactions.

2.5. Effect of surfactants

In order to modify the morphology of MOFs and greatly improve their photocatalytic efficiency, the effect of surfactants is essential. Surfactants function as structure-directing agents by controlling crystal expansion, size, and surface characteristics during synthesis process [47]. The formation of specific morphologies, including nanosheets, nanorods, and hierarchical structures, is controlled, enhancing the surface area of MOFs, porosity, and light-harvesting capabilities [43]. Surfactants also affect the exposure of reactive facets and active sites, which improves charge separation and transfer efficiency [48]. Surfactants improve the photocatalytic performance of MOFs by enhancing their morphology and surface features, facilitating applications in pollutant degradation, HER, and CO_2RR [49]. For example, Molina et al. [50] showed that mesoporosity produced by surfactants improves the efficiency of nanocrystalline MOFs. The combination of NH_2-MIL-53(Al) and the cationic surfactant CTA^+ facilitated the formation of a hierarchically porous material via fast precipitation and facile ethanol washing. The NH_2-MIL-53(Al) demonstrated significant intercrystalline mesoporosity, achieving over 90% removal of 25 ppm bisphenol A (BPA) from water within 10 min at ambient temperature. Similarly, Li et al. [51] examined the effects of surfactants on adenine-UiO-66 (AD-U) MOFs, synthesizing AD-U-S using sodium dodecyl benzene sulfonate (SDBS) and AD-U-C with cetyltrimethylammonium bromide (CTAB) (Fig. 2f). Diclofenac sodium (DCF) was the target pollutant, and AD-U-S demonstrated degradation performance of 98% within 30 min, surpassing AD-U-C, which achieved 78% effectiveness. The reaction steady-state rate of AD-U-S was 3.5 times greater, attributed to its increased surface area, superior ferroelectric characteristics, improved oxidation capacity, and improved charge transfer effectiveness. Hydroxyl radicals (•OH) and holes (h^+) are identified as the primary active sites. SEM analyses indicate that surfactants substantially impact the morphology and elemental distribution of materials. AD-U-S (0.30), modified with the anionic surfactant SDBS, displays a regular flower-flake structure, whereas AD-U-C (0.30), improved with the cationic surfactant CTAB, presents an irregular block-like structure (Fig. 2g, h). The HRTEM analysis validates the lamellar structure of AD-U-S (0.30), exhibiting a lattice spacing of 0.299 nm corresponding to the (011) plane of UiO-66. The nanosheet morphology of AD-U-S (0.30) improves deformation, thereby promoting piezoelectric potential and efficient electron-hole separation (Fig. 2i, j). Their work demonstrates promising pathways for the advancement of piezocatalytic technology in wastewater treatment.

2.6. Effect of post-synthesis treatments

Post-synthesis treatments are essential for tailoring the morphology of MOFs to improve their photocatalytic applications. The treatments, such as thermal annealing, solvent exchange, chemical etching, and defect engineering, facilitate precise control over crystal size, porosity, and surface design [52]. Thermal treatments effectively eliminate residual organic linkers, create vacancies, or transform MOFs into derived materials that exhibit improved light absorption and charge transport characteristics [53]. Solvent exchange techniques can alter the intercrystalline structure, resulting in hierarchical porosity that enhances mass transfer in photocatalysis [54]. Chemical etching modifies MOFs morphologies, increasing active site availability and improving catalytic efficiency [55]. Defect engineering, using techniques like ligand exchange or doping, enhances charge separation productivity by creating active sites [56]. Post-synthesis treatments enhance the structural properties of MOFs, electronic, and morphological characteristics, thus improving their photocatalytic performance for pollutant degradation, water splitting (WS), and energy conversion applications [57]. For example, Zhao et al. [58] synthesized MOF-808-SIPA through a post-synthesis exchange method, incorporating sulfonic acid and carboxyl functional groups. The material demonstrated an adsorption capacity of 287.1 mg g^{-1} for moxifloxacin hydrochloride, surpassing that of MOF-808-AA, which exhibited a 174.6 mg g^{-1} capacity. MOF-808-SIPA demonstrated fast adsorption within approximately 30 minutes, exhibited pH resistance, and displayed effective regeneration capabilities. Hydrogen-bond interactions were significant to its enhanced efficiency, providing a structure for the formation of effective MOF-derived adsorbents. Similarly, Lian et al. [59] devised an affordable strategy to enhance the visible light consumption of Zr-MOFs for carbon capture and transformation through a multi-component post-synthesis modification (PSM) (Fig. 2k). The incorporation of an economical photosensitizer and copper ions into MOF-808 resulted in a CO yield of 236.5 μmol g^{-1} h^{-1} and HCOOH production of 993.6 μmol g^{-1} h^{-1}, achieved without the use of noble metals. Utilizing MOF-808 as the parent structure Cu@808-NH_2IPA-NO_2, Cu@808-NH_2IPA-H, and Cu@808-NH_2IPA-OCH_3 were produced through a three-step chemical modification process. SEM and TEM analysis validated the uniform distribution of NH_2IPA within the stable structure following the substitution of 15% of the original ligand. The post-modified Cu@808-NH_2IPA-NO_2 maintained its octahedral morphology while displaying an increased surface roughness, presumably resulting from chemical grafting in the PSM process (Fig. 2l–o). Their study offers significant insights into CO_2 photoreduction processes and emphasizes the possible uses of MOFs in photocatalytic applications.

2.7. Effect of ligands

Ligands significantly influence the morphology and photocatalytic performance of MOFs by affecting their porosity, electronic structure, and stability [60]. The length and elasticity of the structure influence its openness, which in turn affects mass transfer and reactant diffusion. Additionally, functional groups such as $–NH_2$, $–NO_2$, and –OH modulate band gaps, charge separation, and light absorption characteristics [61]. π-conjugated ligands improve visible-light harvesting and charge transfer, thereby enhancing photocatalytic efficiency [62]. Furthermore, hydrophilic ligands enhance interactions with aqueous reactants in applications such as WS and pollutant degradation. Mixed-ligand strategies create hierarchical porosity, which improves reactant accessibility [63]. Through the precise selection and modification of ligands, MOFs can be designed for enhanced photocatalytic applications, such as CO_2RR, water treatment, and the degradation of organic pollutants [64]. For example, Wang et al. [65] developed a series of isostructural MIL-125-Ti MOFs with different ratios of terephthalic to amino-terephthalic acid and assessed their photostability and photocatalytic hydrogen evolution rate (HER) efficiency. Research indicated that triethanolamine caused corrosion of the MOFs under photocatalytic conditions, while methanol functioned effectively as a hole scavenger. The MIL-125-Ti/methanol system demonstrated a photocatalytic activity that was 45 times greater than that of NH_2-MIL-125-Ti when subjected to broad UV irradiation (Fig. 3a). SEM analysis indicates that both MIL-125-Ti and NH_2-MIL-125-Ti display a circular plate-like morphology, aligning with prior findings. Analysis of Brunauer-Emmett-Teller (BET) surface area and t-plot micropore volume reveals that NH_2-MIL-125-Ti exhibits a marginally lower pore volume of 0.53 cm^3/g and surface area of 1243 m^2/g in comparison to MIL-125-Ti, which has a pore volume of 0.60 cm^3/g and a surface area of 1413 m^2/g. The reduction is ascribed to the amino group in NH_2BDC, which directs toward the pore interior,

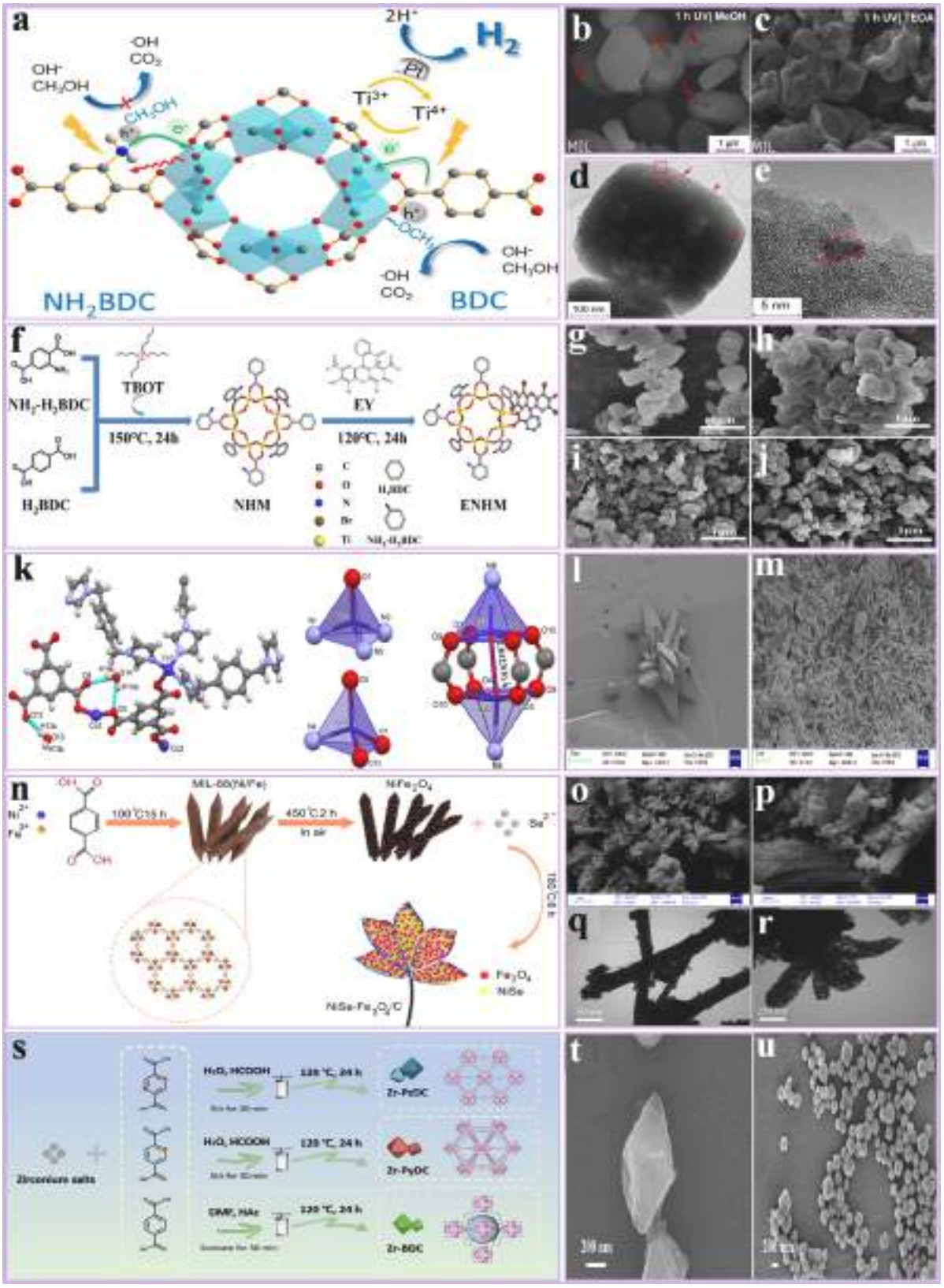

Fig. 3. (a) Proposed synthesis and photocatalytic mechanism; (b, c) SEM; (d, e) TEM analysis of MIL-125-- Ti-xNH_2, reproduced with permission from ref [65] Copyright © 2021, Elsevier. (f) Synthesis process; (g–j) SEM analysis ENHM, reproduced with permission from ref [66] Copyright © 2024, Elsevier. (k) Representation of the asymmetric unit of complex (1); (l, m) FESEM analysis of as-prepared complex (1), reproduced with permission from ref [67] Copyright © 2022, Elsevier. (n) Synthesis process; (o, p) SEM; (q, r) TEM analysis of bi-metal MOF-derived NiSe-Fe_3O_4/C, reproduced with permission from ref [72] Copyright © 2023, Elsevier. (s) Synthesis process; (t, u) TEM analysis of Zr-MOFs, reproduced with permission from ref [73] Copyright © 2024, Elsevier.

resulting in a slight constriction of the pore structure (Fig. 3b, c). TEM analysis reveals a uniform deposition of Pt nanoparticles (~3 nm) on the surfaces of both MOFs, as evidenced by the dark spots observed. Although platinum predominantly occupies the surface of the MOFs due to its size, the possibility of some deposition within the MOFs cannot be excluded. The nanoparticles establish close interfaces with the MOFs, and the measured lattice distance of 0.226 nm, which corresponds to the Pt (111) plane, verifies the metal state of Pt (Fig. 3d, e). Their results showed that the mixed-ligand MOFs exhibited a dual-excitation route, which introduced novel states and transitions, thereby enhancing the comprehension of MOF-derived photocatalysis. Similarly, Liu et al. [66] introduced a multi-ligand approach for the development of MOF-based photocatalysts, successfully integrating a three-ligand Ti-MOF (ENHM) utilizing NH_2-H_2BDC, H_2BDC, and Eosin Y through a hydrothermal approach. The interaction between –NH_2 and –H substituents facilitates electron transfer from organic ligands to metallic nodes, whereas Eosin Y boosts visible-light absorption, thereby enhancing the production of photoinduced electrons. ENHM-2 had the greatest HER (2.15 μmol g^{-1} h^{-1}), outperforming dual- and single-ligand alternatives. ENHM was synthesized via a hydrothermal method using NH_2-H_2BDC, H2BDC, and Eosin Y. NH_2-H_2BDC and H_2BDC were dispersed in DMF/MeOH, after which TBOT was added to produce NHM. Subsequently, EY was incorporated, leading to the formation of the three-ligand ENHM through a second hydrothermal method. Samples of ENHM have been created with different EY/NHM ratios of 1:7, 3:7, and 5:7, designated as ENHM-1, ENHM-2, and ENHM-3. NM, NHM, and ENM have been produced for comparative analysis (Fig. 3f). SEM analyses indicate that pristine NM displays a lamellar morphology characterized by a smooth surface and a diameter of approximately 700 nm. The dual-ligand NHM exhibits a structure comparable to NM, suggesting that the addition of H_2BDC has minimal effect on morphology. ENM and the three ENHM samples maintain a lamellar structure. However, they exhibit reduced size and rougher surfaces, likely resulting from the partial substitution of Eosin Y for NH_2-H_2BDC and/or H_2BDC ligands (Fig. 3g–j). Their research illustrates that the multi-ligand strategy presents a novel method for the development of highly effective microporous photocatalysts. Furthermore, Somnath et al. [67] developed a novel MOFs ($[Co_3(BTC)_2(Bimb)_{2.5}]\cdot 2H_2O)n$ (1), using elemental evaluation, single-crystal X-ray diffraction, and multiple spectroscopy techniques. The structure comprises a 3D system featuring trinuclear cobalt clusters interconnected by BTC^{3-} and Bimb ligands. Luminescence studies indicated emission within the 441-461 nm range, while thermal decomposition resulted in the development of 20 nm Co_3O_4 nanoparticles. Photocatalytic experiments indicated that complex (1) efficiently decomposed several dyes, such as Fluorescein, Rhodamine B, and Congo Red, under UV light, achieving degradation rates of up to 91.7% for Fluorescein after 135 minutes (Fig. 3k). FESEM analysis of the synthesized ($[Co_3(BTC)_2(Bimb)_{2.5}]\cdot 2H_2O)n$ (1) demonstrated a dendritic morphology, predominantly featuring globular nanoparticles with sizes under 50 nm (Fig. 3l, m). EDAX analysis verified a 1:1 ratio of cobalt to oxygen, suggesting compositional homogeneity in the Co_3O_4 nanoparticles. Their research indicated that complex (1) successfully photodegraded multiple dyes, achieving degradation rates of 91.7% for Fluorescein and 77.5% for Eriochrome Black T, while other dyes exhibited lower degradation rates. The complex demonstrated significant reusability, productivity, and cost-effective adsorption, positioning it as a viable option for the treatment of dye-contaminated wastewater.

2.8. Computational aspects

Computational methods are essential for analyzing and forecasting the morphological impacts of MOFs on their photocatalytic efficiency. DFT calculations facilitate the analysis of electronic structures, band gaps, and charge transfer dynamics, thereby supporting the rational development of MOFs with enhanced light absorption and charge separation properties [68]. Molecular dynamics models offer insights into the stability and versatility of various MOFs morphologies under various conditions, including solvent interactions and thermal fluctuations [69]. Computational fluid dynamics (CFD) facilitates the assessment of mass transfer and diffusion characteristics in porous structures, which is essential for the accessibility of reactants in photocatalysis [70]. Moreover, machine learning and higher-throughput screening enable the identification of new ligand-metal combinations that improve MOFs morphology for targeted applications, including CO_2RR and pollutant degradation [71]. Integrating computational modeling with experimental synthesis allows researchers to optimize MOFs structures, enhancing photocatalytic productivity, stability, and scalability. For example, Rashid et al. [72] introduced a solvothermal approach for the synthesis of flower-like NiSe-Fe_3O_4/C S-scheme heterostructures using a Ni/Fe-MOF sacrificial template aimed at the photocatalytic degradation of tetracycline (TC) within a spiral-shaped microfluidic photoreactor. The findings from electrochemical, optical, microscopic, and DFT analyses demonstrated that the NiSe-Fe_3O_4/C heterostructure improved light absorption and charge separation, resulting in over 85% TC degradation within 15 minutes. The mechanism emphasized the involvement of reactive oxygen species (•OH and $\bullet O_2^-$) in the process. NiSe-Fe_3O_4/C was preparad through the combination of Fe/Ni oxide with ethanol and H_2SeO_3, subsequently followed by the gradual addition of $N_2H_4\cdot H_2O$. The mixture underwent hydrothermal treatment at 180°C for 6 hours, followed by centrifugation and drying at 70°C for 24 hours (Fig. 3n). The surface morphologies and structural formations of MIL-88(Ni/Fe) and NiSe-Fe_3O_4/C were examined using FE-SEM and TEM techniques. MIL-88(Ni/Fe) displayed a smooth, spindle-shaped, and consistent structure. Following calcination and chemical selenization, the NiSe-Fe_3O_4/C sample showed smooth, lamella-like particles embedded within a carbon sheath. TEM analysis verified morphological changes, indicating that following calcination, the NiFe-MOF maintained a hexagonal rod-like shape, which subsequently changed into a flower-like structure after selenization. The NiSe and Fe_3O_4 nanoparticles were uniformly distributed within the carbon sheath, with close surface contact essential for minimizing charge carrier recombination (Fig. 3o–r). Their study demonstrates the efficiency of interfacial engineering in improving the photocatalytic activity of heterostructures. Their study introduces a novel method for creating abundant, cost-effective, and stable catalysts derived from bi-MOFs for environmental applications. Similarly, Chen et al. [73] synthesized three MOFs, namely Zr-PzDC, Zr-PyDC, and Zr-BDC, utilizing distinct organic ligands to modulate the internal electric field, thereby improving N_2 photofixation. DFT calculations indicated that Zr-PzDC, featuring a pyrazine ring, exhibited the highest charge density variation, thereby enhancing charge separation and broadening the photoresponse range. Zr-PzDC demonstrated the highest N_2 photofixation efficiency, achieving 143.51 μmol·g^{-1}·h^{-1} under ambient conditions. MOFs employ ligand-to-metal charge transfer (LMCT), facilitating the migration of photoinduced electrons to the metal center for reduction. The resultant inhomogeneous charge distribution generates an internal electric field, which facilitates charge separation and transfer. Three Zr-MOFs with differing nitrogen content were produced using the hydrothermal approach to investigate the impact of ligand charge density variations attributed to nitrogen sites (Fig. 3s). SEM images indicate that Zr-BDC displays significant crystallinity and a consistent octahedral morphology, whereas Zr-PzDC and Zr-PyDC demonstrate lower crystallinity. This is consistent with XRD results and is ascribed to the electron-withdrawing corrosion by nitrogen in pyrazine and pyridine rings, as well as intrachain hydrogen bonding couplings in H_2PzDC ligands (Fig. 3t, u). Their research presents a novel approach to the design of MOFs photocatalysts for nitrogen fixation.

2.9. Effect of different synthesis methods

2.9.1. Hydrothermal synthesis

Hydrothermal synthesis is essential for optimizing the photocatalytic

performance of MOFs by regulating their structure. Adjusting synthesis parameters, including temperature, pressure, reaction time, and precursor concentration, allows hydrothermal methods to produce MOFs with precise shapes, sizes, and crystalline structure [74]. This method facilitates the development of crystalline and consistent MOFs morphologies, including nanosheets, nanorods, and hierarchical structure, which are vital for enhancing light-harvesting efficiency and increasing surface area [43]. The increased surface area and customized morphology promote boosted charge separation, productive mass transfer, and greater accessibility of active sites, thus enhancing

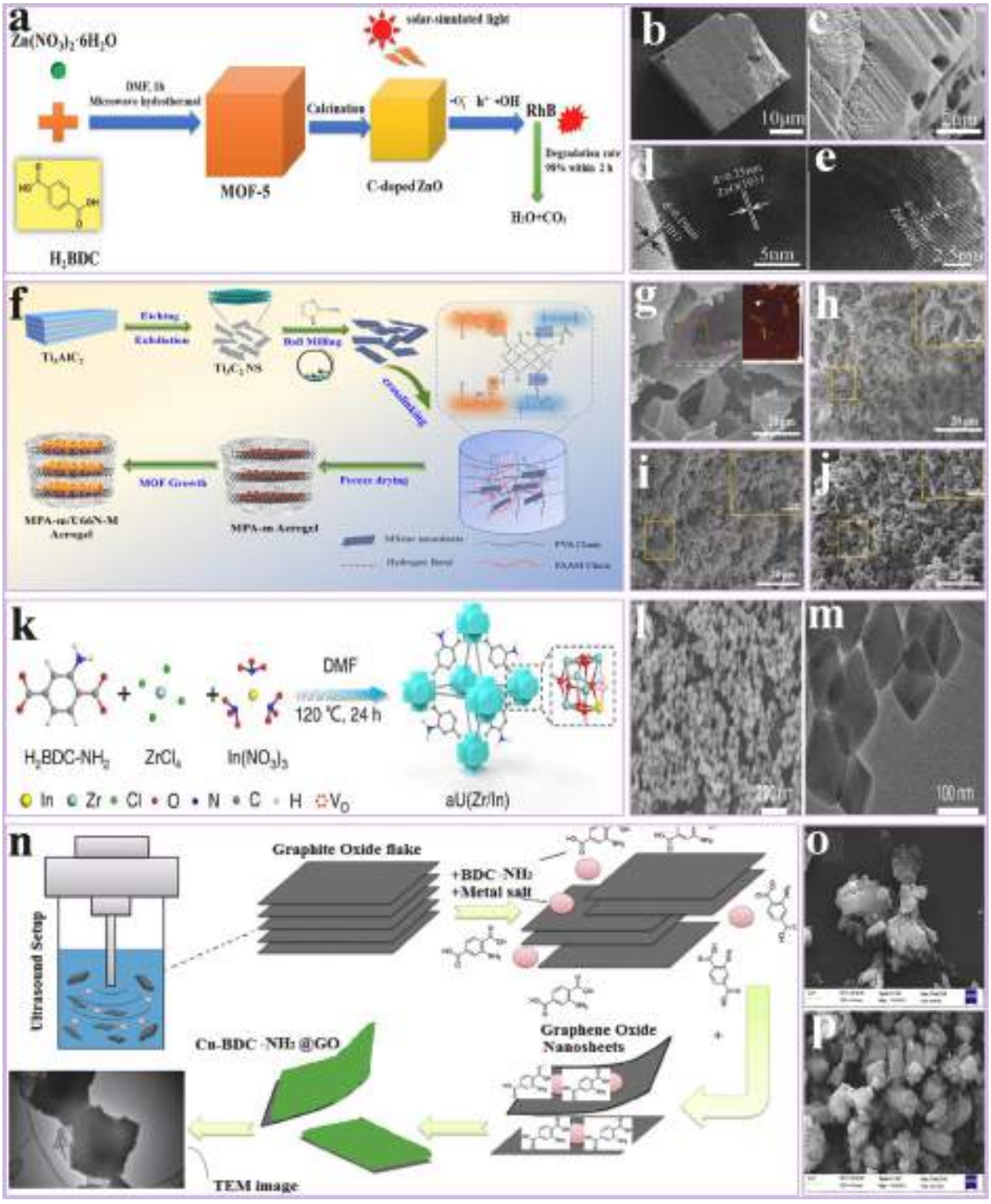

Fig. 4. (a) Synthesis process; (b, c) SEM; (d) TEM; (e) HRTEM analysis of M-MOF-5 reproduced with permission from ref [78] Copyright © 2020, American Chemical Society. (f) Synthetic process; (g–j) SEM analysis of MPA-m/U66N-M, reproduced with permission from ref [84] Copyright © 2023, Elsevier. (k) Synthetic process; (l) TEM; (m) HRTEM of as-prepared aU(Zr/In)-3, reproduced with permission from ref [91] Copyright © 2023, Elsevier. (n) Synthesis process; (o, p) SEM analysis of Cu-BDC-NH_2@GO, reproduced with permission from ref [98] Copyright © 2019, Elsevier.

photocatalytic performance [75]. Hydrothermal synthesis facilitates the addition of dopants or functional groups, further refining the electronic structure and improving the capacity of MOF to absorb visible light and enhance redox reactions [76]. For example, Zheng et al. [77] developed nitrogen-doped TiO_2/ZrO_2 composites using Ti/Zr bimetallic MOFs precursors through a one-step hydrothermal method, subsequently undergoing pyrolysis at 600°C. The composites, exhibiting uniform nitrogen doping, kept the disk morphology characteristic of the MOFs. The composites demonstrated reduced electron-hole recombination and effective photodegradation of methylene blue (93.2% in 80 minutes), tetracycline (86.3%), and phenol (72.4%) when exposed to UV light. Quenching tests and ESR indicated that •OH radicals are the primary active sites, and the composites demonstrated significant stability and versatility for use in photocatalytic processes. Similarly, Wang et al. [78] synthesized C-doped ZnO particles by calcining MOF-5 at 500°C. The material maintained its cubic shape, and the C-doping in ZnO was verified. The C-doped ZnO demonstrated a 98% degradation capacity for Rhodamine B (RhB) within 2 hours under VL, surpassing the performance of C-doped ZnO synthesized through conventional hydrothermal process (Fig. 4a). The SEM analysis indicates that the as-prepared M-MOF-5 exhibits a well-defined cubic structure with a side length of approximately 25 μm. Post-calcination, the samples maintain a cubic morphology while exhibiting increased porosity and roughness, with side lengths measuring approximately 15 μm for M-ZnO-500 and 10 μm for M-ZnO-550. M-ZnO-500 exhibits partially cracked surfaces, whereas M-ZnO-550 presents microspheres and irregular cubes. The calcination temperature has an important effect on morphology (Fig. 4b, c). TEM analysis indicates that M-ZnO-500 comprises approximately 15 nm nanoparticles (Fig. 4d), while HRTEM analysis demonstrates distinct interplanar spacings of 0.29, 0.25, and 0.19 nm, thereby verifying the production of C-doped ZnO (Fig. 4e). Their study introduces a successful approach for synthesizing C-doped ZnO, characterized by decreased reaction time and uniform morphology, indicating its potential utility in environmental remediation applications.

2.9.2. Microwave-assisted synthesis

Microwave-assisted synthesis is a key factor in regulating the morphology of MOFs to improve their photocatalytic performance. This method provides efficient and constant heating, which enhances nucleation and crystallization operations, generating the MOFs with precise and adjustable morphologies [79]. Controlled microwave irradiation facilitates the precise influence of particle size, shape, and crystallinity, which are essential for enhancing light absorption, charge separation, and surface area [80]. Microwave-assisted synthesis effectively minimizes reaction time, energy usage, and the necessity for severe reaction conditions, thereby presenting an effective and sustainable methodology [81]. The resulting MOFs frequently demonstrate boosted photocatalytic performance, attributed to their optimized morphology, increased surface-to-volume ratio, and consistent distribution of active sites, which facilitate modified light absorption and accelerated redox reactions [82]. For example, Liu et al. [83] devised a microwave-assisted technique for synthesizing 2D Zr-MOF UiO-67 nanosheets (UiO-67 NS) and Au/UiO-67 NS nanocomposites. The composites demonstrated significant catalytic capacity, converting 4-nitrophenol to 4-aminophenol in 100 seconds using merely 20 equivalents of sodium borohydride. Their results indicated a 0.48 eV reduction in Au 4f binding energy in Au/UiO-67 NS, which improves the catalytic efficiency relative to Au@UiO-67 OM. Similarly, Yu et al. [84] devised a microwave-assisted method to synthesize MXene/MOF aerogel photocatalysts aimed at enhancing acetone photodegradation under high humidity conditions (Fig. 4f). The N-metal bi-bonding at MXene/MOF interfaces improved light absorption, facilitated the synthesis of $•OH/•O_2^-$ radicals, and boosted electron-hole separation. The photocatalyst demonstrated 97.3% acetone degradation under 80% humidity, exhibiting rate constants 10 to 104 times greater than existing photocatalysts and approximately 95% total organic carbon removal within 60 minutes. Fig. 4g–j illustrates the structural characteristics of pure U66N, Ti_3C_2 NS, and MPA/U66N aerogel composites. Pure U66N displayed a consistent octahedral structure with dimensions ranging from 150 to 200 nm. SEM analysis validated the effective synthesis of ultra-thin Ti_3C_2 flakes through the etching and stripping of Ti_3AlC_2 powders. Their study exhibited significant stability across five cycles, presenting a viable approach for volatile organic compounds (VOCs) degradation in humid environments.

2.9.3. Solvothermal synthesis

Solvothermal synthesis is essential for regulating the morphology of MOFs, thereby improving their photocatalytic performance. This method employs elevated temperature and pressure within a designated solvent, enabling the accurate control of nucleation, expansion, and crystallization methods [85]. Changing reaction parameters, such as temperature, time, solvent type, and precursor concentration, facilitates the solvothermal synthesis of MOFs with distinct morphologies [86]. The solvent significantly influences the dimension of MOFs, shape, and porosity by organizing with metal ions or facilitating anisotropic growth [87]. The customized morphologies considerably improve photocatalytic performance through enhanced light absorption, increased charge separation productivity, and greater accessibility of active sites [88]. The solvothermal method yields MOFs characterized by significant crystallinity and structural stability, which are vital for sustained photocatalytic performance across diverse reaction conditions [89]. For example, Li et al. [90] synthesized MIL-53Fe@MOF using a solvothermal method, resulting in enhanced photocatalytic efficiency compared to MIL-53Fe, attributed to enhanced electron-hole separation. The introduction of peroxymonosulfate under visible light significantly improved the degradation of oxytetracycline through the generation of sulfate radicals. Systematic investigations were performed on PMS dosage, contaminant level, temperature, and pH, confirming sulfate radicals and holes as the primary active species. Similarly, Su et al. [91] synthesized an amino-functionalized MOF (aU(Zr/In)) using a one-pot solvothermal approach to enhance the efficiency of visible light-driven CO_2RR. Amino functionalization decreased the bandgap and improved charge separation, whereas In doping generated oxygen vacancies, facilitating the LMCT process and reducing the energy barrier for CO_2-to-CO transformation. The optimized aU(Zr/In) attained a CO production rate of 37.58 μmol g^{-1} h^{-1}(Fig. 4k). The incorporation of doping does not alter the crystal structure or grain size of aU(Zr/In), as demonstrated by TEM images, which exhibit nano-polyhedrons similar to those of aU (Zr) (Fig. 4l). Lattice expansion resulting from In doping may be theoretically observable through HRTEM; however, the sensitivity of MOFs to electron beam damage complicates the detection of lattice fringes (Fig. 4m). Their study emphasizes the significance of ligand alteration and heteroatom doping in MOFs for solar energy transformation.

2.9.4. Sonochemical synthesis

Sonochemical synthesis is vital in customizing the morphology of MOFs for use in photocatalytic processes. This method employs ultrasonic waves to induce acoustic cavitation, resulting in localized elevated temperatures, pressures, and fast cooling rates [92]. Extreme conditions enhance nucleation and crystal development, leading to the emergence of MOFs with distinctive morphologies [93]. The sonochemical method allows for exact particle size, shape, and surface area regulation by adjusting ultrasonic power, duration, and solvent conditions [94]. The reduction in particle size and the increase in porosity obtained through this method improve light absorption, promote charge transfer, and offer numerous active sites, resulting in improved photocatalytic efficiency [95]. Sonochemical synthesis is a rapid, energy-efficient, and scalable method, rendering it particularly appropriate for the large-scale production of MOFs with customized morphologies for photocatalytic applications, including pollutant degradation and energy conversion [96]. For example, Tanhaei et al. [97] prepared a graphene oxide-MOF nanocomposite (GO-TMU-23) employing a facile, large-scale

sonochemical method at ambient temperature. The nanocomposite demonstrated markedly improved adsorption rates for methylene blue, achieving 90% removal and equilibrium in 2 min, surpassing the performance of the pristine materials. Similarly, Dastbaz et al. [98] designed a composite of GO and Cu-terephthalate (CuBDC-NH_2) MOFs to improve hydrogen adsorption and storage capabilities (Fig. 4n). The application of low-frequency ultrasound (20 kHz) resulted in enhanced reaction time, yield, and structure activation during synthesis. Fig. 4o, p illustrates the morphology of GO, Cu-BDC-NH_2, and Cu-BDC-NH_2@GO powders. Sonochemical synthesis yields consistent Cu-BDC-NH_2 crystals as a result of regulated energy distribution. In contrast, the addition of GO leads to imperfections and irregular shapes by functioning as a ligand via its functional groups and facilitating the formation of the supporting structure on the nanosheets. Surface method (Box-Behnken Design) further improves reaction conditions and GO content. The composite demonstrated enhanced hydrogen adsorption, which was attributed to a boosted BET surface area, a more significant number of active sites, and diminished gas diffusion resistance, while GO contributed to the chemical and thermal stability of the structure. More importantly, a detailed comparative table of different MOFs morphologies and their performance in various applications are summarized in Table. 1.

3. Morphologies of MOFs

3.1. Nanosheets

Nanosheets (NS) are 2D materials characterized by a high aspect ratio and ultrathin structures [177], providing a large surface area and distinctive electrical characteristics that significantly improve the photocatalytic efficiency of MOFs [178]. When integrated into MOFs, NS enhances charge separation and transport by offering brief diffusion paths for photoexcited electrons and holes, thus decreasing recombination rates [179]. Their extensive surface area assures enhanced light absorption and reveals more active areas for catalytic processes. Integrating nanosheets may enhance the structural stability of MOFs, especially under extended photocatalytic conditions [180]. These NS may work as conductive platforms or co-catalysts when modified with reactive groups or doped with heteroatoms, improving charge mobility and augmenting visible light absorption [181–183]. In this regard, Tian et al. [184] developed Ti_3C_2 NS by incorporating them into porous MOFs (UiO-66-NH_2) via a one-pot hydrothermal technique, establishing face-to-face interaction. The composite TU10 exhibited the greatest photocatalytic HER rates among the TU series, almost eight times larger than prsitine UiO-66-NH_2. The increased efficiency is due to the exposed active sites on the Ti_3C_2 NS, efficient charge separation and transfer via Schottky intersections, and better electron donation (Fig. 5a). The microstructure of the fabricated samples was examined by SEM and

Table 1
The comparative analysis of MOFs morphologies and their efficiency across various applications.

Morphologies	Surface Area (m^2/g)	Porosity	Stability	Charge Transfer	Key Applications	Performance Highlights	Refs.
Nanosheets	Very High (1000-4000)	Super-high	Moderate	Fast	Photocatalysis, Membrane Separation, Gas Adsorption	Extensive surface area, high light absorption capacity, rapid diffusion rates	[99–104]
Nanofilms	Moderate (500-1500)	Moderate	High	Fast	Coatings, Electronics, Sensing	Consistent coverage, superior adhesion, and effective electrical conductivity	[105–109]
Nanotubes	Moderate (600-2500)	Moderate	High	Fast	Supercapacitors, CO_2 Reduction, Catalysis	Elevated electron mobility, structural integrity, and enhanced mechanical stability	[110–114]
Nanorods	Moderate (400-1500)	Moderate	High	Moderate	Energy Storage, Sensors, Catalysis	Enhanced charge transfer and structural stability for electrochemical applications	[43,110,114–117]
Nanowires	Moderate (800-2000)	Moderate	High	Fast	Electronics, Batteries, Sensors	Significant aspect ratio enhances conductivity and facilitates effective electron transfer	[43,110,118,119]
Nanoparticles	High (500-3000)	High	Moderate	Fast	Catalysis, Drug Delivery, Gas Storage	Improved reaction kinetics and increased accessibility of active sites	[43,76,114,120,121]
Quantum Dots	High (500-3000)	High	Moderate	Very fast	Optoelectronics, Photocatalysis, Imaging	Robust quantum confinement, adjustable bandgap, elevated photoluminescence	[122–126]
Hollow	High (800-3000)	Super-high	Moderate	Moderate	Gas Adsorption, Drug Delivery, Photocatalysis	Elevated diffusion rates, improved molecular transfer, reduced density	[126–131]
Hierarchical	High (1000-4000)	High	Super-high	Fast	Multistep Catalysis, Energy Storage	Synergistic characteristics, improved stability, and multifunctionality	[43,132–135]
Sea Urchin-like	High (900-3500)	High	Moderate	Fast	Photocatalysis, Supercapacitors	Radial porosity enhances light absorption and increases the exposure of active sites	[136–140]
Monolith	High (1000-4000)	High	Super-high	Moderate	Adsorption, Separation, Catalysis	Excellent mechanical stability, macroporous structure, and simple handling	[141–145]
Nanocages	Very High (1200-5000)	Super-high	Moderate	Fast	Drug Delivery, Sensing, CO_2 Capture	Hollow surface, controlled release characteristics, and an elevated surface-to-volume ratio	[146–152]
Core-Shell	High (800-3000)	High	High	Optimized	Catalysis, Energy Storage, Drug Delivery	Enhanced stability, regulated interfacial characteristics, and tunable activity	[153–157]
Yolk-Shell	High (900-3500)	Super-high	Moderate	Moderate	Nanoreactors, Biomedicine, Catalysis	Internal void space facilitates reactant storage and provides protection against aggregation.	[158–161]
Aerogel	Extremely High (2000-6000)	High	High	Moderate	Environmental Remediation, Catalysis, Sensors	Extremely low weight, large surface area, and superior adsorption ability	[162–166]
Nanoflowers	High (1000-4000)	High	High	Fast	Photocatalysis, Energy Storage	Extensive active area, structured hierarchy, enhanced mass transfer	[167–170]
Nanoribbons	High (900-3500)	High	Moderate	Fast	Electronics, Flexible Devices	Significant flexibility, anisotropic conductivity, adjustable electronic characteristics	[171–176]

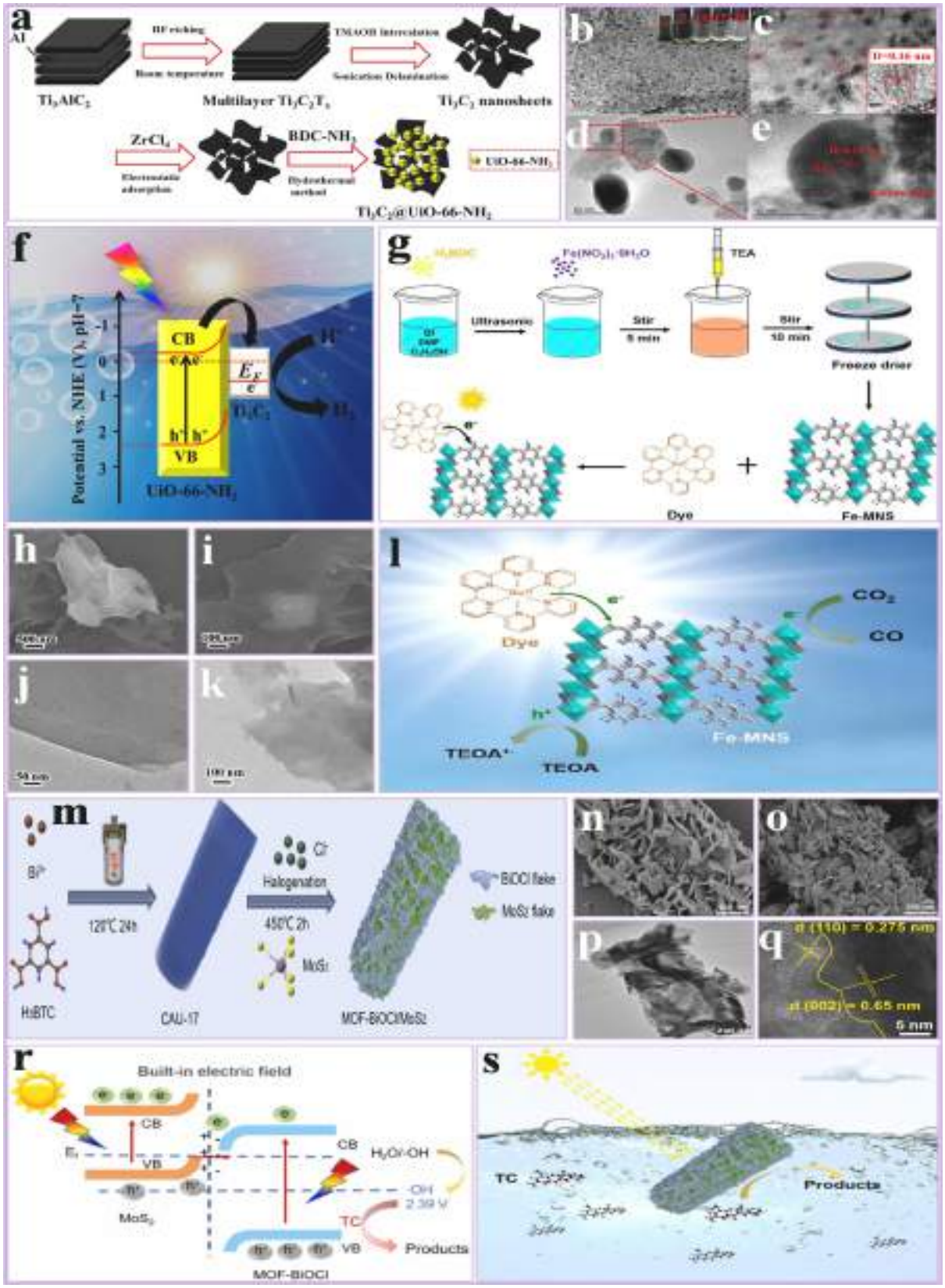

Fig. 5. (a) Synthesis process; (b) SEM; (c) TEM; (d, e) HRTEM analysis of Ti_3C_2 NS and TU series; (f) TU series energy level diagram for photocatalytic HER mechanism, reproduced with permission from ref [184] Copyright © 2019, Elsevier. (g) Synthesis process; (h, i) SEM; (j, k) TEM analysis of 2D Fe-MNS and dye-sensitized system; (l) The $Ru(bpy)_3^{2+}$ dye-sensitized 2D Fe-MNS system hypothesized process of VL-driven CO_2-to-CO reduction, reproduced with permission from ref [185] Copyright © 2022, Elsevier. (m) Synthesis process; (n, o) SEM; (p) TEM; (q) HRTEM analysis of MOF-BiOCl/MoS_2 composites; (r) Photocatalytic TC degradation mechanism during VL over MOF-BiOCl/MoS_2 samples; (s) Graphical representation of photocatalytic TC degradation, reproduced with permission from ref [186] Copyright © 2022, Elsevier.

TEM. Pure UiO-66-NH_2 particles exhibited an irregular cubic-spherical morphology, whereas $Ti_3C_2T_x$ MXenes revealed a 2D, multi-layered accordion-shaped structure, showing effective aluminum elimination during HF etching. SEM analysis indicated that the size of a peeled Ti_3C_2 NS was about 5.0 nm (Fig. 5b). TEM analysis verified the creation of homogeneous, ultrasmall Ti_3C_2 fragments devoid of aggregation (Fig. 5c). HRTEM analysis confirmed the Ti_3C_2 structure, exhibiting close proximity to UiO-66-NH_2 in TU10, with a discernible surface and lattice fringes of 0.18 nm, matching to the (11) crystalline plane of single-layer Ti_3C_2 (Fig. 5d, e). The photocatalytic HER efficiency was evaluated using a Na_2S-Na_2SO_3 system under simulated visible light. Pristine UiO-66-NH_2 showed low HER activity (25.6 $\mu mol \cdot h^{-1} \cdot g^{-1}$) due to fast electron-hole recombination. Adding Ti_3C_2 NS significantly enhanced HER rates, with TU10 achieving the highest efficiency at 204 $\mu mol \cdot h^{-1} \cdot g^{-1}$, about eight times higher than UiO-66-NH_2. This boost is due to Schottky barriers and accessible active sites on Ti_3C_2 NS, enhancing charge separation and transfer. TU10 outperformed Ti_3C_2/UiO-66-NH_2 made by penetration (61 $\mu mol \cdot h^{-1} \cdot g^{-1}$) and 2 wt%Pt/UiO-66-$NH_2$ (123 $\mu mol \cdot h^{-1} \cdot g^{-1}$), showing Ti_3C_2 as a potential Pt substitute. Stability tests revealed a 25% activity drop after 18 hours due to UiO-66-NH_2 degradation. The enhanced HER is attributed to efficient electron transfer from UiO-66-NH_2 to Ti_3C_2 via Schottky contacts and oxygen-terminated Ti_3C_2 facilitating proton reduction. The Na_2S-Na_2SO_3 system acts as a hole scavenger, reducing charge recombination and boosting HER efficiency (Fig. 5f). Their research indicates that MXenes/MOFs complexes use Schottky connections for effective photocatalytic hydrogen generation. Similarly, Idris et al. [185] synthesized 2D Fe-MOF NS (Fe-MNS) with a LUMO potential of 0.11 V vs RHE. Functionalization with the VL-responsive $[Ru(bpy)]_3^{2+}$ dye-sensitizer resulted in electron infusion into Fe-MNS, which changed its LUMO potential to -0.15 V vs. RHE, hence boosting photocatalytic CO_2-to-CO conversion to 1120 $\mu mol \cdot g^{-1} \cdot h^{-1}$ under visible. Doping Fe-MNS with Co enhanced the efficiency to 1637 $\mu mol \cdot g^{-1} \cdot h^{-1}$ (Fig. 5g). The structural features and phase homogeneity of the as-prepared 2D Fe-MNS sample were verified using SEM and TEM investigations. SEM analysis indicated that the sample comprises 2D sheet-like particles (Fig. 5h, i), whereas the TEM analysis demonstrated that the diffraction peaks corresponded with simulated peaks, affirming the phase purity of Fe-MOF crystals (Fig. 5j, k). The findings demonstrate that the 2D Fe-MNS NS were effectively synthesized, exhibiting a large surface area that offers increased catalytic active sites for photocatalytic processes. The photocatalytic CO_2RR capabilities of pristine 2D Fe-MNS and activated Dye/Fe-MNS samples were evaluated under visible light ($\lambda > 420$ nm) using TEOA as an electron donor. Pure 2D Fe-MNS exhibited no CO generation, presumably owing to its inadequate LUMO potential. Conversely, the synthetic $[Ru(bpy)]_3^{2+}$ dye alone had a CO generation efficiency of 105 $\mu mol \cdot g^{-1} \cdot h^{-1}$. The functionalization of 2D Fe-MNS with $[Ru(bpy)]_3^{2+}$ dye markedly enhanced CO output to 1120 $\mu mol \cdot g^{-1} \cdot h^{-1}$, illustrating the productivity of dye sensitization in visible light photocatalytic CO_2RR. The CO generation profile corresponded with the dye absorption spectrum, validating the dye as the primary light absorber in the system (Fig. 5l). Their work emphasizes dye-sensitized systems as viable approaches for developing visible light-responsive photocatalysts. Furthermore, Liu et al. [186] devised a MOF-BiOCl composite that consists of rod-shaped Bismuth-MOF (CAU-17) and BiOCl NS via an in-situ halogenation mechanism. Combining this with MoS_2 NS led to an S-scheme heterojunction that improved photocatalytic tetracycline (TC) breakdown. In 20 minutes, the improved MOF-BiOCl/MoS_2-3 composite accomplished 90% TC degradation (Fig. 5m). XRD analysis was performed on CAU-17, MoS_2, BiOCl, MOF-BiOCl, and their composites throughout the synthesis. The XRD pattern of CAU-17 matched prior data, validating its formation. 2H-MoS_2 peaks were seen in MoS_2. Pristine BiOCl, MOF-BiOCl, and their composites showed BiOCl-like diffraction peaks. Low MoS_2 concentration in composites prevented the observation of discrete peaks. CAU-17 peaks were seen in MOF-BiOCl and MOF-BiOCl/MoS_2 composites, with intensity reducing with increasing MoS_2 concentration, indicating expansion on the rod surface. SEM was used to study the structural features of MOF-BiOCl and MOF-BiOCl/MoS_2 catalysts. Both catalysts preserve CAU-17's rod-shaped structure with flaky microcrystals (Fig. 5n, o). MOF-BiOCl/MoS_2-3 rods have smaller MoS_2 flakes and exterior BiOCl flakes. BiOCl and MoS_2 NS on CAU-17 rods are evident in TEM (Fig. 5p) and HRTEM images (Fig. 5q), with 0.275 nm and 0.65 nm crystal planes, respectively. The photocatalytic efficiency of MOF-BiOCl/MoS_2 samples was investigated for TC degradation. The degradation rate of pristine BiOCl was 40%, whereas MOF-BiOCl reached 72% after 20 minutes. By adding 3% MoS_2, MOF-BiOCl/MoS_2-3 achieved the greatest performance at 90%. However, adding 7% MoS_2 decreased efficiency by causing excessive loading, hindering heterojunction production and electron-hole dissociation. Degradation exhibited quasi-first order kinetics, with MOF-BiOCl/MoS_2-3 having the greatest kinetic constant ($k = 0.104$), 1.86 times higher than pristine BiOCl. An unchanged XRD pattern showed that the catalyst was active and stable across five cycles. The degradation mechanism found $\bullet OH$ and h^+ as the main active chemicals, with $\bullet O_2^-$ playing a minor role. Applications are possible due to the stability and photocatalytic activity of photocatalyts (Fig. 5r, s). Their method for building heterostructure photocatalysts for wastewater treatment is ideal for energy storage applications.

3.2. Nanofilms

Nanofilms are fragile, 2D structure distinguished by their low thickness and large lateral dimensions, providing unique physicochemical features, including excellent surface-to-volume ratios and superior electrical conductivity [187]. In MOFs, nanofilms significantly enhance photocatalytic activity. Their thin structure promotes fast charge movement and decreases the diffusion length of photoexcited electrons and holes, considerably reducing recombination losses [108,188]. Furthermore, nanofilms accelerate light absorption by interacting with incoming photons across a wide range, enhancing light harvesting [189]. When incorporated into MOFs, nanofilms provide an extensive surface area for the adsorption of reactants and catalysis, facilitating effective contact with target molecules [190]. Additionally, nanofilms may function as structural templates or conductive layers, facilitating the formation of MOFs with enhanced stability and homogeneity. This synergy amplifies the catalytic effectiveness of MOFs, rendering them more proficient for applications such as WS, CO_2RR, and pollutant degradation [191,192]. For example, Gao et al. [193] fabricated an innovative, versatile platform that integrates semiconductor ZnInS NS with 2D conductive MOF (ZIF-8 nanofilms; NF), referred to as ZnInS NS@ZIF-8 NF, enabling concurrent fluorescence detection and photocatalysis. This platform, produced by a facile in-situ self-assembly process, demonstrates markedly enhanced photocatalytic performance and facilitates real-time, label-free, and sensitive fluorescence sensor. The ZnInS NS function as a photocatalyst and a self-sacrificial template, supplying Zn^{2+} ions for developing ZIF-8 nanofilms, therefore improving electron transfer and facilitating target preconcentration (Fig. 6a). The morphology and microstructure of the ZnInS NS@ZIF-8 NFs were analyzed using SEM. The ZnInS NS exhibited a hierarchical flower-shaped microsphere structure formed by self-assembled nanoflakes. Following the in-situ creation of ZIF-8 NF, the ZnInS NSs maintained their original flaky morphology. Still, it exhibited increased roughness and thickness, with the total thickness rising from 22 nm to 40–46 nm, suggesting that the ZIF-8 NFs contributed an additional 5–12 nm (Fig. 6b–e). The photocatalytic effectiveness of bare ZnInS NSs, ZIF-8, and ZnInS NS@ZIF-8 NF was assessed for the breakdown of TC under visible light. ZnInS NS@ZIF-8 NFs presented exceptional photocatalytic efficiency, degrading TC swiftly within 5 minutes, in contrast to ZnInS NSs and ZIF-8, which attained removal efficiencies of 43.3% and 36.3%, respectively. The ZnInS NS@ZIF-8 NFs exhibited a large surface area and many adsorption sites, improving interaction with TC. Despite four cycles, the photocatalytic activity remained adequate, affirming the capability of ZnInS NS@ZIF-8 NFs for effective water pollutant

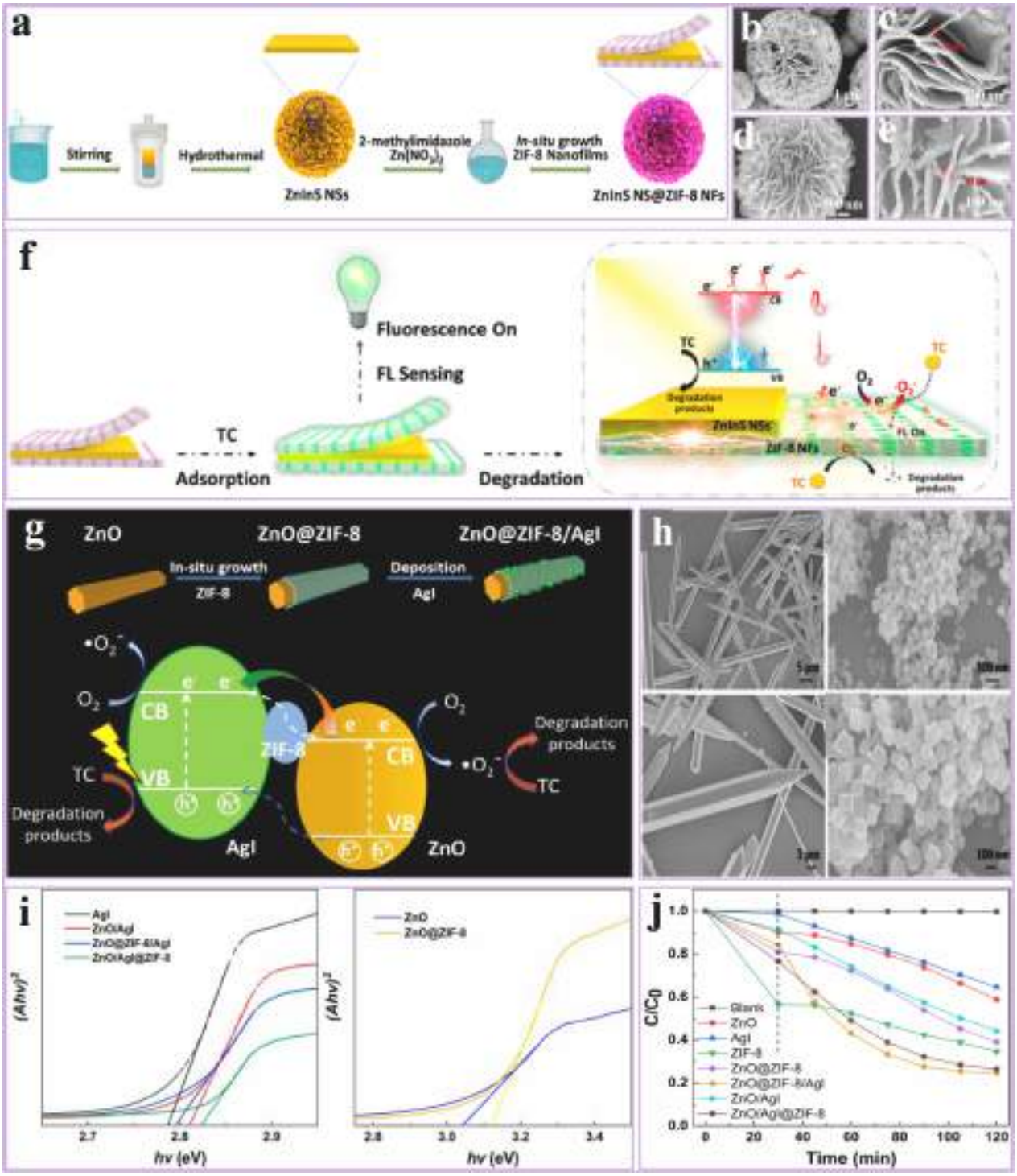

Fig. 6. (a) Synthesis route of the ZnInS NS@ZIF-8 NFs; SEM analysis of (b, c) ZnInS NSs; (d, e) ZnInS NS@ZIF-8 NFs; (f) The tactics of TC adsorption, detection, and degradation over ZnInS NS@ZIF-8 NFs, reproduced with permission from ref [193]Copyright © 2021, Elsevier. (g) Synthesis process the ZnO@ZIF-8/AgI and the photocatalytic degradation process for ZnO@ZIF-8/AgI to TC; (h) SEM analysis of ZnO, ZIF-8, and AgI; (i) Photographic photocatalyst bandgap energy $(Ahv)^2$ vs energy *(hv)* plots; (j) TC adsorption and photocatalytic degradation over as-synthesized materials under visible light, reproduced with permission from ref [194] Copyright © 2022, Elsevier.

degradation. Their research investigated the sensing and photocatalytic processes of ZnInS NS@ZIF-8 NFs. Fluorescence investigation demonstrated increased emission when TC reacted with Zn(II) and ZIF-8, attributed to the stable coordination bond creation and the distinctive pore structure of ZIF-8, which entrapped TC molecules and limited their rotation, augmenting fluorescence. Photocurrent responses indicated that ZnInS NS@ZIF-8 NFs exhibited excellent effectiveness in electron-hole pair separation, hence enhancing electron transport between ZnInS NSs and ZIF-8 (Fig. 6f). Their methodology provides exciting directions for the future formation of sophisticated photocatalysts. Similarly, Dai et al. [194] synthesized a ternary ZnO@ZIF-8/AgI material to enhance adsorption and photocatalytic performance. The ZnO microrods were developed using a hydrothermal technique, accompanied by the self-sacrificial synthesized ZIF-8, which accumulates targets next to

the photocatalyst and offers binding sites for AgI nanoparticles. AgI on ZnO@ZIF-8 facilitates the suppression of electron-hole recombination, improving photocatalytic performance. The composite effectiveness was evaluated for TC degradation under visible light, whereby electrons from AgI were transported via the ZIF-8 shell to ZnO, producing reactive oxygen species ($\bullet O_2^-$) for TC decomposition. The photocatalytic performance of ZnO@ZIF-8/AgI surpassed that of the control ZnO/AgI@ZIF-8 composite (Fig. 6g). SEM images demonstrate the morphologies of ZnO, ZIF-8, and AgI. ZnO micro rods are characterized as smooth hexagonal prisms, ZIF-8 manifests as well-organized rhombic dodecahedral nanocrystals, and AgI nanoparticles coalesce into uneven, rough formations. AgI nanoparticles adhere to the ZnO surfaces following in-situ deposition, forming ZnO/AgI heterojunctions. In the ZnO@ZIF-8 composite, ZnO maintains its microrod morphology, while the surface exhibits increased roughness owing to the homogeneous, thick ZIF-8 nanofilms, which augment TC adsorption. The in-situ fabrication of ZIF-8 using Zn^{2+} derived from ZnO guarantees a robust and tightly interconnected structure, enhancing the stability of the photocatalyst (Fig. 6h). Investigation of UV-visible light absorption indicates that incorporating AgI nanoparticles extends the visible light absorption spectrum of ZnO microrods. However, the addition of ZIF-8 nanofilms does not substantially impede light absorption. The absorption boundaries of ternary ZnO@ZIF-8/AgI and ZnO/AgI@ZIF-8 materials exhibit a red shift relative to ZnO, indicating enhanced photoresponse during visible light. The bandgap energies (Eg) determined by the *Tauc* calculation indicate that the incorporation of AgI significantly decreases Eg, with ZnO@ZIF-8/AgI exhibiting the lowest Eg of 2.79 eV, hence augmenting its photocatalytic efficiency (Fig. 6i). The photocatalytic efficiency of ZnO@ZIF-8/AgI was assessed employing TC under visible light, demonstrating a substantial enhancement in adsorption and degradation relative to other catalysts. ZnO@ZIF-8/AgI had the maximum degradation rate of 75.47% after 90 min, surpassing ZnO, AgI, ZIF-8, ZnO/AgI, and ZnO/AgI@ZIF-8, attributable to its superior surface area and effective electron-hole separation. The findings conformed to a pseudo-first-order reaction model, with ZnO@ZIF-8/AgI exhibiting the greatest rate constant, five times superior to pristine ZnO. The ZIF-8 shell enhances performance by concentrating TC, supporting AgI nanoparticles, and promoting visible light absorption while reducing electrons-holes recombination. In comparison, ZnO/AgI@ZIF-8 exhibited diminished stability owing to fewer interactions among its components, hence underscoring the benefits of ZnO@ZIF-8/AgI (Fig. 6j). Their research introduced the innovative ZnO@ZIF-8/AgI for tetracycline (TC) photodegradation and offered new perspectives for the synthesis and use of additional MOF-derived heterostructure photocatalysts.

3.3. Nanotubes

Nanotubes (NT) are hollow cylindrical nanostructures characterized by high aspect ratios, distinctive electronic characteristics, and superior stability [195]. Their hollow symmetry and high surface area render them suitable for incorporation into MOFs to improve photocatalytic efficiency [196]. In MOFs, NT enhances charge separation and transfer by offering a continuous conductive route for photoexcited charge carriers, thus reducing recombination losses [197,198]. The tubular structure enhances reactant diffusion and adsorption by increasing surface area and porosity, which are essential for catalytic reactions. Furthermore, NT serves as a light-scattering centers, thereby prolonging light-matter interaction and enhancing the absorption of incoming photons [199–201]. Incorporating NT into MOFs improves the stability of the photocatalyst by offering structural reinforcement and facilitating the development of hierarchical structures. This synergy enhances the photocatalytic performance of MOFs [202–204]. Therefore, Liang et al. [205] prepared a hierarchical S-scheme TiO_2@CoNi-MOF NT heterojunction photocatalyst for CO_2RR. The design comprises ultrathin, high-porosity CoNi-MOF NS synthesized atop TiO_2 NT by a solvothermal technique. This heterojunction facilitates charge transfer and separation, offers several active sites, and promotes CO_2 adsorption, light absorption, and CH_4 preference. The improved TiO_2@CoNi-MOF NT exhibited enhanced CO_2RR efficiency relative to the separate TiO_2 and CoNi-MOF constituents, with a CH_4 yielding of 41.65 μmol g^{-1} h^{-1} with 93.2% selectivity and commendable stability. The hierarchical TiO_2@-CoNi-MOF NTs have been synthesized by a multi-step methodology that included the electrospinning and carbonization of polyacrylonitrile fibers to generate carbon nanofibers (CNFs). TiO_2 was then applied to CNFs to create a CNF@TiO_2 core-shaped configuration by alcoholics, accompanied by higher-temperature calcination, which converted CNFs into gaseous byproducts, resulting in higher-crystallinity anatase TiO_2 NT (Fig. 7a). The morphology and microstructure of the produced materials were examined using SEM and TEM. CNFs were originally synthesized with a diameter of around 200 nm and a polished surface (Fig. 7b, e). Following the application of TiO_2, the surfaces of the CNF@TiO_2 fibers exhibited increasing roughness, and their diameter expanded to 350–400 nm (Fig. 7c, f), and HRTEM verified the presence of anatase TiO_2 (Fig. 7d, g). Post-calcination, TiO_2 NT with a marginally decreased 200–250 nm diameter was produced, preserving anatase properties. The improved CO_2 photoreduction performance of TiO_2@-CoNi-MOF NTs is ascribed to many significant aspects. The hierarchical S-scheme heterojunction design boosts light absorption via numerous reflections and augments CO_2 adsorption and reduction. This configuration integrates 1D TiO_2 NT with 2D CoNi-MOF NS, enhancing mass and charge transfer efficiency. Tests demonstrate that TiO_2@CoNi-MOF NTs show enhanced CO_2 adsorption relative to pristine TiO_2 or CoNi-MOF. The S-scheme mechanism, shown by variations in work functions, flat-band potentials, and band topologies, enables effective charge transfer. Electrons produced in the valence bands (VB) of TiO_2 and CoNi-MOF migrate to their related conduction bands (CB), facilitating less recombination and improved photoreduction. This process and the hierarchical structure and bimetal active centers significantly enhance CO_2RR performance, resulting in increased CH_4 selectivity and output (Fig. 7h). Their research indicates a possible avenue for developing hollow semiconductive-MOF hybridized photocatalysts to enhance solar-induced energy transformation efficiency. Similarly, Pi et al. [206] prepared an innovative photocatalyst by combining multiwalled carbon NT (MWCNT) with NH_2-MIL-68(In) to improve the photocatalytic reduction of Cr(VI), a hazardous heavy metal ion. The MWCNT/NH_2-MIL-68(In) (PL-1) complex exhibits a willow leaf-shaped MOF developed on a MWCNT backbone, promoting effective transfer of photoexcited carriers. MWCNTs further facilitated the formation of additional mesopores for Cr(VI) diffusion and enhanced visible light absorption without modifying the CB location. This alteration enhanced the photocatalytic kinetic constant PL-1 to virtually thrice that of the pristine MOF (Fig. 7i). The structure of the MWCNT/NH_2-MIL-68(In) composite was analyzed using SEM and TEM imaging techniques. Acid-treated MWCNTs had a tubular morphology with a diameter of around 20 nm. The SEM analysis revealed that the NH_2-MIL-68(In) crystals, like willow leaves, formed highly dispersed nanostructures around the MWCNTs, partly avoiding their visibility (Fig. 7j). TEM analysis further validated this encapsulation, demonstrating that the In-MOF developed along tubular structure of the MWCNTs, preserving the willow leaf-like shape while enveloping the CNT (Fig. 7k). Integrating MWCNTs into NH_2-MIL-68(In) markedly enhanced the transfer of photogenrated charge carriers and decreased the recombination of electron-hole pairs, which is essential for improving surface redox processes. Steady-state photoluminescence (PL) demonstrated that PL-1 (MWCNT/NH_2-MIL-68(In)) had decreased emissions relative to the core NH_2-MIL-68(In), indicating efficient charge transfer to MWCNTs. This was also corroborated by increased photocurrents in PL-1, validating improved charge separation. Upon light irradiation, NH_2-MIL-68(In) produced electrons that were transported to MWCNTs, enhancing the diffusivity of Cr(VI) to the photocatalyst surface and resulting in increased photoreduction performance (Fig. 7l). Their research presents a viable method for

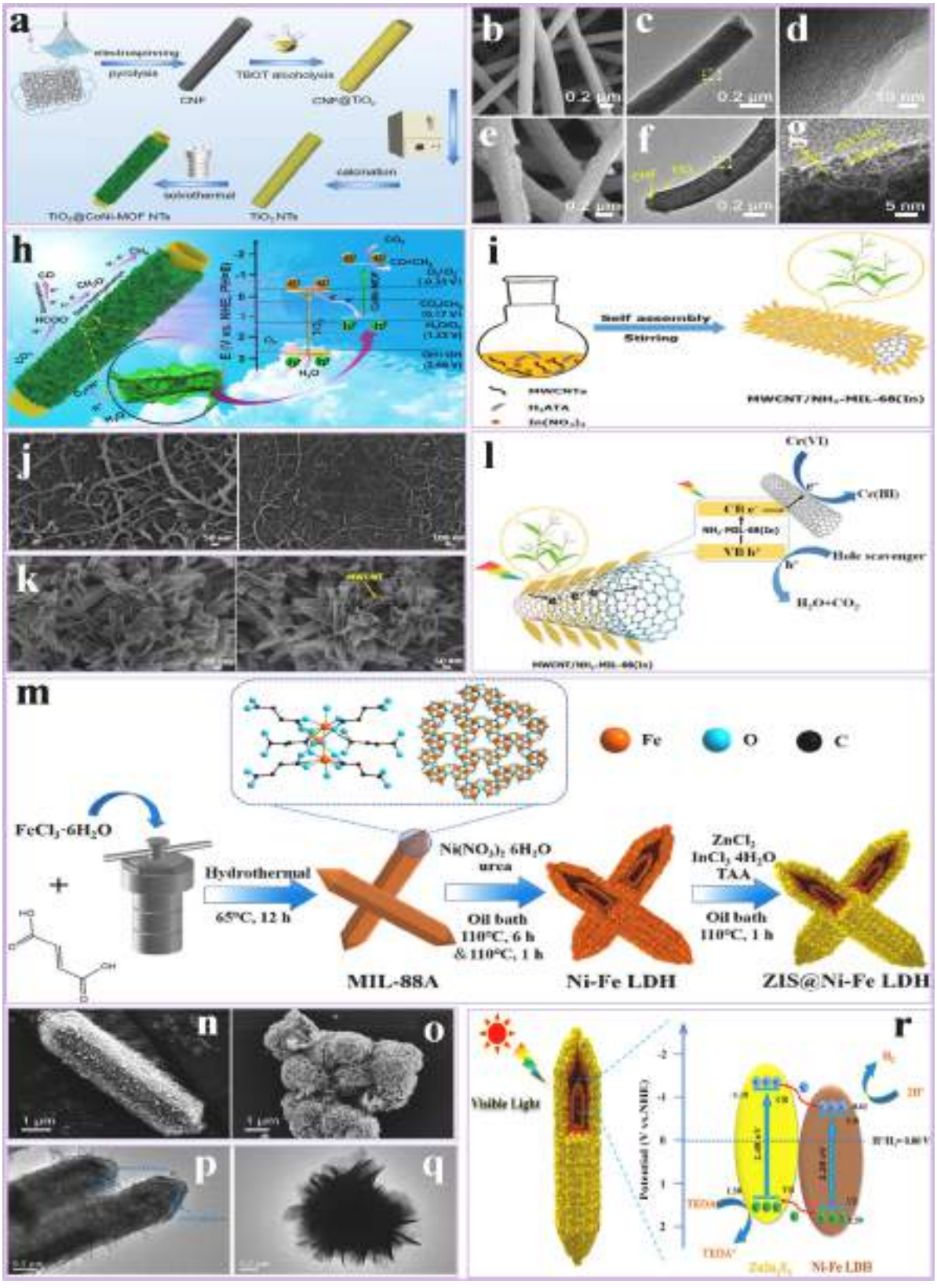

Fig. 7. (a) Synthesis process of TiO_2@CoNi-MOF NT; SEM analysis of (b) CNFs; (e) CNF@TiO_2 nanofibers; TEM analysis of (c) CNFs; (f) CNF@TiO_2 nanofibers; HRTEM analysis of (d) CNFs; (g) CNF@TiO_2 nanofibers; (h) photocatalytic CO_2RR mechanism over TiO_2@CoNi-MOF NT, reproduced with permission from ref [205] Copyright © 2023, Elsevier. (i) Synthesis process; (j) SEM; (k) TEM analysis of MWCNT/NH_2-MIL-68(In); (l) Schematic showing Cr(VI) reduction on PL-1 under visible light, reproduced with permission from ref [206] Copyright © 2017, Springer Nature. (m) Synthesis process; SEM analysis of (n) Ni−Fe LDH; (o) $ZnIn_2S_4$; TEM analysis of (p) Ni−Fe LDH; (q) $ZnIn_2S_4$; (r) Charge transfer diagram for ZIS@Ni-Fe LDH composite under visible light, reproduced with permission from ref [207] Copyright © 2021, American Chemical Society.

environmental cleanup with solar energy. It is the first demonstration of MWCNT/MOF materials for photocatalytic applications. Furthermore, Zhao et al. [207] produced $ZnIn_2S_4$ (ZIS) NS on MIL-88A-based Ni−Fe layered double hydroxide (LDH) to generate ternary-shelled NT (ZIS@Ni−Fe LDH) by a self-assembly approach (Fig. 7m). The structural features of Ni−Fe LDH, $ZnIn_2S_4$, and ZIS@Ni−Fe LDH composites were analyzed using SEM and TEM techniques. Ni−Fe LDH has a hexagonal rod-shaped morphology encased in a rough nanosheet shell, whereas pristine $ZnIn_2S_4$ manifests as flower-like microspheres (Fig. 7n, o). The ZIS@Ni−Fe LDH composite has $ZnIn_2S_4$ NS that uniformly envelops the Ni−Fe LDH, resulting in a ternary-shelled morphology. Excess $ZnIn_2S_4$ results in aggregation. It also verifies the uniform distribution of Ni, Fe, O, Zn, In, and S, emphasizing the close interaction between $ZnIn_2S_4$ and Ni−Fe LDH, facilitating charge transfer. The ternary-shelled structure of the heterostructure enhances hydrogen diffusion and the transmission of photoexcited electrons (Fig. 7p, q). The photocatalytic HER of Ni−Fe LDH, $ZnIn_2S_4$, and ZIS@Ni−Fe LDH was evaluated under visible light using TEOA as a hole scavenger. Pristine $ZnIn_2S_4$ had a HER rate of 301.86 μmol g^{-1} h^{-1}, while Ni−Fe LDH showed inactivity. The ZIS@Ni−Fe LDH composites demonstrated markedly improved H_2 generation, with the ZIS@Ni−Fe LDH-8 sample attaining a peak rate of 2035.81 μmol g^{-1} h^{-1}, about 6.7 times more than that of pristine $ZnIn_2S_4$. This improvement is due to the excellent heterostructure development between $ZnIn_2S_4$ and Ni−Fe LDH, which promotes effective electron-

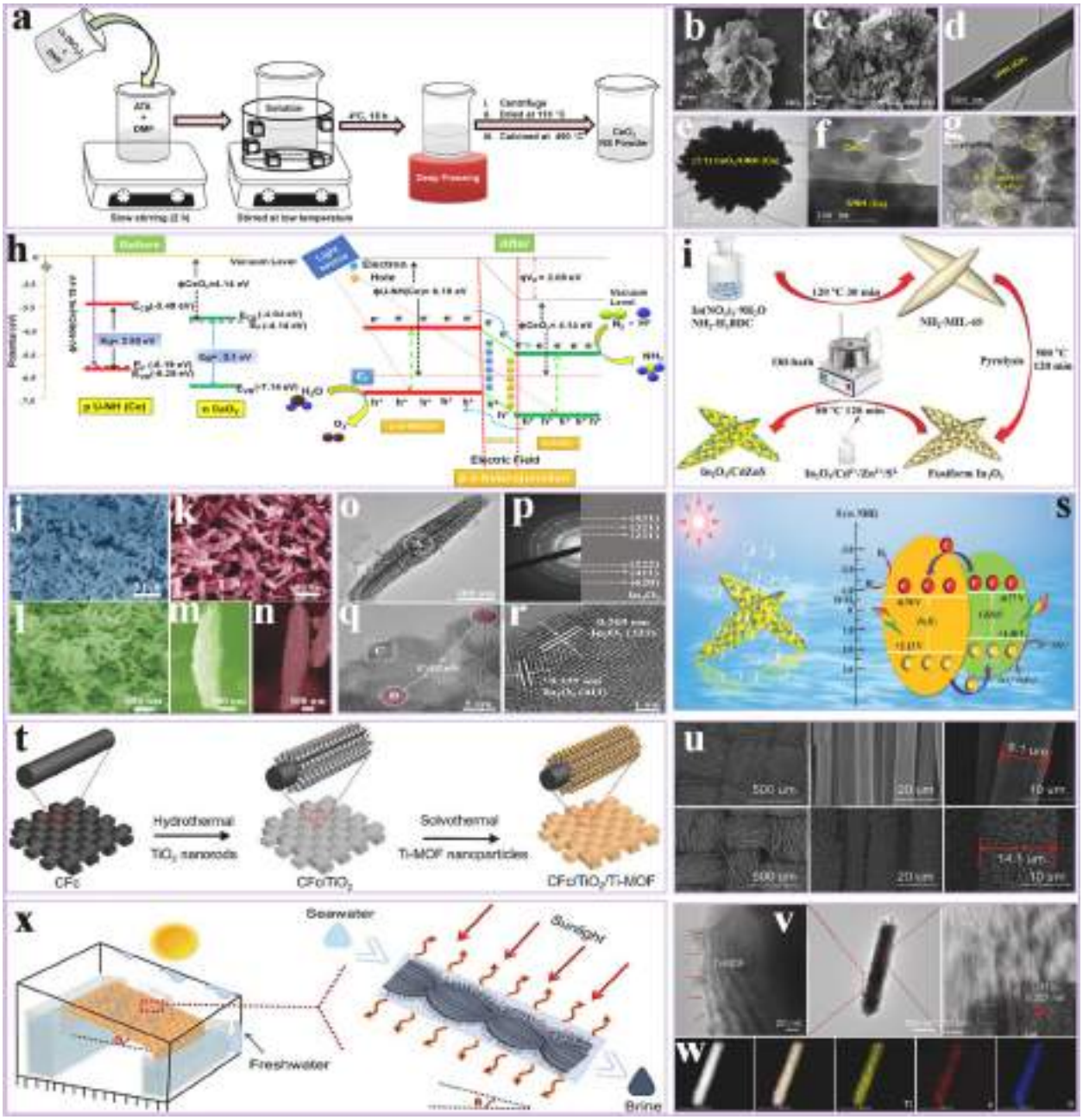

Fig. 8. (a) Synthesis process; (b, c) FESEM; (d–f) TEM; (g) HRTEM analysis of CeO_2 NS and CeO_2/UNH (Ce) Composite; (h) Schematic Representation of NH_3 evolution and OER on CeO_2/UNH (Ce) p-n Heterojunction (Rod@Sheet), reproduced with permission from ref [217] Copyright © 2021, American Chemical Society. (i) Synthesis process of In_2O_3/CdZnS composite photocatalysts; FESEM analysis of (j) NH_2-MIL-68, (l, m) MOFs-derived In_2O_3, (k, n) In_2O_3/CdZnS hybrids; (o, p) TEM; (q, r) HRTEM analysis of In_2O_3/CdZnS; (s) The suggested photocatalytic reaction process for the In_2O_3/CdZnS hybrid photocatalyst, reproduced with permission from ref [218] Copyright © 2021, John Wiley and Sons. (t) Synthesis process; (u) SEM; (v) TEM; (w) Elemental mapping of CFc/TiO_2/Ti-MOF; (x) Schematic illustration of the CFc/TiO_2/Ti-MOF evaporator, reproduced with permission from ref [219] Copyright © 2024, Elsevier.

hole dispersion. Conversely, inadequate and excessive $ZnIn_2S_4$ loading in ZIS@Ni−Fe LDH-1 and ZIS@Ni−Fe LDH-11, respectively, led to reduced H_2 generation owing to insufficient $ZnIn_2S_4$ availability or agglomeration (Fig. 7r). Consequently, the ZIS@Ni−Fe LDH ternary-shelled NT, which exhibits a substantially improved photocatalytic WS efficiency, is an exciting alternative to satisfy energy and environmental demands.

3.4. Nanorods

Nanorods are elongated nanostructures characterized by an elevated aspect ratio, displaying distinct optical, electronic, and structural characteristics [208]. Nanorods in MOFs considerably improve photocatalytic activity by permitting efficient charge transfer and separation [209]. The anisotropic shape facilitates the motion of photoexcited electrons and holes, thus decreasing recombination and enhancing catalytic efficiency [210,211]. The elongated morphology enhances surface area and active site accessibility, facilitating improved adsorption of reactants and increased light absorption. Additionally, nanorods function as scaffolds for the formation of hierarchical structures within MOFs, enhancing light scattering and prolonging light-matter interaction [212–214]. These improved productivity and stability properties are notably advantageous for photocatalytic applications [215]. By incorporating nanorods into MOFs, scientists may enhance their photocatalytic capabilities for environmentally friendly and sustainable energy solutions [216]. In this regard, Mansingh et al. [217] examined a 1D-2D p-n heterostructure consisting of rod-like Ce-MOF-NH_2 (UNH (Ce)) and sheet-shaped, OV-enrich CeO_2, which was produced by a simplistic hydrothermal method. The binary compound was synthesized using various MOF-to-CeO_2 ratios of 1:1, 1:2, and 2:1. They assessed the photocatalytic effectiveness of these composites for nitrogen reduction reaction (N_2RR) and oxygen evolution reactions (OER), illustrating the promise of this heterostructured material in photocatalysis (Fig. 8a). Fig. 8b, c depicts the surface morphologies of the photocatalysts CeO_2, UNH (Ce), and their (1:1) mixture, analyzed using field emission scanning electron microscopy (FESEM). CeO_2 has a sheet-like shape characterized by ripples and twisted edges. UNH (Ce) exhibits rod-shaped structures of diverse lengths and diameters, with certain aggregation attributed to irregular nucleation (Fig. 8b). The (1:1) CeO_2/UNH (Ce) material exhibits a blend of sheet and rod morphologies, indicating effective decorating of the rod-shaped UNH (Ce) on the CeO_2 NS. This hybrid structure develops during the in-situ development of UNH (Ce) rods on CeO_2, showing efficient coordination between the two materials (Fig. 8c). The TEM analysis of the synthesized photocatalyst provided comprehensive insights into its shape, elemental dispersion, crystalline structure, and surface interaction. The rod-shaped UNH (Ce) and sheet-like CeO_2 nanostructures were clearly seen, confirming their morphology in accordance with other studies. In the (1:1) CeO_2/UNH (Ce) material, luminous circular rings signified distinct crystal planes (Fig. 8d–f), and HRTEM analysis revealed lattice fringes matching to the (111) crystal plane of CeO_2 cubic fluorite phase. Lattice distortion, amorphization, and defects in the composite structure improve catalytic efficiency by facilitating charge carrier separation, enhancing light absorption, and boosting N_2 polarization for efficient photocatalysis. The distinct interfacial connection between CeO_2 and UNH (Ce) verifies the creation of the composite, characterized by CeO_2 sheets composed of many aggregated particles (Fig. 8g). The photocatalytic N_2RR capability of several samples was evaluated during ultraviolet light in a quartz batch photoreactor. Their research indicated that N_2 fixation transpired only in the context of both light and a catalyst, with no alternate routes for NH_3 production identified. Among the evaluated catalysts, the (1:1) CeO_2/UNH (Ce) material had the greatest NH_3 generation rate of 0.856 mg/L/h (47.55 μmol/L/h) under UV light, owing to efficient charge carrier separation and oxygen vacancies that enhance N_2 activation and exciton separation. The NH_3 generation rate rose to 1.57 mg/L/h using a 10 vol% methanol mixture saturated with N_2, suggesting that methanol augments the photocatalytic activity by producing carbon dioxide radical anions ($\bullet CO_2^-$) having significant reduction capability. No NH_3 was seen without N_2 or in Ar-saturated deionized water, showing that NH_3 synthesis is exclusively attributed to the photoreduction of N_2 with aqueous protons (Fig. 8h). Their research proposes a novel method to enhance NH_3 synthesis and OER under ambient conditions. Similarly, Yang et al. [218] synthesized higher-efficiency visible light-driven In_2O_3/CdZnS hybridized photocatalysts with a facile oil-bath technique. This included the connection of ultrafine CdZnS nanoparticles onto NH_2-MIL-68-based In_2O_3 mesoporous nanorods. The resultant hybrid photocatalysts exhibited superior visible light absorption, increased charge transfer and separation, and an excess of active sites (Fig. 8i). FESEM analysis of NH_2-MIL-68, In_2O_3, and In_2O_3/CdZnS composites revealed that NH_2-MIL-68 exhibited fusiform rod-shaped nanostructures characterized by a smooth surface. Post-annealing, In_2O_3 nanorods maintained their morphology while exhibiting increased roughness and porosity. The In_2O_3/CdZnS composites maintained this structure, incorporating CdZnS nanoparticles to enhance surface roughness. N_2 adsorption-desorption analyses revealed the presence of mesopores in both In_2O_3 and In_2O_3/CdZnS, resulting in the hybrid sample exhibiting a superior BET surface area of 64.71 m^2/g, in contrast to In_2O_3 29.08 m^2/g, and hierarchical mesopores at around 8 and 15 nm attributed to the incorporation of CdZnS (Fig. 8j–n). Furthermore, the morphological and structural properties of In_2O_3 and In_2O_3/CdZnS (FICZ-2.5) composites were examined using TEM and HRTEM. TEM analysis demonstrates that both samples have a fusiform nanorod morphology (Fig. 8o, p). HRTEM analysis reveals interlayer spacings in In_2O_3 associated with the (222) and (211) planes, but the In_2O_3/CdZnS hybrid exhibits supplementary lattice fringes for CdZnS, with lattice spacings linked to certain planes of both In_2O_3 and CdZnS (Fig. 8q, r). In addition, the photocatalytic HER efficiencies of In_2O_3 and In_2O_3/CdZnS materials were assessed under visible light irradiation, using Na_2S and Na_2SO_3 as hole scavengers. The In_2O_3/CdZnS (FICZ-2.5) composite exhibited a much superior H_2 generation rate (1110 μmol g^{-1} h^{-1}) relative to pristine In_2O_3, reflecting an increase of 185-fold. The composite exhibited consistent efficiency throughout three cycles and demonstrated an apparent quantum yielding (AQY) of 0.32% at 420 nm, similar to previous In_2O_3-derived photocatalysts with Pt cocatalysts. The photocatalytic effectiveness of In_2O_3/CdZnS exceeded that of other comparable photocatalysts. In_2O_{3s}/CdZnS also exhibited superior photocurrent responsiveness and reduced electrochemical impedance relative to pristine In_2O_3, signifying enhanced charge carrier separation and transfer effectiveness (Fig. 8s). Furthermore, Meng et al. [219] describe the fabrication of a TiO_2/NH_2-MIL-125(Ti) nanorod array on carbon fiber cloth (CFc), referred to as CFc/TiO_2/Ti-MOF, via a hydrothermal-solvothermal method. This composite exhibits superior photoabsorption (89.5%) and exceptional hydrophilicity (contact angle of 0° in 5 seconds), surpassing the uncoated CFc substrate. The CFc/TiO_2/Ti-MOF efficiently eliminates pollutants such as Rhodamine B (76.4%), methylene blue (94.1%), tetracycline (62.8%), and ofloxacin (58.5%) during 120 minutes of sunlight exposure. Moreover, it attains a substantial evaporation rate of 1.86 kg $m^{-2}h^{-1}$ without salt precipitation, making it optimal for prolonged auto-cleaning solar desalination. The CFc/TiO_2/Ti-MOF composite was synthesized in two phases: first, TiO_2 nanorods were hydrothermally cultivated on CFc, followed by the solvothermal deposition of Ti-MOF. At first, the CFc is black and composed of smooth carbon fibers around 9.1 μm in diameter. Following the formation of TiO_2, the CFc transitions to a grey-white hue, with fiber diameters growing to around 14.1 μm and covered with TiO_2 nanorods of around 0.49 μm. After Ti-MOF deposition, the fibers exhibit a light-yellow hue, accompanied by an extra coating of about 3.81 μm and an enlarged fiber diameter of around 14.7 μm (Fig. 8t). SEM analysis verifies the effective deposition of Ti-MOF nanoparticles onto the TiO_2 nanorods. The CFc/TiO_2/Ti-MOF exhibits excellent resistance to abrasion and tensile stress and has hierarchical pores that improve light dispersion and facilitate water vapor release during evaporation

(Fig. 8u). In addition, the structure and content of TiO_2/Ti-MOF powder, extracted from the CFc/TiO_2/Ti-MOF, were examined using TEM. The powder comprises nanorods of 0.44 μm in width and 2.25 μm in length, with many connected nanoparticles. TEM analysis also reveals a separation of about 0.307 nm, which corresponds to the (110) crystal planes of rutile TiO_2 (Fig. 8v). Energy-dispersive spectroscopy (EDS) verifies the existence of Ti, O, and C elements, signifying that the nanorods consist of TiO_2 and Ti-MOF, with an atomic ratio of Ti/C/O of 43.49:3.36:53.15 (Fig. 8w). The findings validate the effective development of TiO_2/Ti-MOF nanorods on CF fabric. Moreover, salt crystallization is a prevalent problem for solar-driven evaporators due to diverse salt ions in saltwater. Crystalline salt may accumulate on the surfaces of photothermal materials, reflecting solar radiation and diminishing evaporation effectiveness. Two evaporation models were evaluated: a floating evaporator and a hanging evaporator, both employing CFc/TiO_2/Ti-MOF fabric. In the floating evaporator model, salt crystals started formation after 8 hours, resulting in a substantial reduction in the evaporation rate from 1.23 to 0.85 kg/m^2h owing to salt accumulation. Conversely, the hanging evaporator sustained an evaporation rate of around 1.84 kg/m^2h over 8 hours, exhibiting no discernible salt deposits, as the brine was perpetually extracted from the fabric. The hanging evaporator exhibited superior self-cleaning efficacy when

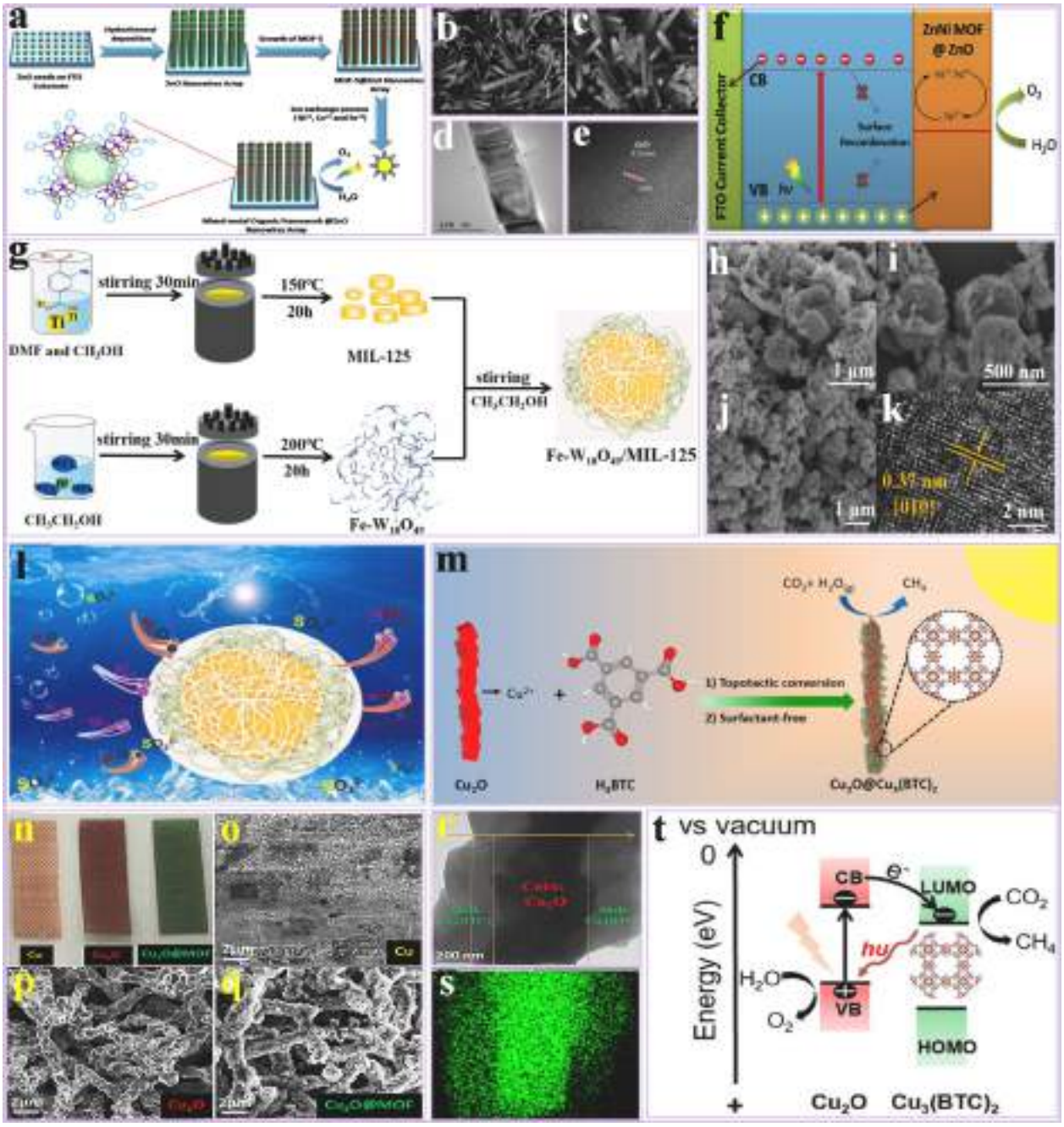

Fig. 9. (a) Synthesis process; (b, c) SEM; (d) TEM; (e) HRTEM analysis of ZnNi MOF @ZnO nanowires array; (f) Diagram illustrating PEC WS kinetics using ZnNi MOF@ZnO nanowire array as photoanode, reproduced with permission from ref [227] Copyright © 2019, Elsevier. (g) Synthesis process; (h–j) SEM; (k) TEM analysis of Fe-$W_{18}O_{49}$/NH_2-MIL-125 NW; (l) The proposed photocatalytic mechanism of Fe-$W_{18}O_{49}$/NH_2-MIL-125–2 for N_2 fixation under VL, reproduced with permission from ref [228] Copyright © 2024, Elsevier. (m) Synthesis process; (n–q) SEM; (r) TEM; (s) EDX mapping of $Cu_2O@Cu_3(BTC)_2$ core–shell NW; (t) The proposed photocatalytic mechanism of $Cu_2O@Cu_3(BTC)_2$ core–shell NW, reproduced with permission from ref [229] Copyright © 2021, John Wiley and Sons.

used with saline polluted by RhB, attributable to its exceptional wettability and photocatalytic characteristics. This demonstrates that the suspended evaporator design efficiently inhibits salt buildup and maintains optimal performance (Fig. 8x). Their research offers insights into the synthesis of innovative photothermal/photocatalytic membranes for effective self-cleaning solar desalination.

3.5. Nanowires

Nanowires (NW) are elongated nanostructures exhibiting higher aspect ratios, typically defined by their 1D morphology [220]. Nanowires play an important role in improving photocatalytic efficiency in MOFs. Their distinct structure enhances charge carrier transfer by reducing electron and hole recombination, which is essential in photocatalysis [221]. NW enhances the surface area available for reactant adsorption and establishes a continuous conductive pathway, thus enhancing the electronic interaction within the MOFs structures [222,223]. Their elongated define increases light scattering, extends light-matter interaction, and improves light absorption productivity. These features make NW-based MOFs ideal for WS, CO_2RR, and pollutant degradation applications, which need fast charge separation, higher catalytic efficiency, and more excellent stability [224–226]. Utilizing the structural and electronic properties of NW, researchers can synthesize MOFs that exhibit enhanced photocatalytic performance. For example, Peng et al. [227] propose a technique to fabricate a 3D mixed-MOF-doped array of ZnO NW (ZnNi MOF@ZnO) to improve PEC efficiency. In this system, ZnO NW functions as photon absorbers and charge carriers, whereas the ZnNi MOFs offer active sites for the photoelectrochemical mechanism, reducing the energy barrier for water oxidation and decreasing electrons-holes recombination. The 3D structure facilitates robust surface interaction, allowing fast charge transfer during photocatalytic OER. The ZnNi MOF@ZnO array showed enhanced water oxidative capability, characterized by the lowest onset potential (0.31 V vs. RHE) and the highest photocurrent density (1.40 mA/cm^2), in comparison to Zn MOF@ZnO and bare ZnO NW (Fig. 9a). The morphology of the synthesized ZnNi MOF@ZnO nanowire array was observed employing SEM and TEM. The SEM analysis indicated that the ZnNi MOF@ZnO NW has been orientated vertically on the FTO substrate (Fig. 9b, c). TEM analysis demonstrated a thinner layering of ZnNi MOF covering the ZnO NW, maintaining the capacity of ZnO capacity to absorb visible light and promote the electrocatalytic reduction of water (Fig. 9d). The measured matrix fringe of 0.26 nm correlates to the 002 plane of ZnO, but no discernible fringe for MOF-5 was discovered, perhaps attributable to the fragile layer of the mixed-MOF (Fig. 9e). The elevated electrocatalytic efficiency of the ZnNi MOF@ZnO NW array may be attributed to many causes. ZnO absorbs photons with energy higher than its bandgap, producing electron-hole pairs during visible light. In the n-type ZnO photoanode, photoexcited electrons migrate from the CB to the substrate and the counter electrode to lower water and create hydrogen. Simultaneously, the holes in the VB of ZnO migrate to the ZnNi MOF, facilitating the oxidation of Ni^{2+} to elevated valence states (Ni^{3+}/Ni^{4+}), which then react with water to produce oxygen before reverting to Ni^{2+}. The $Ni^{2+}/Ni^{3+}/Ni^{4+}$ redox mechanism reduces the energy barrier for water oxidation and amplifies photocurrent. Furthermore, the surface modification of ZnNi MOF mitigates surface trapping sites, reduces electrons-holes recombination, and enhances quantum effectiveness. The 3D design of the ZnNi MOF@ZnO array guarantees robust surface interaction for swift charge transfer and offers active sites for effective water reduction at minimal overpotentials. This approach improves the efficiency of charge separation and transfer, hence enhancing PEC water oxidation performance (Fig. 9f). Their technique provides a structure for developing advanced photoanodes for solar energy conversion. Similarly, Hou et al. [228] synthesized Fe-$W_{18}O_{49}$ NW and NH_2-MIL-125 with a two-step solvothermal technique. The two catalysts were disseminated in ethanol, and Fe-$W_{18}O_{49}$/NH_2-MIL-125 was synthesized by combining the suspensions and dispersing the ethanol. Fe-$W_{18}O_{49}$ NW, characterized by oxygen vacancies, are affixed to the surface of NH_2-MIL-125, diminishing the NW aggregation. The carrier transport pathway in the Fe-$W_{18}O_{49}$/NH_2-MIL-125 composite was modified, and the formation of a type II heterojunction significantly decreased the electron-hole recombination percentage, enhancing efficiency (Fig. 9g). SEM analysis elucidated the structural properties of the as-prepared composites. Fe-$W_{18}O_{49}$ had an NW morphology, while NH_2-MIL-125 presented a plate-like morphology with diameters between 300 and 600 nm. In the composite catalyst, the Fe-$W_{18}O_{49}$ NW were distributed and encased around NH_2-MIL-125, mitigating NW aggregation. This composite design increased the accessibility of active sites in Fe-$W_{18}O_{49}$, facilitating nitrogen fixation via more oxygen voids (Fig. 9h–j). TEM analysis revealed lattice fringes of 0.37 nm for Fe-$W_{18}O_{49}$, matching the (010) crystal plane, but the lattice of NH_2-MIL-125 was indiscernible (Fig. 9k). Electron paramagnetic resonance (EPR) were utilized to classify the radicals $\bullet O_2^-$ and •OH in Fe-$W_{18}O_{49}$, NH_2-MIL-125, and Fe-$W_{18}O_{49}$/NH_2-MIL-125 to suggest a reaction process. NH_2-MIL-125 exhibited a signal for DMPO-$\bullet O_2^-$, suggesting that its CB may decrease O_2 to $\bullet O_2^-$, since its CB value (-0.63 V vs. NHE) is superior to the potential for $O_2/\bullet O_2^-$ (-0.33 V vs. NHE). Nonetheless, no such signal was seen in Fe-$W_{18}O_{49}$/NH_2-MIL-125, indicating that $\bullet O_2^-$ was not produced. Fe-$W_{18}O_{49}$ exhibited a pronounced DMPO-•OH signal, indicating that its VB (2.39 V vs. NHE) is higher than the $H_2O/\bullet OH$ potential (2.24 V vs. NHE), hence facilitating •OH formation; however, Fe-$W_{18}O_{49}$/NH_2-MIL-125 demonstrated no •OH production. No $\bullet O_2^-$ or •OH radicals were identified in Fe-$W_{18}O_{49}$/NH_2-MIL-125, presumably owing to the type II heterojunction between Fe-$W_{18}O_{49}$ and NH_2-MIL-125. This junction creates a bidirectional carrier transfer pathway, facilitating the transition of electrons from the CB of NH_2-MIL-125 to the VB of Fe-$W_{18}O_{49}$, while holes transition from the VB of Fe-$W_{18}O_{49}$ to the VB of NH_2-MIL-125. The oxygen voids in Fe-$W_{18}O_{49}$ serve as electron-capturing centers and nitrogen adsorption sites, promoting electron injection intothe π antibonding orbital of nitrogen and producing NH_3 via protonation (Fig. 9l). Their study positively influences other scholars investigating photocatalytic nitrogen fixation and the development of cost-effective catalysts. Furthermore, Wu et al. [229] synthesized $Cu_2O@Cu_3(BTC)_2$ core–shell NW on a porous carbon structure (CM), using Cu_2O NW/CM as the precursor. The gradual dissolving rate of Cu^{2+} from Cu_2O and the rapid nucleation kinetics of $Cu_3(BTC)_2$ led to the encapsulation of Cu_2O NW inside the $Cu_3(BTC)_2$ structure (Fig. 9m). SEM images illustrating the morphological transitions from a flat substrate to NW structures in the CM, Cu_2O/CM, and $Cu_2O@Cu_3(BTC)_2$/CM samples. Both Cu_2O and $Cu_2O@Cu_3(BTC)_2$ NW had an average length of more than 8 μm (Fig. 9n–q). TEM analysis indicated that the Cu_2O core had a diameter of around 400 nm, while the MOFs outer shell was approximately 300 nm thick (Fig. 9r). It further validated the $Cu_2O@Cu_3(BTC)_2$ core-shell configuration. The solid Cu_2O core possesses a greater copper concentration than the porous $Cu_3(BTC)_2$ shell. The distribution of oxygen and carbon components indicates a reduced density of these elements around the dense Cu_2O core, presumably derived from the $Cu_3(BTC)_2$ shell. Cu, O, and C dispersion reveals a greater concentration in the core and a diminished concentration in the shell, corroborating the core-shell structure (Fig. 9s). To comprehend the improved efficiency of Cu_2O encapsulated in $Cu_3(BTC)_2$, the photoluminescence (PL) spectrum of Cu_2O/CM and $Cu_2O@Cu_3(BTC)_2$/CM thin films were examined. The $Cu_2O@Cu_3(BTC)_2$ composite demonstrated reduced PL intensity at 500 nm and introduced a novel peak within the 600–700 nm range relative to bare Cu_2O, signifying modified charge transport. $Cu_3(BTC)_2$, with a LUMO energy level of -3.7 eV, enables electron transport from the CB of Cu_2O (at -3.2 eV) to its LUMO, hence quenching the luminescence of Cu_2O. It further indicated reduced charge transfer resistance (Rct) for $Cu_2O@Cu_3(BTC)_2$/CM, indicating accelerated charge transfer. Transient photocurrent studies indicated enhanced photoexcited electron dissociation and transfer in Cu_2O decorated with $Cu_3(BTC)_2$. The novel PL peak at 630 nm indicates electron transport from the LUMO of

$Cu_3(BTC)_2$ to the VB of Cu_2O, exhibiting a 0.5 eV energy disparity that aligns with the observed shift in PL peak wavelength (Fig. 9t). Their results will encourage future efforts to create exceptionally efficient organic-inorganic composite photocatalysts.

3.6. Nanoparticles

Nanoparticles (NP) are zero-dimensional (0D) nanostructures characterized by sizes generally between 1 and 100 nm, which provide an excellent surface-to-volume ratio and adjustable characteristics [230]. Incorporating NP into MOFs markedly improves the photocatalytic efficiency via multiple mechanisms [231]. Their diminutive dimensions facilitate uniform distribution within the MOFs structure, enhancing the accessibility of active sites for catalytic processes [232]. NP enhances light absorption and promotes charge separation by functioning as electron sinks or facilitating charge transfer between the MOFs and the reactants. NP, including metal oxides [233], plasmonic metals [234], and quantum dots [235], may improve photocatalytic activity by narrowing the bandgap, improving visible light absorption, and strengthening the MOFs structure based on their composition [236–238]. Optimizing MOF-based systems for better reaction, selectivity, and stability may be achieved by using the specific features of NP. In this regard, Meng et al. [239] fabricated composite photocatalysts by depositing Ag NP onto NH_2-MIL-125(Ti) surface with various lower-index facets via an in-situ photodeposition technique. Incorporating Ag NP markedly improved photocatalytic performance and methane (CH_4) selectivity in CO_2RR. The enhancement is attributed to the impact of the Ag NP on the surface plasmonic resonance (SPR), which maximizes light absorption. Furthermore, the distributed Ag NP enhance charge separation and transfer, minimizing electrons-holes recombination and increasing overall photocatalytic performance (Fig. 10a). The structural characteristics of the as-synthesized catalysts were analyzed using SEM and TEM. NH_2-MIL-125(Ti) featuring exposed (001), (110), and (111) facets were festooned with NP without significant accumulation owing to the lower concentration of Ag. The original design of NH_2-MIL-125(Ti) was preserved after Ag incorporation (Fig. 10b−d). TEM analysis revealed evenly distributed Ag NP (~4 nm) on the (111) facets, exhibiting no agglomeration (Fig. 10e). Nonetheless, accumulation ensued as the silver level rose to 3.6%, resulting in a particle size of about 20 nm. The suggested photocatalytic method for CO_2 conversion using Ag NP-doped NH_2-MIL-125(Ti) with visible lower-index facets comprises many essential phases. The adsorption of CO_2 on the extensive surface area of catalysts is important, and it is increased by the inclusion of Ag NP. Photoexcited electron-hole pairs are produced due to light irradiation, with electrons being excited to the lowest unoccupied molecular orbital (LUMO) and holes remaining in the highest occupied molecular orbital (HOMO). The Ag NP promotes charge separation by absorbing electrons, reducing recombination, and enhancing charge transfer. The surface titanium species, particularly on (111) facets, significantly facilitate CO_2RR. The synergistic interaction between Ag NPs and exposed facets enhances photocatalytic performance (Fig. 10f). Their research offers guidance for exploring facet engineering in MOFs materials, specifically aimed to improve CH_4 selectivity to optimize photocatalytic efficiency. Likewise, Zhu et al. [240] synthesized a new Cu-MOF/$Cd_{0.5}Zn_{0.5}S$ composite catalyst by an electrostatic self-assembly process. Characterization investigations indicated that the robust interface between Cu-MOF and $Cd_{0.5}Zn_{0.5}S$ augmented active sites and improved HER efficiency. The synthesis of the Cu-MOF/$Cd_{0.5}Zn_{0.5}S$ heterojunction effectively reduced the photocatalytic limitations of $Cd_{0.5}Zn_{0.5}S$ and enhanced charge separation efficiencies. The composite exhibited great efficiency in photocatalytic HER and remarkable stability (Fig. 10g). SEM and TEM investigations of the Cu-MOF/$Cd_{0.5}Zn_{0.5}S$ (CZSM-15) composite demonstrated significant structural attributes. $Cd_{0.5}Zn_{0.5}S$ manifested as irregular spherical NP, while Cu-MOF had a normal octahedral structure (Fig. 10h, i). In the CZSM-15 composite, the surface exhibited increased roughness while maintaining the octahedral morphology of the Cu-MOF (Fig. 10j). HRTEM analysis revealed that $Cd_{0.5}Zn_{0.5}S$ NP thickly coated the Cu-MOF surface, exhibiting a lattice spacing of 0.32 nm matching to the (111) planes of $Cd_{0.5}Zn_{0.5}S$ (Fig. 10k). The photocatalytic productivity of Cu-MOF, $Cd_{0.5}Zn_{0.5}S$, and their compositie (CZSM-15) was evaluated under visible light. Cu-MOF exhibited negligible HER, but $Cd_{0.5}Zn_{0.5}S$ demonstrated a modest HER rate of 5301 μmol g^{-1} h^{-1}. The CZSM-15 composite markedly boosted H_2 generation, attaining a rate 3.6 times greater than that of $Cd_{0.5}Zn_{0.5}S$ alone, attributable to the creation of heterojunctions that promoted electrons-holes separation and boosted active sites. Excessive Cu-MOF diminished efficiency by obstructing light absorption. Stability experiments demonstrated steady HER throughout four cycles, signifying the exceptional stability of CZSM-15 (Fig. 10l). Furthermore, the CZSM-15 composite exhibited a significant increase in HER efficiency and remarkable stability, sustaining constant performance throughout numerous cycles, therefore positioning it as a viable catalyst for effective HER. Furthermore, Sun et al. [241] prepared surface pores among MOFs and covalent organic frameworks (COFs) to create a photocatalyst. Pt NP was enclosed in the surface pores of Ti-MOF@Pt and the hydrophobic DM-LZU1 shell of the nanocomposite. Pt helped charge separately on photoactive Ti-MOF, whereas DM-LZU1 enriched reactants. Interfacial pores worked as nanoreactors, accelerating electron and mass transfer and photocatalytic performance (Fig. 10m). SEM analysis revealed smooth octahedral Ti-MOF. As DM-LZU1 developed on Ti-MOF, it formed a core-shell structure, enclosing it (Fig. 10n). TEM Ti-MOF@Pt@DM-LZU1 demonstrated hydrogenation of olefins under VL, converting styrene to ethylbenzene with over 99% selectivity in 40 minutes and a high TOF value of 577 h^{-1} depending on Pt concentration (Fig. 10o, p). The linear conversion rate verified catalyst stability. The reactivity was triggered by Ti-MOF@Pt@DM-LZU1 using H_2 as the proton resource. Control studies showed the importance of Pt NP and light irradiation. Ti-MOF enhanced hydrogenation by transferring electrons to Pt NPs, while the DM-LZU1 shell hindered unwanted electron transfer, ensuring catalyst efficiency without Pt leaching. The core-shell configuration was confirmed by Ti-MOF encapsulation in DM-LZU1. Additionally, the Ti-MOF@Pt@DM-LZU1 catalyst showed excellent selectivity and conversion rates while successfully hydrogenating various olefins. Allylbenzene, similar to styrene, was completely transformed into propylbenzene with over 99% selectivity in 40 minutes. Nonetheless, the catalyst exhibited markedly reduced reaction (25% conversion) towards internal C=C bonds, such as in trans-β-methylstyrene, attributable to the confinement impact of the COF shell, which limits molecular rotation and accessibility to Pt NPs. The catalyst effectively transformed aliphatic olefins such as cyclohexene and 1-octene into alkanes. Moreover, it selectively hydrogenated C=C bonds in 5-hexen-2-one while preserving C=O bonds, underscoring its potential for site-selective hydrogenation in diverse applications (Fig. 10q). Their research introduces an innovative idea for synthesizing the diverse photocatalysts exhibiting significant activity.

3.7. Quantum dots

Quantum dots (QDs) are nanoscale semiconductor particles, generally determined between 2 and 10 nm, exhibiting distinctive optical and electronic properties due to quantum confinement effects [242]. The incorporation of QDs into MOFs markedly improves photocatalytic efficiency by using the excellent light absorption and charge carrier dynamics of QDs alongside the substantial surface area and adjustable porosity of MOFs [243]. QDs enhance the light absorption spectrum of MOFs, expanding it into the visible and near-infrared regions, which increases light harvesting production [211,244]. QDs promote efficient charge separation and transfer, thus decreasing electrons-holes recombination rates and improving photocatalytic performance [123,245,246]. The tunable bandgap facilitates precise modification of the electronic structure of MOFs, thus optimizing photocatalytic reactions for targeted applications. The interaction between QDs and

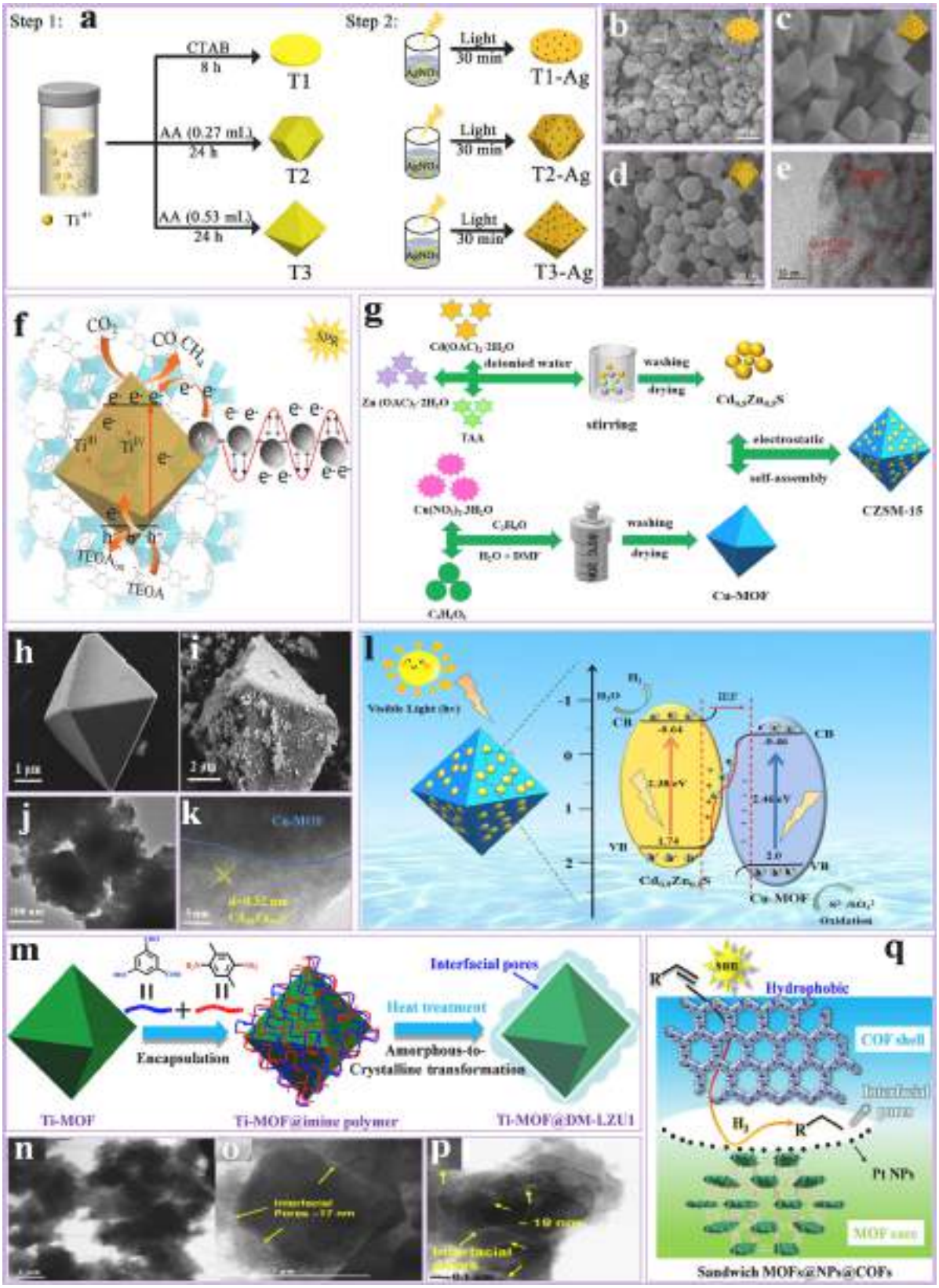

Fig. 10. (a) Synthesis process; (b–d) FESEM; (e) TEM analysis of Ag-loaded catalysts; (f) Schematic representation of T_3-Ag for photocatalytic CO_2RR, reproduced with permission from ref [239] Copyright © 2022, American Chemical Society. (g) Synthesis process; (h, i) SEM; (j) TEM; (k) HRTEM analysis of Cu-MOF/$Cd_{0.5}Zn_{0.5}S$ composites; (l) Cu-MOF/$Cd_{0.5}Zn_{0.5}S$ composites under visible light and feasible photoreaction process, reproduced with permission from ref [240] Copyright © 2023, Elsevier. (m) Synthesis process; (n) SEM; (o, p) TEM analysis of Ti-MOF@DM-LZU1; (q) The proposed photocatalytic mechanism of Sandwich MOFs@NPS@COFS, reproduced with permission from ref [241] Copyright © 2020, American Chemical Society.

MOFs facilitates the synthesis of advanced photocatalysts characterized by substantial productivity, selectivity, and stability [247]. In this regard, Ma et al. [248] synthesized a composite photocatalyst, PQ-CDs6.67@Cu-TCA, by embedding 9,10-phenanthraquinone (9,10-PQ) enhanced CQDs (PQ-CDs) inside Cu-TCA (TCA = 4,4',4''-nitrilotribenzoic acid). The covalent link among CQDs, the Cu paddle-wheel configuration, and 9,10-PQ facilitate efficient electron routes, improving electron transport and reducing carrier recombination. This catalyst exhibited an elevated electron absorption rate of 393.98 μmol·g^{-1}·h^{-1} and a CH_4 production of 44.43 μmol·g^{-1}·h^{-1} with a selectivity of 90.22%, surpassing several carbon material/MOF heterojunctions in photocatalytic CO_2RR effectiveness (Fig. 11a). The SEM analysis of $CQDs_{3.24}$@Cu-TCA exhibits a smooth octahedral shape with a grain size of around 500 nm, akin to Cu-TCA (Fig. 11b). No CQDs are seen on the surface, since they are enclosed inside the cavities of Cu-TCA, as proven by TEM investigation (Fig. 11c). The TEM analysis shows homogenous CQDs measuring 1.83 ± 0.32 nm, indicating effective encapsulation inside the Cu-TCA structure (Fig. 11d). The photocatalytic CO_2RR effectiveness of the $CQDs_{3.24}$@Cu-TCA heterojunction was evaluated in a CO_2-saturated MeCN/H_2O mixture using TEA as a hole scavenger under 300 W Xe lamp irradiation. Under optimal conditions, CO and CH_4 were the primary carbon products identified, with no H_2 or liquid products discovered, therefore validating photocatalytic CO_2RR. Control studies devoid of light, catalyst, CO_2, or H_2O exhibited no product production, underscoring the reaction stability on these materials. An experiment using the ^{13}C isotope further substantiated CO_2 as the carbon source, affirming that CO and CH_4 originated via photocatalytic CO_2RR. The PQ-$CQDs_{6.67}$@Cu-TCA composite demonstrated exceptional photocatalytic CO_2RR effectiveness, attaining CH_4 and CO generation rates of 44.43 and 19.27 μmol·g^{-1}·h^{-1}, respectively, with an electron consumption rate (Rele) of 393.98 μmol·g^{-1}·h^{-1}, which is 2.47 times more than that of $CQDs_{6.73}$@Cu-TCA. The elevated CH_4 selectivity (90.22%) was ascribed to the effective CO_2 methanation facilitated by PQ-CQDs. The apparent quantum efficiency (AQE) at 700 nm was 3.35%, surpassing several carbon/MOF-based photocatalysts. The stability experiments indicated that PQ-$CQDs_{6.67}$@Cu-TCA preserved 95.4% of its initial Rele after 30 cycles, sustaining structural integrity and morphology, hence demonstrating its exceptional stability during photochemical CO_2 reduction reaction (Fig. 11e). Their research combines electron-hole dissociation and remixing in CQDs@MOF photocatalysts to optimize the use of electrons provided by CQDs, offering insights for the engineering of advanced MOF-based photocatalysts. Similarly, Qin et al. [249] prepared a material of MXene QDs (Ti_3C_2-QDs) and a 2D nickel MOF (Ni-MOF) by a facile self-assembly approach to create type II heterostructures to improve photocatalytic N_2RR. The Ti_3C_2-QD/Ni-MOF heterostructure exhibited enhanced light absorption and surface charge transfer, attaining a significant NH_3 production rate of 88.79 μmol g_{cat}^{-1} h^{-1}. The synthesis of Ti_3C_2-QD/Ni-MOF heterostructure included etching Ti_3AlC_2 powder to eliminate Al layers, followed by ultrasonication to generate 2D Ti_3C_2 microsheets (Fig. 11f). Ti_3C_2 QDs were subsequently produced using a hydrothermal technique with DMF intercalation. Ultimately, Ti_3C_2-QD/Ni-MOF composites were prepared by the assembly of Ti_3C_2 onto Ni-MOF employing electrostatic interaction and prolonged sonication. The resultant heterojunctions, designated as 5MX-MOF, 7MX-MOF, 9MX-MOF, and 11MX-MOF, exhibited homogeneous 2D NS with uniformly dispersed Ti_3C_2 QDs. SEM, TEM, and HRTEM investigations demonstrated close interaction between Ti_3C_2-QDs and Ni-MOF, with point defects on Ti_3C_2 surfaces serving as catalytic sites and composition of Ni, Ti, and C (Fig. 11g–j). The photocatalytic N_2RR of Ti_3C_2-QD/Ni-MOF heterostructures were evaluated under simulated visible light. Among the samples, 9MX-MOF had the greatest NH_3 production of 88.79 μmol g^{-1} h^{-1}, surpassing 11MX-MOF, 7MX-MOF, 5MX-MOF, and Ni-MOF. The peak solar-to-ammonia performance was 0.139%. Control tests verified that NH_3 generation resulted from N_2 fixation instead of environmental influences since no substantial NH_3 was seen under Ar or dark circumstances. Isotopic labeling using $^{15}N_2$ and ^1H NMR corroborated the production of NH_3 following N_2 reduction. The 9MX-MOF exhibited consistent efficiency across several cycles, indicating commendable photostability. In-situ FTIR revealed nitrogen-related functional groups, including NH_4^+/NH_3 and adsorbed N_2Hy species, therefore verifying the process intermediates during N_2 photofixation (Fig. 11k). Their research provides a prototype material for surface design and establishes a novel approach for the rational engineering of effective photocatalysts for the N_2RR. Furthermore, Ding et al. [250] synthesized a $Cs_3Bi_2Br_9$/Bi-MOF composite by in-situ synthesis of $Cs_3Bi_2Br_9$ QDs on Bi-MOF NS using shared bismuth atoms. The improved composite $3Cs_3Bi_2Br_9$/Bi-MOF exhibited superior CO_2 capture and conversion efficiency, with a CO_2-to-CO transition yielding of 572.24 μmol g^{-1} h^{-1} under 300 W Xe lamp irradiation. The material exhibited commendable stability after five cycles in humid air, with a little reduction in performance. Mechanistic investigations demonstrated that the atomic-scale interaction between $Cs_3Bi_2Br_9$ and Bi-MOF improves QDs dispersion and facilitates surface charge transfer, enhancing CO_2 photoreduction effectiveness (Fig. 11l). TEM investigations elucidated the shape and crystalline structure of the $Cs_3Bi_2Br_9$/Bi-MOF composite. The Bi-MOF comprises narrow NS of about 3 μm in length, 500 nm in width, and 4.1 nm in thickness. $Cs_3Bi_2Br_9$ exhibits homogeneous quasi-spherical NP having a median diameter of 5.5 nm. In the $3Cs_3Bi_2Br_9$/Bi-MOF composite, $Cs_3Bi_2Br_9$ QDs (about 4.1 nm) are evenly affixed to the Bi-MOF surface, augmenting the performance of photocatalysts. The reduced Bi concentration in the composite indicates the sharing of Bi atoms among $Cs_3Bi_2Br_9$ and Bi-MOF (Fig. 11m–p). The suggested process for CO_2 photocatalytic conversion in $Cs_3Bi_2Br_9$/Bi-MOF entails the in-situ formation of $Cs_3Bi_2Br_9$ QDs on Bi-MOF NS, establishing a proximate interface via shared bismuth atoms. This design optimizes photoexcited carrier transfer, generates defective sites, and promotes the distribution and stability of $Cs_3Bi_2Br_9$ QDs. The S-type band alignment promotes electron transport from the CB of $Cs_3Bi_2Br_9$ to the VB of Bi-MOF, with Bi species functioning as electron shuttles, maintaining redox capabilities (Fig. 11q, r). This configuration facilitates electrons-holes separation, promotes defect development, expands light absorption, and boosts CO_2RR efficiency and stability. The in-situ fabrication of heterostructures with atomic-level interaction among inorganic semiconductors and MOFs is anticipated to enhance the production of lead-free halide perovskite/MOF-derived photocatalysts. This method can potentially strengthen their uses in electronics, solar cells, photodetectors, and photocatalysts, facilitating broader utilization of these materials across diverse technologies.

3.8. Hollow

Hollow structures in MOFs are defined as structure featuring void interiors enclosed by porous shells [251]. The distinct morphologies markedly improve photocatalytic performance through enhanced light consumption, increased reactant diffusion, and greater accessibility of active sites [252]. The hollow cavities function as light-trapping regions, extending light-matter interaction and facilitating enhanced photon absorption, which enhances photocatalytic performance [76]. The shell structure offers numerous active sites on both the inner and outer surfaces, enabling various reaction pathways [43]. The enhanced mass transfer and diffusion dynamics within the hollow structure mitigate transport limitations, facilitating effective accessibility of reactants to catalytic sites [253,254]. Hollow MOFs demonstrate decreased bulk density and improved stability under reaction conditions as a result of their distinctive structural characteristics [255–257]. For example, Fan et al. [258] synthesized Ce-doped $ZnIn_2S_4$ photocatalysts featuring hollow nanocages by a one-step hydrothermal process, using Ce-based MOFs (Ce-MOFs) as both the template and source of Ce ions. The Ce-MOFs enable concurrent Ce doping and the synthesis of $ZnIn_2S_4$ hollow nanocages composed of ultrathin NS subunits. The resultant photocatalysts exhibit a distinctive tetrakaidecahedron morphology derived

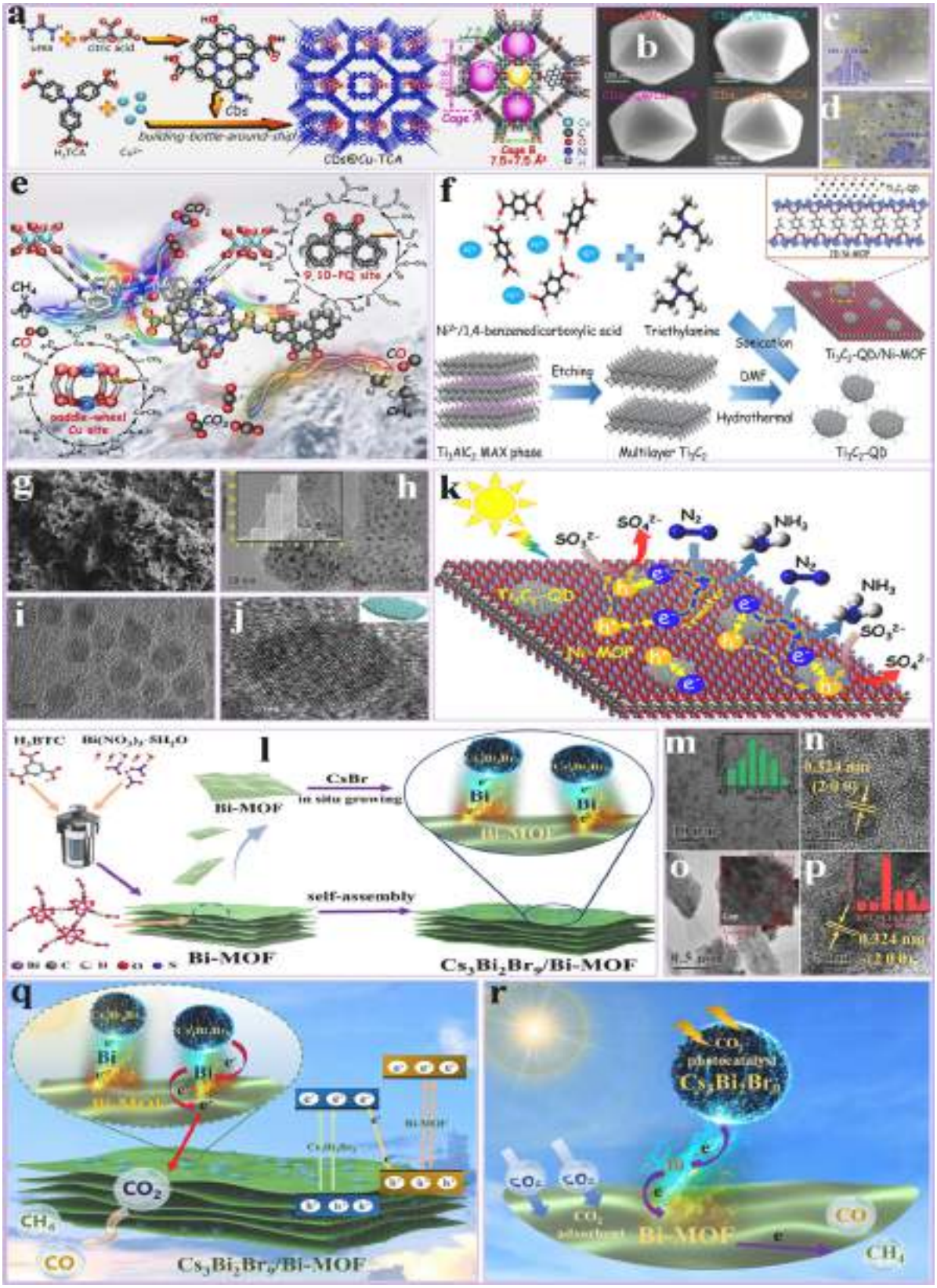

Fig. 11. (a) Synthesis process; (b) SEM; (c, d) TEM analysis of CQDs and CDs@Cu-TCA composites; (e) The graphical illustration of PQ-CQDs$_{6.67}$@Cu-TCA illustrates the dual-catalytic sites and simultaneous electron transfer channels for photocatalytic CO_2 reduction, reproduced with permission from ref [248] Copyright © 2024, Elsevier. (f) Synthesis process; (g) SEM; (h, i) TEM; (j) HRTEM analysis of ultrafine Ti_3C_2-QD/Ni-MOF; (k) Diagram illustrating the spatial charge separation and transport during the photocatalytic reduction of N_2 using Ti_3C_2-QD/Ni-MOF, reproduced with permission from ref [249] Copyright © 2020, American Chemical Society. (l) Synthesis process; (m–p) TEM analysis of $Cs_3Bi_2Br_9$/Bi-MOF composite; (q, r) Photocatalytic method for CO_2 conversion using the $Cs_3Bi_2Br_9$/Bi-MOF composite, reproduced with permission from ref [250] Copyright © 2023, American Chemical Society.

from the Ce-MOF template and possess a nonspherical 3D hollow nanostructure with a shell formed of ultrathin NS. The synthesis of Ce-doped $ZnIn_2S_4$ (ZIS) hollow nanocages entails a two-step process. Initially, large-pore tetrakaidecahedron Ce-MOFs are produced. Ce-doped ZIS hollow nanocages are synthesized by a one-step solvothermal process using Ce-MOFs as both the template and Ce precursor. Thioacetamide (TAA) degrades Ce-MOF templates throughout the process, enabling the sequential formation of ultrathin ZIS nanosheets. The resultant Ce-doped ZIS nanocages preserve the tetrakaidecahedron morphology of the Ce-MOF template, with a shell constructed from ultrathin NS subunits. ICP analysis indicates that elevated Ce doping results in a progressive reduction of the Zn:In atomic ratio, suggesting that Ce may substitute for Zn in the ZIS lattice (Fig. 12a). The structural features of the as-prepared Ce-MOFs were analyzed using FESEM and TEM. FESEM analysis demonstrates that the Ce-MOFs possess a consistent tetrakaidecahedron morphology, with an average dimension of

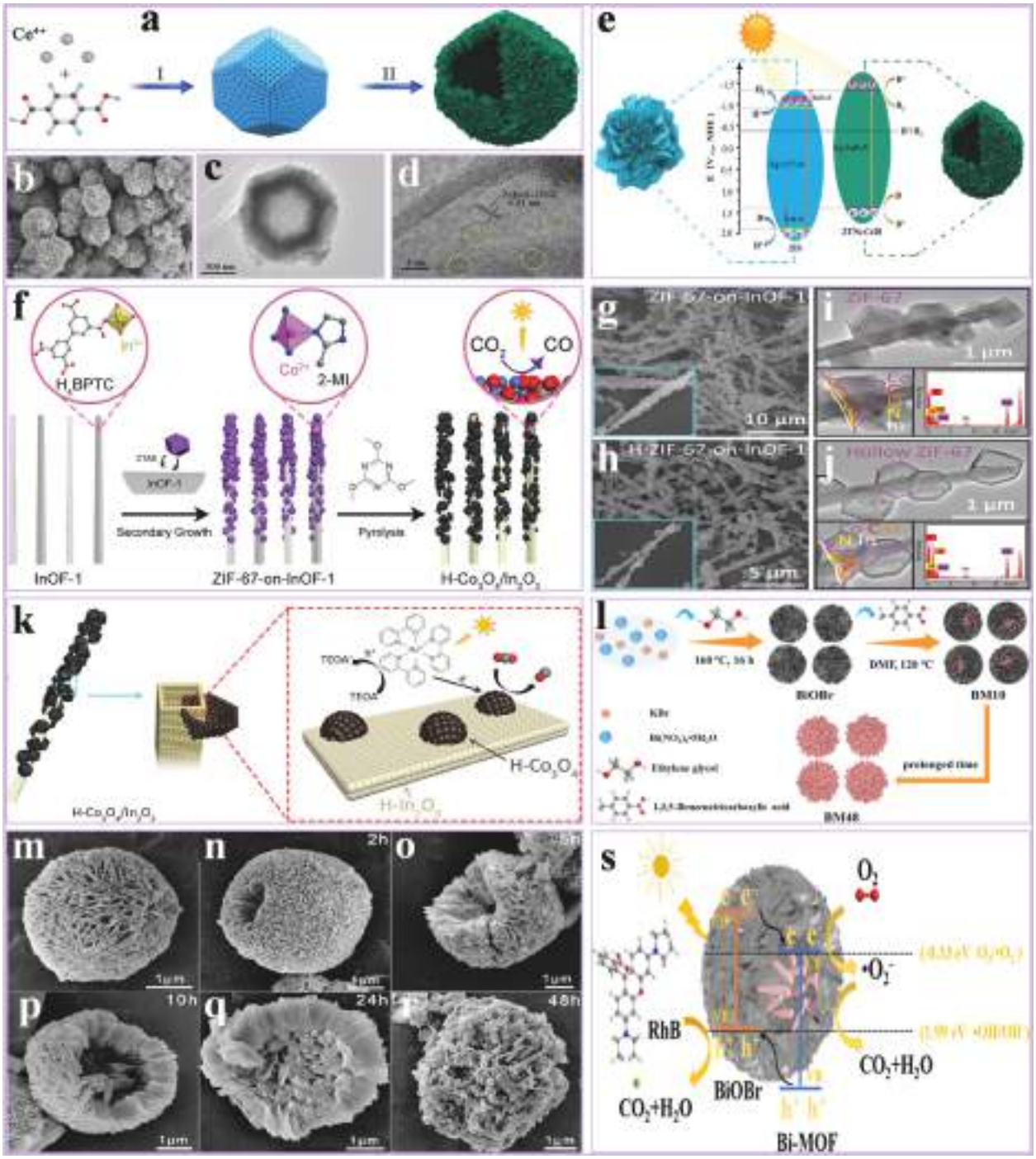

Fig. 12. (a) Synthesis process; (b) FESEM; (c, d) TEM analysis of hierarchical ZTNs-Ce20 tetrakaidecahedron hollow nanocages; (e) Schematic representation of the band structure of the pristine ZIS and ZTNs-Ce20 samples, reproduced with permission from ref [258] Copyright © 2022, John Wiley and Sons. (f) Synthesis process; (g, h,) SEM; (i, j) TEM analysis of MOF-on-MOF-based hollow bimetallic photocatalyst H-Co_3O_4/In_2O_3 for the CO_2RR; (k) Projected catalytic route for the photoreduction of CO_2 to CO over H-Co_3O_4/In_2O_3, reproduced with permission from ref [259] Copyright © 2023, John Wiley and Sons. (l) Synthesis process; (m–r) SEM analysis of 3D Hollow BiOBr@Bi-MOF and Bi-MOF; (s) Suggested charge separation and transfer routes in BiOBr@Bi-MOF heterostructure under visible light, reproduced with permission from ref [260] Copyright © 2021, American Chemical Society.

around 900 nm, characterized by a homogeneous structure and porous surface (Fig. 12b). TEM analysis further corroborates that these Ce-MOFs are solid and advanced magnification images emphasize the orderly arrangement and homogenous of channels on their surfaces (Fig. 12c, d). The superior photocatalytic efficiency of ZTNs-Ce20 is ascribed to the improved separation of photogenerated carriers resulting from Ce loading, which significantly modulates the band structure. Mott–Schottky plots indicate that ZTNs-Ce20 exhibits a higher negative flat-band potential and an elevation in VB and CB positions relative to pure ZIS. This transition leads to enhanced mobility and increased use of photogenerated holes, promoting more effective hydrogen ion reduction and H_2 production during photocatalysis. The porous hierarchical design and cerium-induced modifications to the band structure enhance light absorption and charge dispersion, substantially enhancing the catalytic activity of ZTNs-Ce20 (Fig. 12e). Their research emphasizes the approach of using MOFs as both a template and doping to fabricate nonspherical hollow nanocage photocatalysts having elemental loading, hence facilitating the development of novel and efficient photocatalysts. Similarly, Han et al. [259] synthesized MOF-based hollow bimetal oxide nanocomposites for effective CO_2 photoreduction. A ZIF-67-on-InOF-1 heterostructure was created by depositing Co-drived ZIF-67 onto InOF-1 nanorods. Post-acid etching, the material evolved into a hollow structure with an expanded surface area, and the resultant H-Co_3O_4/In_2O_3 displayed many heterogeneous surfaces with increased active sites. The energy band structure is compatible with the photosensitizer $[Ru(bpy)_3]Cl_2$, resulting in a substantial CO production of 4828 ± 570 μmol h^{-1} g^{-1} and consistent activity across six successive runs, demonstrating robust photocatalytic performance. A distinctive MOF-on-MOF heterojunction, ZIF-67-on-InOF-1, was synthesized using crystal engineering. InOF-1 exhibits octahedral In(III) centers, with Co(II) ions from ZIF-67 being well-distributed owing to the strong electronegativity of the O atoms in InOF-1. This structure facilitates the effective proliferation of ZIF-67 on InOF-1. Incorporating ZIF-67 enhanced the adsorption ability and micropore content of InOF-1 (Fig. 12f). STEM analysis verified the effective production of a heterojunction in which ultra-long InOF-1 nanorods are fully encased by ZIF-67 elements (Fig. 12g, h). The incorporation of the powders in ethanol emerged as colorless and clear, indicating robust interfacial forces among the MOFs. Cyanuric acid chemically fixed the material to improve surface area and mass transfer. Although some partial separation was caused by elevated temperatures and etching, the hierarchical design of H-ZIF-67-on-InOF-1 was sustained (Fig. 12i, j). The photocatalytic efficiency was assessed in a mixed solution including triethanolamine (TEOA) and $[Ru(bpy)_3]Cl_2$ of the samples analyzed—H-Co_3O_4, H-In_2O_3, and a physical combination of H-Co_3O_4 and In_2O_3—H-Co_3O_4/In_2O_3 exhibited the greatest CO productivity rate of 4828 ± 570 μmol h^{-1} g^{-1}. H-Co_3O_4 yielded 1644 ± 210 μmol h^{-1} g^{-1}, while H-Co_3O_4+In_2O_3 generated 2420 ± 444 μmol h^{-1} g^{-1}, and H-In_2O_3 exhibited little activity. H-Co_3O_4/In_2O_3 showed a preference of 80% and an AQE of 0.59% for CO production at 450 nm. The material exhibited outstanding CO_2 photoreduction effectiveness for 2 hours and demonstrated stability over six recycling trials (Fig. 12k). Their research may be expanded to include the rational engineering and mechanical manipulation of MOFs precursors and their derivatives as effective and resilient catalysts for pollutant degradation, WS, fuel cells, and further applications. Furthermore, Xu et al. [260] fabricated a 3D hollow BiOBr@Bi-MOF microsphere via a self-assembly technique with regulated dissociation kinetics of a BiOBr self-sacrificial substrate. They modulated response time and coordination capacity to control the residual BiOBr and Bi-MOF production. The porous design created by the Oswald ripening process improved the division of photogenerated electron−hole pairs and the adsorption of dye. This led to a substantial enhancement in the photocatalytic degradation effectiveness of RhB, rising from 56.4% with BiOBr to 99.4% with the modified BiOBr@Bi-MOF microsphere (Fig. 12l). The 3D hollow BiOBr@Bi-MOF heterojunction was prepared to employ an in-situ self-assembly technique, using BiOBr microspheres as both the template and the Bi^{3+} precursor. The response time was set to modify the comparative amounts of BiOBr and Bi-MOF. Initially, the BiOBr surface became roughened and partly dissolved; with prolonged reaction time, a hollow shape developed owing to localized Ostwald ripening. SEM validated the core@shell design, exhibiting lattice spacings aligned with BiOBr and Bi-MOF (Fig. 12m–r). The 3D hollow BiOBr@Bi-MOF heterojunction exhibited excellent photocatalytic degradation kinetics for RhB dye, according to a pseudo-first-order dynamic model with a rate efficiency of 0.07009 min^{-1}, markedly surpassing that of pure BiOBr and Bi-MOF. Stability tests demonstrated exceptional stability, with no notable decrease in deterioration rate after five cycles. The photocatalytic process entails the adsorption of RhB on BiOBr@Bi-MOF, whereby photoexcited electrons and holes promote electron transfer from BiOBr to Bi-MOF. The lower energy CB of Bi-MOF facilitates the reduction of oxygen to $\bullet O_2$ radicals, while the holes efficiently oxidize RhB, hence improving degradation effectiveness (Fig. 12s). Their study enhances the preference of semiconductor/MOF hetero-nanocrystals by considering design and adaptable synthesis.

3.9. Hierarchical

Hierarchical structures in MOFs consist of structure featuring multiscale porosities, which include micropores, mesopores, and macropores [261]. These structures improve photocatalytic performance by integrating various pore sizes, which improve reactant diffusion, light harvesting, and availability of active sites [262]. The interrelated pore structures enable fast mass transfer, ensuring the effective transfer of reactants to catalytic sites and prompt removal of reaction byproducts [263,264]. The existence of larger pores enhances light scattering, which increases light-matter interaction and improves photon absorption. In contrast, smaller pores provide an extensive surface area and localized active sites conducive to catalytic processes [265,266]. Hierarchical structures improve charge carrier dynamics by shortening diffusion pathways, decreasing recombination, and facilitating the effective separation and transport of photoinduced charge carriers [267,268]. In this regard, Rao et al. [269] examined a range of Cu/C composites produced by calcining alkylpyrogallol[4]arene (PgCs) metal-organic nanocapsule (MONC) precursors at different temperatures and times. The degradation of methyl violet (MV) dye assessed the photocatalytic performance of these composites. Among the composites evaluated, Cu/C-1000–4, calcined at 1000 °C for 4 hours, exhibited the highest photocatalytic degradation efficiency, achieving a 96.30% removal of MV dye. The degradation process of MV by Cu/C-1000–4 was investigated further using LC-MS (Fig. 13a). The morphologies and internal structures of Cu/C composites (Cu/C-800–4, Cu/C-900–4, Cu/C-1000–4, Cu/C-1100–4, Cu/C-1000–2, and Cu/C-1000–8) were examined using SEM. All samples maintained an elliptical shape but had varying surface textures. Cu/C-900–4 had a rougher surface than Cu/C-800–4, which displayed tiny Cu particles. Cu/C-1100–4 exhibited a porous morphology with substantial Cu particles and considerable surface degradation (~350 nm). The results demonstrate that calcination temperatures over 800 °C caused the degradation of calkylpyrogallol[4]arene metal-organic nanocapsules. The SEM analysis of Cu/C-1000–4 showed densely packed Cu particles with lattice spacing matching the (111) facet of metal Cu. With the elevation of the calcination temperature, the dimensions of Cu particles on the surface increased (Fig. 13b). The photocatalytic performance of several Cu/C composites on MV dye under visible light showed considerable degradation, with Cu/C-1000–4 attaining the greatest rate at 96.30%, attributed to its excellent surface area and electrons-holes separation characteristics. Performance fluctuated based on light source, time, dye concentration, catalyst dose, and active sites. LC-MS/MS analysis revealed intermediates resulting from deamination and functional group loss, suggesting potential degradation mechanisms that require additional confirmation (Fig. 13c). Their research presents a novel photocatalyst developed from MOFs, demonstrating excellent efficiency in environmental applications, particularly

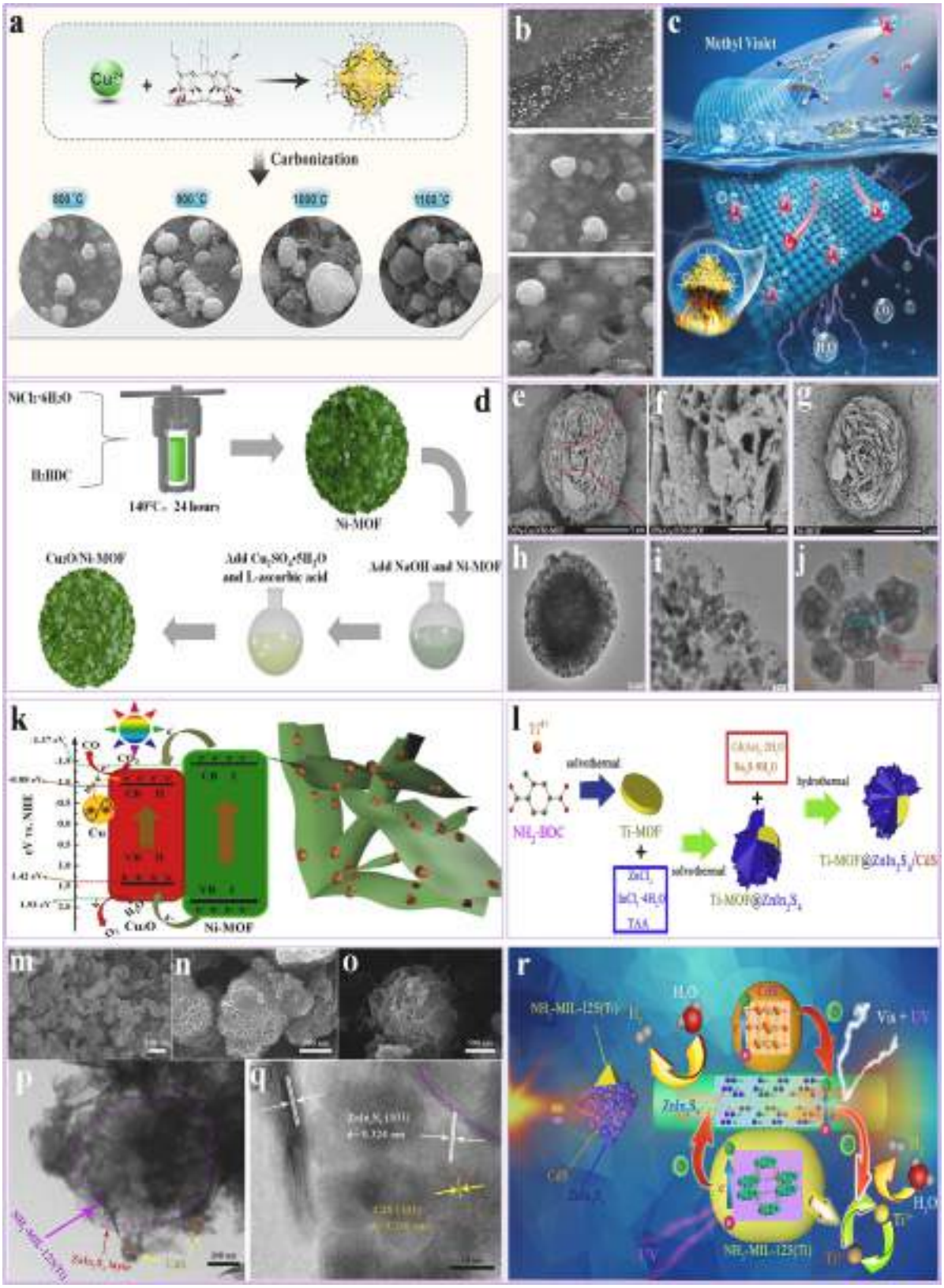

Fig. 13. (a) Synthesis process; (b) SEM analysis of Cu/C composites; (c) Graphical depiction of the possible photocatalytic performance of MV, reproduced with permission from ref [269] Copyright © 2022, Elsevier. (d) Synthesis process; (e–j) SEM analysis of Cu_2O/Ni-MOF; (k) Simulated electron transfer mechanism in 30%-Cu_2O/Ni-MOF composite CO_2RR under visible light, reproduced with permission from ref [270] Copyright © 2023, Elsevier. (l) Synthesis process; (m–o) SEM; (p) TEM; (q) HRTEM analysis of NH_2-MIL-125(Ti)@$ZnIn_2S_4$/CdS hierarchical tandem heterostructures photocatalyst; (r) The proposed photocatalytic HER of NH_2-MIL-125(Ti)@$ZnIn_2S_4$/CdS, reproduced with permission from ref [271] Copyright © 2020, Elsevier.

in the removal of organic dyes from wastewater, and elaborates on the structure and fabrication of these porous composites. Similarly, Jiang et al. [270] synthesized a hierarchical Cu_2O/Ni-MOFs material photocatalyst exhibiting local surface plasmonic resonance (SPR) characteristics by hydrothermal and water bath techniques. The surface plasmon resonance of Cu^0 improved light absorption and generated hot electrons, markedly enhancing photocatalytic activity owing to the hierarchical and heterostructure characteristics of composites. In the absence of a sacrificial agent, the CO production of the 30%-Cu_2O/Ni-MOF composite was 4.1 times more than that of Cu_2O and 11.1 times greater than Ni-MOF, indicating its enhanced effectiveness (Fig. 13d). The morphology and microstructure of the Ni-MOF and Cu_2O/Ni-MOF samples were analyzed using SEM. The Ni-MOF structure comprises stacked lamellar formations that create a 3D lamellar sphere about 5 μm in diameter, providing multiple active and heterogeneous nucleation sites, hence serving as an exceptional carrier material (Fig. 13e, f). In addition, the 30%-Cu_2O/Ni-MOF exhibits a uniform distribution of Cu_2O particles over the Ni-MOF surface, devoid of substantial agglomeration, hence creating a hierarchical structure (Fig. 13g). Upon meticulous examination, diminutive Cu_2O particles are equally distributed throughout the Ni-MOF surface, promoting the development of a heterostructure. The decrease in Cu_2O particle size after recombination is attributed to many nucleation sites on the Ni-MOF, inhibiting Cu_2O agglomeration (Fig. 13h–j). This structure augments the active sites of photocatalysts, surface area, and molecular transport, enhancing its effectiveness. The in-situ FT-IR investigation of the 30%-Cu_2O/Ni-MOF catalyst identified critical steps in the photocatalytic CO_2RR mechanism. Peaks associated with HCO_3, b-CO_3^{2-}, m-CO_3^{2-}, and COOH* groups were discerned, with the latter serving as essential intermediates in the transformation of CO_2 to CO. Adsorbed CO was discovered, and H_2O oxidation was noted, supplying electrons for the process. The suggested process entails the adsorption of CO_2 and H_2O on the catalyst, followed by separating electron-hole pairs upon exposure to visible light. Hot electrons produced by Cu NP transfer to provide H_2O and adsorbed CO*. Ultimately, CO* desorbs as free CO, with H_2O providing electrons and protons to maintain the process (Fig. 13k). Their research illustrates the key function of 3D hierarchical heterostructures and the surface plasmon resonance effect in enhancing photocatalytic performance, supporting the development of effective photocatalysts. Furthermore, Zhang et al. [271] synthesized defective-enrich, electron-enrich mesoporous NH_2-MIL-125(Ti)@$ZnIn_2S_4$/CdS hierarchical tandem heterostructures via two-step solvothermal and one-step hydrothermal techniques. The electron-rich surface facilitates active reactions, accelerates charge transfer and separation, and mitigates CdS photocorrosion. $ZnIn_2S_4$ serves as an intermediary between Ti-MOFs and CdS, promoting charge carrier dispersion and establishing tandem heterojunctions. The photocatalyst has a substantial surface area (~877.0 m^2/g) and a small bandgap (~1.84 eV), facilitating effective absorption of visible light. It demonstrates a substantial photocatalytic HER of 2.367 μmol/g/h and notable degradation efficiencies for 2,6-dichlorophenol (98.6%) and 2,4,5-trichlorophenol (97.5%) (Fig. 13l). SEM images show the hierarchical structure of $ZnIn_2S_4$ (ZIS), which possesses considerable interface energy and is suited for growing CdS or other photocatalysts. Upon the incorporation of CdS with TiM and ZIS, the surfaces exhibited increased roughness, indicating effective integration (Fig. 13m). SEM analysis of different TiM@ZIS weight ratios indicated that a higher ZIS content enlarged the TiM@ZIS size (Fig. 13n); nevertheless, an excess of ZIS compromised the surface, diminishing electron separation performance and H_2 generation (Fig. 13o). Various CdS weight ratios were coupled with 45% TiM@ZIS, and SEM analysis indicated negligible changes. The TEM and HRTEM analysis of TiM@ZIS and TiM@ZIS/CdS validated the establishment of core-shell structures and heterostructures (Fig. 13p). The lattice fringes, measuring 0.324 nm for ZIS and 0.336 nm for CdS, were attributed to their corresponding crystal planes, therefore confirming the effective synthesis of TiM@ZIS/CdS tandem heterojunctions (Fig. 13q). The photocatalytic degradation effectiveness of the TiM@ZIS/CdS heterojunction catalyst for 2,6-dichlorophenol (DCP) and 2,4,5-trichlorophenol (TCP) achieved 98.6% and 97.5%, respectively, exceeding the efficiency of other photocatalysts such as TiM, TiM/CdS, ZIS/CdS, and TiM@ZIS. The H_2 generation experiments under AM 1.5 irradiation showed that TiM@ZIS/CdS had the greatest rate of 2.367 μmol g^{-1} h^{-1}. The improved efficiency was ascribed to the extensive surface area of catalysts, active sites, and effective charge separation and transference. The ideal ratio for TiM@ZIS was 45%, while further optimization of TiM@ZIS/CdS indicated that 45% TiM@ZIS joint with 7% CdS yielded the highest HER at 2.306 μmol g^{-1} h^{-1}. Excessive ZIS or CdS diminished performance by impairing the surface reaction and decreasing charge stability (Fig. 13r). Their study used hierarchical tandem heterojunctions to leverage electron enrichment, therefore enhancing surface reactions, expediting electron-hole pair separation, and augmenting photocatalytic HER and pollutant degradation. Nonetheless, several electron transference channels are present, necessitating more investigation into innovative methods.

3.10. Sea urchin-like

Sea urchin-like morphology in MOFs is defined by radially organized nanostructures that radiate from a central core and resemble a sea spines urchin [272]. This distinct morphology provides a large surface area and numerous active sites, essential for effective photocatalytic performance [136]. The radial structure enhances light scattering and harvesting, thus prolonging light-matter interaction and optimizing photon absorption [139,273]. The open structure facilitates reactant diffusion and reduces charge carrier recombination by offering shorter routes for separating and transporting photoinduced electrons and holes [138,274]. These properties make sea urchin-like MOFs very useful for applications requiring significant catalytic effectiveness and stability, such as pollutant degradation, WS, and CO_2RR [140]. For example, Li et al. [275] synthesized a composite catalyst, sea urchin-like Zn-MOF-74@g-C_3N_4, for the generation of H_2O_2 by an efficient two-electron OER. The catalyst comprises spherical Zn-MOF-74 and graphite phase carbon nitride nanoneedles with higher-curvature tips, which provide a "lightning rod impact" to improve charge transfer by facilitating electron movement. The integration of piezo-photocatalysis with a step-scheme heterostructure generates a dual electric field, markedly enhancing the division and transition of photo-excited carriers (Fig. 14a). SEM and TEM were used to examine the structural features of Zn-MOF-74, g-C_3N_4, and the composite Zn-MOF-74@g-C_3N_4. Unadulterated Zn-MOF-74 exhibited a uniform, spherical morphology; however, further self-assembly resulted in the deposition of organized, needle-like g-C_3N_4 nanoneedles, culminating in a sea urchin-like morphology having a median diameter of 10 μm (Fig. 14b–d). TEM analysis indicated that the needle-like g-C_3N_4 exhibited variability in length and size on the Zn-MOF-74 surface. This sea urchin-like structure amplifies H_2O_2 generation by boosting and enhancing contact with the piezoelectric field, thus enhancing the ORR efficiency (Fig. 14e–g). The suggested process for H_2O_2 synthesis by Zn-MOF-74@g-C_3N_4 under visible light and ultrasound entails piezo-photocatalysis. When disseminated in an aqueous mixture containing IPA and exposed to ultrasonic vibration, the Zn-MOF-74@g-C_3N_4 photocatalyst undergoes deformation, resulting in internal carrier disruption and the generation of an electric dipole owing to the alignment of positive and negative charge centers. This leads to polarization and the formation of an intrinsic electric field. Visible light stimulates photoexcited electrons, creating electron-hole pairs segregated by the internal electric field, inhibiting recombination. The S-scheme heterostructure promotes efficient remixing of electrons and holes, hence enhancing their usage. The piezoelectric action of g-C_3N_4 creates substantial charges and a polarization field, enhancing carrier separation and enhancing photocatalytic performance (Fig. 14h). Their novel method resulted in an increased H_2O_2 generation rate owing to the synergistic interplay of the lightening rod impact and piezo-photocatalysis. Similarly, He et al. [136] prepared a sophisticated

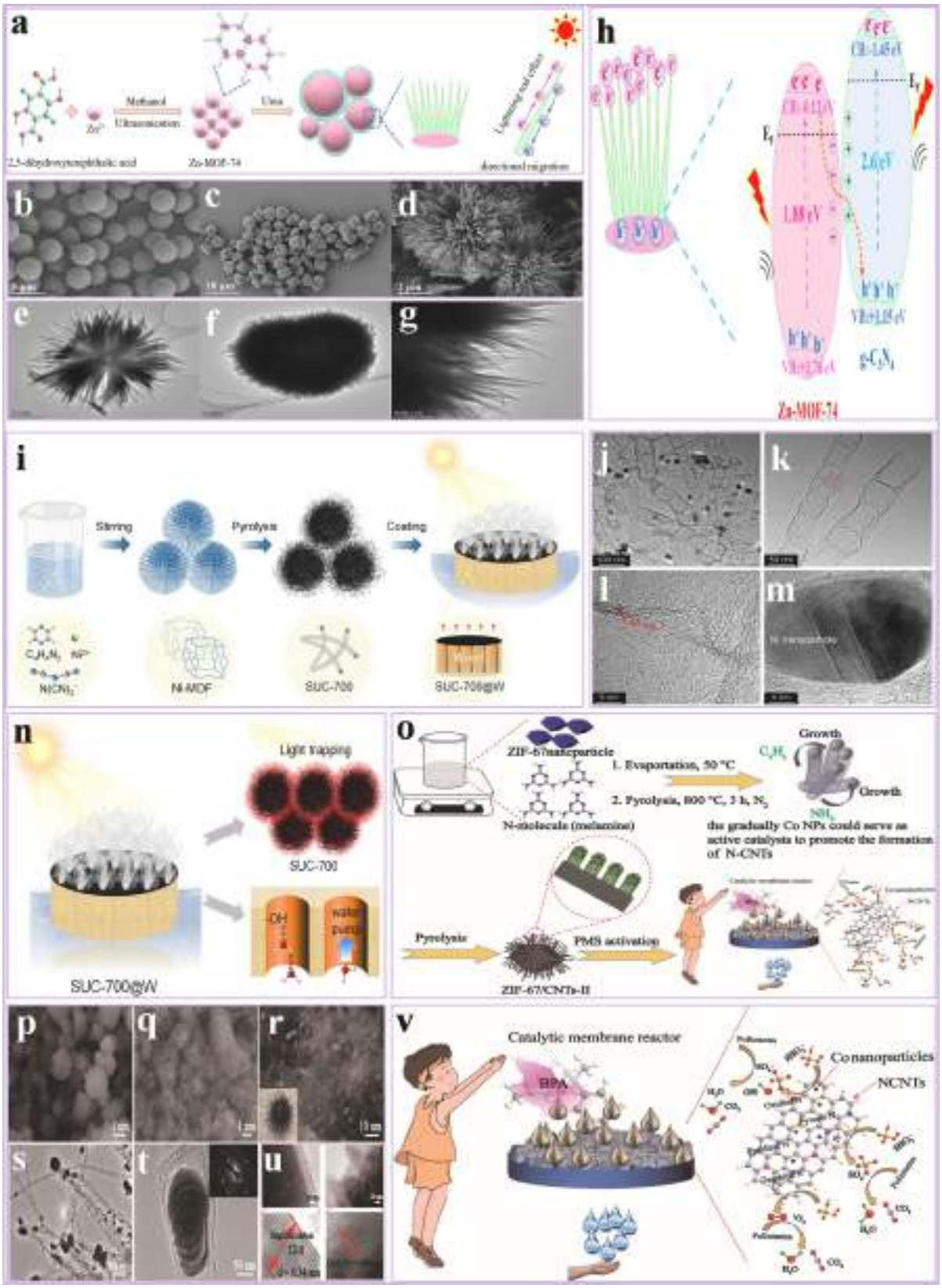

Fig. 14. (a) Synthesis process; (b–d) SEM; (e–g) TEM analysis of sea urchin-like Zn-MOF-74@g-C_3N_4; (h) The proposed route of ORR Zn-MOF-74@g-C_3N_4, reproduced with permission from ref [275] Copyright © 2024, Elsevier. (i) Synthesis process; (j–m) TEM analysis of SUC-x@W; (n) Mechanism on the surface solar steam production of SUC-700@W, reproduced with permission from ref [136] Copyright © 2021, Elsevier. (o) Synthesis process; (p–r) SEM; (s, t) TEM; (u) HRTEM analysis of ZIF-67/CNTs-II; (v) The potential degradation pathways of the ZIF-67/CNTs/PMS system for PMS activation, reproduced with permission from ref [140] Copyright © 2021, Elsevier.

bilayer solar evaporator by applying carbon components sourced through sea urchin-like MOFs onto wood. These carbon materials generated from MOFs have a sea urchin-like design, including bamboo-shaped CNT and nickel NP, improving light absorption and solar-to-thermal conversion efficiency. Nitrogen and oxygen dopants enhance the hydrophilicity of carbon material. The wooden base serves as thermal insulation and facilitates water channels, while hydrogen bonding between wood and water diminishes the enthalpy of water evaporation. The bilayer solar evaporator attains an evaporation efficiency of 2.07 kg m^{-2} h^{-1}, exhibiting remarkable scalability and enduring stability (Fig. 14i). TEM analysis of SUC-700 indicates the presence of metal NP (10–60 nm) and bamboo-shaped CNT (20–70 nm). The CNT has a bamboo-shaped design, and the graphite lattice at the bamboo junctions displays poor ordering with an interplanar distance of around 0.38 nm, which is more than that of ordinary graphite (0.34 nm), possibly attributable to nitrogen loading. Metal NP are encased in graphitic carbon, suggesting that the bamboo-shaped NT develops via an apical process (Fig. 14j–m). The suggested method for the surface solar steam production of SUC-700@W encompasses numerous significant variables. The SUC-700 has a sea urchin-like design, characterized by many CNT and nickel NP, which form microporous and mesoporous systems that improve light absorption and water porosity. This shape facilitates accessible pathways for effective water and vapor movement and enhances light harvesting via scattering mechanisms. The nitrogen and oxygen loading enhances the hydrophilicity of SUC-700. With 30 μm channels, Wood enables fast water movement by capillary action. The hydrophilic groups on SUC-700@W establish hydrogen bonds with water, resulting in free, intermediate, and bound water types. Intermediate water interacts with bound water, diminishing hydrogen bonds and lowering the energy required for evaporation. This theory is corroborated by an evaporation experiment using LiCl solution, which demonstrates that the Li^+ content of condensed water from SUC-700@W is 17 times more than that from evaporators without the material, suggesting that water vapor departs as water clusters (Fig. 14n). Their research underscores the promise of carbon materials produced from MOFs for solar evaporation in mitigating global freshwater scarcity. Future initiatives will improve evaporation rates, increase freshwater output, and innovate designs for ongoing freshwater generation. Furthermore, Ye et al. [140] devised a facile technique to synthesize a 3D carbon-derived hybrid resembling a sea urchin by N-molecule-induced pyrolysis of ZIF-67 nanocrystals. The composite was then incorporated into a poly(vinylidene fluoride) (PVDF) membrane by a phase inversion method, resulting in a ZIF-67/CNTs-II@PVDF catalytic membrane for bisphenol A (BPA) degradation. The efficiency of membrane is ascribed to integrating nitrogen-loaded CNT, encapsulated cobalt NP, elevated nitrogen doping, 3D porous designs, and many active sites. The ZIF-67/CNTs-II/PMS (peroxymonosulfate) system attained a 90.9% degradation rate of BPA in 25 minutes with no cobalt leaching, exceeding the performance of most current catalysts. The ZIF-67/CNTs-II@PVDF membrane effectively removed several persistent organic pollutants (Fig. 14o). The shape and structure of materials were analyzed using SEM and TEM. The progenitors of ZIF-67 had a distinct polyhedral morphology with smooth surfaces, in accordance with prior findings. Post-pyrolysis, ZIF-67/Cs retained its structure, although with some contraction. The ZIF-67/CNTs-II, synthesized at a 2:1 mass ratio, included substantial aggregates of N-doped CNTs with metal cobalt NPs at the center and multi-walled N-doped CNT as the outer layer. This structure was optimal for improving BPA decomposition owing to its extensive surface area (Fig. 14p–r). Conversely, ZIF-67/CNTs-I and ZIF-67/CNTs-III, fabricated with varying mass ratios, exhibited rougher surfaces and less efficient CNT morphologies. TEM analysis indicated that Co NP was localized at the tips of N-doped CNT (Fig. 14s, t), whereas HRTEM analysis demonstrated that these nanoparticles were encased in multilayered, graphitized carbon layers, enhancing electron transport and protecting the Co NP (Fig. 14u). The research assessed the catalytic effectiveness of several carbon-derived catalysts with varying nitrogen levels for the removal of BPA using PMS to produce ROS. PMS alone was ineffective, eliminating just around 8.64% of BPA in 40 minutes. ZIF-67/CNTs-II, exhibiting optimum N-doping, markedly surpassed alternatives by eliminating 98.7% of BPA in 40 minutes, accompanied by a high-rate constant of 0.0956 min^{-1}. ZIF-67/CNTs-I, ZIF-67/CNTs-III, and ZIF-67/Cs had BPA removal rates of 40.8%, 74.8%, and 79.8%, respectively. The leaching of cobalt ions was minimal for ZIF-67/CNTs-II (0.021 mg/L), indicating its enhanced stability and catalytic performance (Fig. 14v). Their study presented an efficient method for developing highly active catalytic membranes for practical environmental cleanup.

3.11. Monolith

Monolith morphology denotes a self-supporting, porous structure characterized by higher mechanical strength and interconnected systems [276]. This design facilitates effective mass transfer and optimizes active site exposure, thus improving catalytic and adsorption efficiency [277]. The stability and scalability of this system render it suitable for industrial applications that demand robust and repeatable efficiency [278]. Monolith in MOFs is very important to enhance photocatalytic performance. The interconnected porous structure promotes efficient mass transfer, facilitating the diffusion of reactants and products to and from active sites [143,279]. The substantial surface area of monoliths improves light absorption and increases the availability of active sites, which are essential for photocatalytic reactions [99,280,281]. For example, Niu et al. [282] synthesized a ZnO/polyacrylamide (ZnO/PAM) macroporous composite monolith by a green technique, using radical polymerization of acrylamide in CO_2-in-water Pickering HIPEs supported by ZnO NP. The ZnO NP acted as a metal ion source to facilitate the growth of a MOFs phase by secondary recrystallization, resulting in a MOF/PAM porous monolith. The features of the composite, particularly the photocatalytic degradation of cationic dye, were improved with higher ZnO concentration (up to 3.75 wt.%). The material demonstrated significant mechanical stress (0.24 MPa) and form recovery, with ZIF-8/PAM achieving 88.6% efficiency in dye elimination. The synthesis of porous ZIF-8/PAM composites entails a bifurcated methodology. Initially, ZnO/PAM precursors are prepared by a CO_2-in-water HIPE template process, using acrylamide (AM) as the monomer, MBA as the crosslinker, ZnO NP (2.25–5.25 wt%) as stabilizers, and PVA as a co-stabilizer (Fig. 15a). The porous ZnO/PAM complex is synthesized using free radical polymerization, exhibiting connected pores and open cellular morphologies with cavities measuring 30–125 μm and pores ranging from 2 to 20 μm. In the second stage, the ZIF-8/PAM hybridized composite is effectively produced from ZnO/PAM precursors, preserving its polyHIPE form. Nonetheless, the aggregation of ZnO NP resulted in the non-uniform dispersion of ZIF-8 crystals, restricting the availability of active sites for forming the MOF phase (Fig. 15b). The effectiveness of a catalyst in photocatalytic degradation is affected by the adsorption of pollutants and the effective species generated during the process. Their study included embedding ZIF-8 crystals into a porous organic polymer, characterized by an interconnected macroporous structure that enhances pollutant transport and maximizes interaction with ZIF-8 crystallites. This increased the availability of active sites for pollutant degradation. Research on active species indicated that hydroxyl radicals (•OH) and superoxide anions ($\bullet O_2^-$) significantly contributed to dye degradation, while holes (h^+) had little impact. A suggested model indicates that sunlight energizes electrons in ZIF-8, generating $\bullet O_2^-$ and •OH, which break down contaminants such as methylene blue (MB) (Fig. 15c). Similarly, Tian et al. [283] developed a novel monolithic MOF, monoZIF-67, with gold (Au) NPs inside. The material was designed for photocatalytic applications, particularly CO_2 photoreduction. ZIF-67 was selected because of its elevated surface area, chemical strength, minimal bandgap, and ability to capture visiblle light. Au NP was integrated owing to their localized surface plasmonic resonance (LSPR) impact, which amplifies light

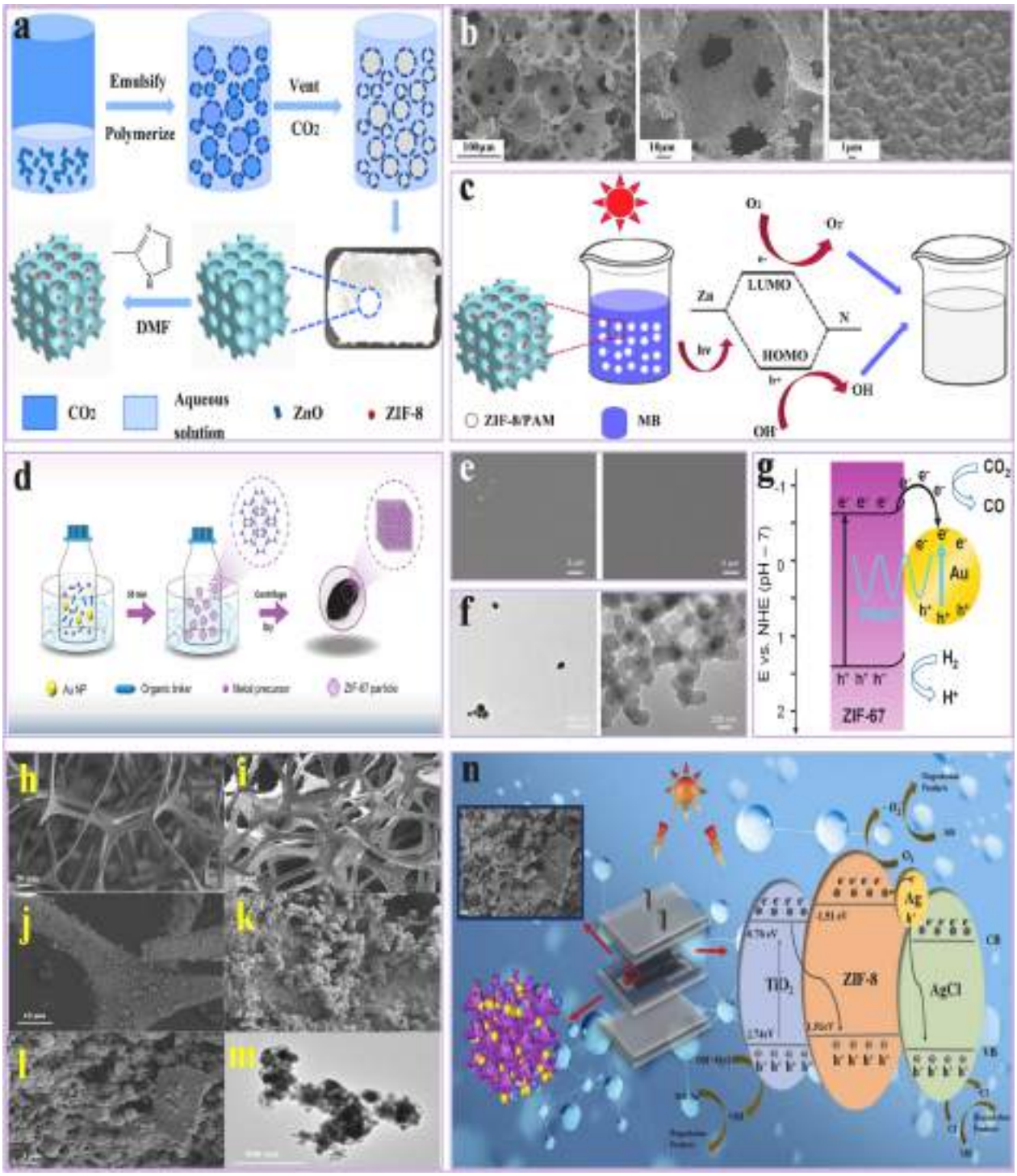

Fig. 15. (a) Synthesisc process; (b) SEM analysis of ZIF-8/PAM hybrid materials; (c) Proposed model of the photocatalytic mechanism of MB on ZIF-8/PAM, reproduced with permission from ref [282] Copyright © 2021, John Wiley and Sons. (d) Synthetic process; (e) SEM; (f) TEM analysis of monolithic Au@ZIF-67; (g) Schematic photocatalytic reaction mechanism, reproduced with permission from ref [283] Copyright © 2023, Elsevier. (h–j) SEM; (k–m) TEM analysis of MS/PDA/TiO_2/ZIF-8/AgCl/Ag; (n) The suggested route of MB photodegradation by MS/PDA/TiO_2/ZIF-8/AgCl/Ag during visible light, reproduced with permission from ref [284] Copyright © 2023, Elsevier.

absorption and promotes photocatalytic performance. The sol-gel process used in an ice bath facilitated the synthesis of monolithic ZIF-67 (monoZIF-67), which preserved its bulk design in contrast to powder ZIF-67 (powZIF-67). Both versions exhibited identical crystalline phases, as corroborated by PXRD signals. The development of monoZIF-67 was ascribed to the diminutive particle size derived from the moderate synthesis temperature (0°C), which limited crystal formation and facilitated the conversion from powder to monolith. Monolithic Au@ZIF-67 samples were produced by synthesizing polyvinylpyrrolidone (PVP)-stabilized Au NP, inhibiting Au accumulation and promoting ZIF-67 nucleation around the Au NPs. Three samples with different Au NP concentrations (1.8, 3.5, and 6 wt. %) were fabricated (Fig. 15d). The SEM and TEM analysis validated the compact, planar surface of the monoliths, with Au NP uniformly distributed and

enclosed inside the ZIF-67 structure (Fig. 15e). Some ZIF-67 particles, however, were devoid of Au cores, presumably because to the surplus of organic linkers used, which expedited nucleation but diminished Au NP integration (Fig. 15f). The higher efficiency of monolithic Au@ZIF-67 relative to pristine monoZIF-67 is ascribed to two main factors: the plasmonic impact of Au NP and better electron-hole division facilitated by the Au-ZIF-67 heterostructure. The plasmonic impact facilitates non-radiative energy transfer from Au NP to ZIF-67, generating electron-hole pairs. The diminutive dimensions of Au NP reduce scattering and the impact of hot electron insertion. Furthermore, the Au-ZIF-67 hetero-junction facilitates electron transport, hence reducing electrons-holes recombination. This integrated mechanism enhances the effectiveness of CO_2 photoreduction (Fig. 15g). Their research demonstrated that the uniformly distributed Au NP inside ZIF-67 improved CO_2 photoreduction efficiency. Under visible light, the superior monolithic Au@ZIF-67 exceeded immaculate, monolithic ZIF-67 and powdered ZIF-67 by factors of 1.5 and 3, respectively. Furthermore, Li et al. [284] engineered a 3D monolithic photocatalytic microreactor via the in-situ growth of TiO_2/ZIF-8/AgCl/Ag on polydopamine (PDA)-derived melamine sponge (MS). The MS/PDA/TiO_2/ZIF-8 was created by a lower-energy methanol solvothermal method, yielding reduced particle sizes and enhanced structural characteristics. Following hydrothermal treatment at 85°C for 24 hours, the synthesized material was washed and dried for further investigations. The structural features of the synthesized samples were analyzed using SEM and TEM. Initially, the MS has a flat surface, complicating the grafting of photocatalysts. Following polydopamine (PDA) application, the surface exhibited increased roughness, indicating effective PDA deposition (Fig. 15h–j). TiO_2 NP were evenly distributed on the PDA-doped MS surface. After ZIF-8 deposition, a compact ZIF-8 coating enveloped the TiO_2 particles. Cubic structures emerged after the incorporation of AgCl/Ag. TEM analysis validated the effective deposition of TiO_2, ZIF-8, and AgCl/Ag nanoparticles onto the MS/PDA surface (Fig. 15k–m). The photocatalytic degradation performance of the monolithic microreactor was evaluated using MB as a model contaminant. The studies were performed in a continuous recirculation flow mode under defined conditions: an input flow rate of 45 mL/min, a catalyst doping of 207 mg, and an MB amount of 15 mg/L. The MS/PDA/TiO_2/ZIF-8/AgCl/Ag microreactor exhibited superior photocatalytic performance, attaining a 99.99% elimination rate of MB in 8 minutes under visible ligh. The increased effectiveness is ascribed to the Ti-O-Zn bonds facilitating charge transfer between TiO_2 and ZIF-8, improving electrons-holes division and reaction effectiveness. TiO_2 contributes to the stability and effectiveness of Ag/AgCl. Conversely, the MS/PDA/TiO_2/ZIF-8 microreactor attained a 30.26% elimination of MB during dark adsorption, attributable to the adsorption sites offered by the PDA coating, which improves photocatalytic degradation performance (Fig. 15n).

3.12. Nanocages

The morphology of nanocages in MOFs is characterized by hollow, cage-like structures that possess thin walls and interrelated cavities [285]. This morphology provides a large surface area and increased porosity, promoting effective reactant adsorption and mass transfer [146]. The limited space within nanocages establishes a microenvironment that facilitates selective interactions between reactants and active sites, which enhances catalytic specificity [147]. Nanocages enhance light harvesting by capturing and scattering light within their hollow cavities, thus prolonging light-matter interaction [286,287]. The features cooperatively boost the separation of photoexcited charge carriers, decrease recombination rates, and enhance the overall photocatalytic performance of MOFs [288,289]. For example, Zhang et al. [290] synthesized copper NPs supported on surface-defective titanium dioxide oval nanocages (xCu/H-TiO_2) for photocatalytic CO_2RR via a solvothermal process accompanied by hydrogenation. The oval-shaped MIL-125(Ti) particles served as precursors, leading to TiO_2 nanocages with oxygen vacancies (VO) that improved visible ligh absorption and offered more active sites. The Schottky barrier established between hydrogenated TiO_2 (H-TiO_2) and Cu NP enhanced charge separation and transfer. The improved catalyst with modest Cu NP concentration demonstrated the maximum CO_2 production, selectivity, and exceptional photocatalytic stability (Fig. 16a). SEM analyses verified that the oval shape of MIL-125(Ti) was preserved in the 8Cu/H-TiO_2 sample, featuring a hollow morphology that facilitates CO_2 adsorption channels. Moderate loading of Cu NP maintained this structure; however, excessive loading resulted in aberrant morphologies (Fig. 16b). TEM analysis revealed nanosheet-assembled hollow structures containing well-distributed Cu NP, which offered increased active sites for catalytic processes (Fig. 16c). HRTEM analysis exhibited clear lattice stripes for TiO_2 and Cu, which validated the homogeneous distribution of components (Fig. 16d). The results indicate that surface fault structures and uniformly distributed Cu NP improve photocatalytic CO_2RR. Their composition and Schottky junctions affect the charge transfer effectiveness of metal/semiconductor hybrid catalysts. Steady-state PL measurements indicated that 8Cu/H-TiO_2 had the lowest peak intensity, indicating efficient suppression of electrons-holes recombination attributable to Schottky junctions and surface imperfections. EPR measurements indicated increased surface defects in 8Cu/H-TiO_2, which improved CO_2 adsorption and activation. A photoelectrochemical study revealed that 8Cu/H-TiO_2 exhibited the maximum photocurrent and the lowest charge transfer resistance, indicating rapid charge transfer. The combined impact of VO and Schottky junctions boosted photocatalytic CO_2RR effectiveness (Fig. 16e). Their research presents compelling concepts for developing MOF-based photocatalysts and prospective usages in solar-to-chemical energy transition. Similarly, Su et al. [291] devised a facile synthesis technique to prepare nickel hydroxide nanocages ($Ni(OH)_2$-NCs) using zinc-derived zeolitic imidazole structures (ZIF-8) as templates, with nickel chloride functioning as both the etching agent and metal precursor. The thickness of the nanocage wall, essential for light harvesting, may be modified by altering the salt content or the duration of the reaction (Fig. 16f). The shape of nickel hydroxide nanocages ($Ni(OH)_2$) may be precisely modified by altering the reaction duration or the Ni^{2+}/Zn^{2+} ratio verified by the STEM. Core-shell NP, designated as $Ni(OH)_2$-NP-0.4, was synthesized with a 1-hour reaction time and a Ni^{2+}/Zn^{2+} ratio of 0.4:1, featuring thin NS on the surface (Fig. 16g, h). Boosting the ratio to 2:1 yielded hollow nanocages characterized by thin, rough walls ($Ni(OH)_2$-NC-2). The nanocages, designated $Ni(OH)_2$-NC-5, exhibited larger walls and rougher surfaces with increased nanoflake thickness at a ratio of 5:1 (Fig. 16i, j). The effectiveness of charge separation and the kinetics of transfer in the system were studied by steady-state and transient fluorescence spectroscopy. The photosensitizer $[Ru(bpy)_3]^{2+}$, when stimulated at 500 nm, showed a pronounced emission peak at 607 nm, suggesting photoexcited carrier recombination. Co-catalysts significantly suppressed the emission. Ni $(OH)_2$-NC-2 showed the most pronounced quenching capability owing to its porous structure, elevated porosity, and extensive surface area, which facilitate mass transfer and particle interactions. Time-resolved PL decay investigations further corroborated the enhanced charge-transfer kinetics of $Ni(OH)_2$-NC-2, showing static charge transfer between the photosensitizer and co-catalyst. The findings underscore the improved photon usage via numerous internal reflections (Fig. 16k). Their research indicates the rational engineering and construction of inorganic hollow structures for effective photocatalysis CO_2RR. Furthermore, Verma et al. [292] fabricated an efficient photocatalytic HER using N-loaded Fe_3C (N-Fe_3C) nanocages adorned with ultrathin $ZnIn_2S_4$ NS, obtained from dual MOFs. The porous hybrid structure offers several active sites for catalytic processes and improves light absorption via scattering. This composition attained a remarkable solar-driven HER rate of 9,600 μmol $h^{-1}g^{-1}$ and an AQE of 3.6%, surpassing Pt-based co-catalysts and previously documented $ZnIn_2S_4$ nanohybrids (Fig. 16l). TEM and HRTEM analysis of the generated $ZnIn_2S_4$@N-Fe_3C nanocomposite. The results indicate that $ZnIn_2S_4$ nanostructures are

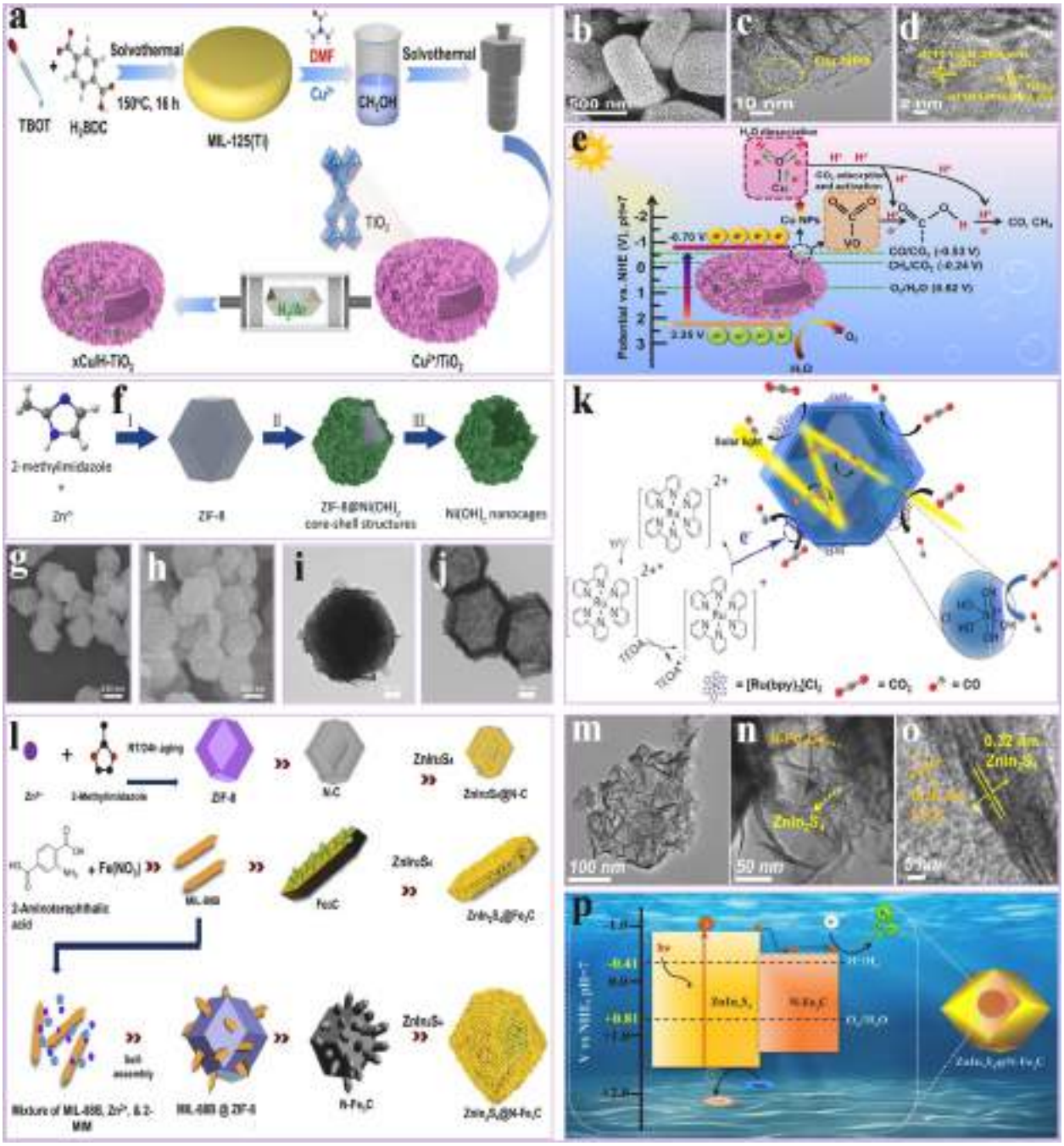

Fig. 16. (a) Synthesis process; (b) SEM; (c) TEM; (d) HRRTEM analysis of surface defective TiO_2 (xCu/H-TiO_2) oval nanocages; (e) The suggested photocatalytic CO_2RR route over 8Cu/H-TiO_2, reproduced with permission from ref [290] Copyright © 2024, Elsevier. (f) Synthesis process; (g, h) SEM; (i, j) TEM analysis of Ni$(OH)_2$-NCs; (k) Suggested route of photocatalytic CO_2RR at the oxygen vacancy sites of α-Ni$(OH)_2$, reproduced with permission from ref [291] Copyright © 2021, American Chemical Society. (l) Synthesis process; (m) TEM; (n, o) HRTEM analysis of dual MOFs and $ZnInS_4$@ N Fe_3C nanostructures; (p) Potential charge carrier reaction pathways and chemical processes for H_2 generation, reproduced with permission from ref [292] Copyright © 2023, John Wiley and Sons.

firmly adhered to the surfaces of N-Fe_3C (Fig. 16m). HRTEM analysis indicates two diffraction planes, (102) and (210), with interplanar spacings of 0.32 nm and 0.208 nm, matching to $ZnIn_2S_4$ and Fe_3C, respectively. It further validates the homogeneous dispersion of Zn, In, S, Fe, C, and N, substantiating the superior performance of the $ZnIn_2S_4$@N-Fe_3C photocatalysts (Fig. 16n, o). They investigate a photocatalytic HER using N-doped Fe_3C (N-Fe_3C) nanocages decorated with $ZnIn_2S_4$ nanoparticle NS. Sunlight energizes electron-hole pairs, facilitating the flow of electrons from $ZnIn_2S_4$ to N-Fe_3C, hence segregating charges and augmenting H_2 generation. The incorporation of N-Fe_3C reduces carrier recombination, resulting in an enhanced HER rate of 9,600 $\mu mol \cdot h^{-1} \cdot g^{-1}$ and a quantum ratio of 3.6%, exceeding that of Pt-based systems (Fig. 16p). Their research underscores the promise of noble-non-metal catalysts for solar-driven hydrogen synthesis, while improvements in quantum efficiency are necessary.

3.13. Core-shell

The core-shell morphology in MOFs features a core material surrounded by a shell of a different material, resulting in a unique layer structure [293]. This morphology improves photocatalytic efficiency through the integration of the different characteristics of the core and

shell components [154]. The core typically exhibits strong electronic or optical characteristics, whereas the shell contributes to increased surface area and active sites for catalytic processes [294]. Core-shell structures enhance charge transfer efficiency by reducing electron-hole recombination [295]. The shell serves as a protective barrier, decreasing surface defects and improving stability [156,296]. The core-shell design facilitates customized light absorption, enhanced reactant accessibility, and selective interactions. This morphology facilitates the integration of multifunctional components, which improves photocatalytic performance [155,297,298]. In this regard, Liang et al. [299] fabricated tunable iron oxide phases (Fe_3O_4 and α-Fe_2O_3) using the calcination of MIL-88A in various atmospheres and created unique 2D/1D core-shell heterojunctions ($ZnIn_2S_4$@Fe_3O_4 and $ZnIn_2S_4$@α-Fe_2O_3) by employing an in-situ self-assembly approach. The materials were evaluated for photocatalytic degradation of organic contaminants, including RhB, MB, BPA, and MO under visible ligh. The magnetic $ZnIn_2S_4$@Fe_3O_4 had the best photocatalytic performance and enhanced stability relative to $ZnIn_2S_4$, Fe_3O_4, and $ZnIn_2S_4$@α-Fe_2O_3, highlighting the influence of fluctuating weight proportions of $ZnIn_2S_4$ to iron oxide (Fig. 17a). The morphology of $ZnIn_2S_4$, α-Fe_2O_3, Fe_3O_4, and their core-shell composites (ZIS@Fe_2O_3 and ZIS@Fe_3O_4) was analyzed using SEM. Pristine $ZnIn_2S_4$ exhibited flower-shaped microspheres, while MIL-88A had a hexagonal rod-shaped morphology (Fig. 17b, c). Post-pyrolysis, α-Fe_2O_3, and Fe_3O_4 maintained their hexagonal order, although with diminished dimensions. $ZnIn_2S_4$ was effectively deposited onto the surfaces of α-Fe_2O_3 and Fe_3O_4, resulting in a distinct 2D/1D core-shell structure. TEM analysis revealed a $ZnIn_2S_4$ shell and α-Fe_2O_3 or Fe_3O_4 core (Fig. 17d, e). The photocatalytic performance of $ZnIn_2S_4$, Fe_3O_4, α-Fe_2O_3, and their composites (ZIS@Fe_3O_4 and ZIS@Fe_2O_3) was assessed by the degradation of organic pollutants (RhB, MB, BPA, MO) under visible ligh. ZIS@Fe_2O_3-5 exhibited a degradation performance of 96.4% for RhB over 180 minutes, but ZIS@Fe_3O_4-5 surpassed this, with

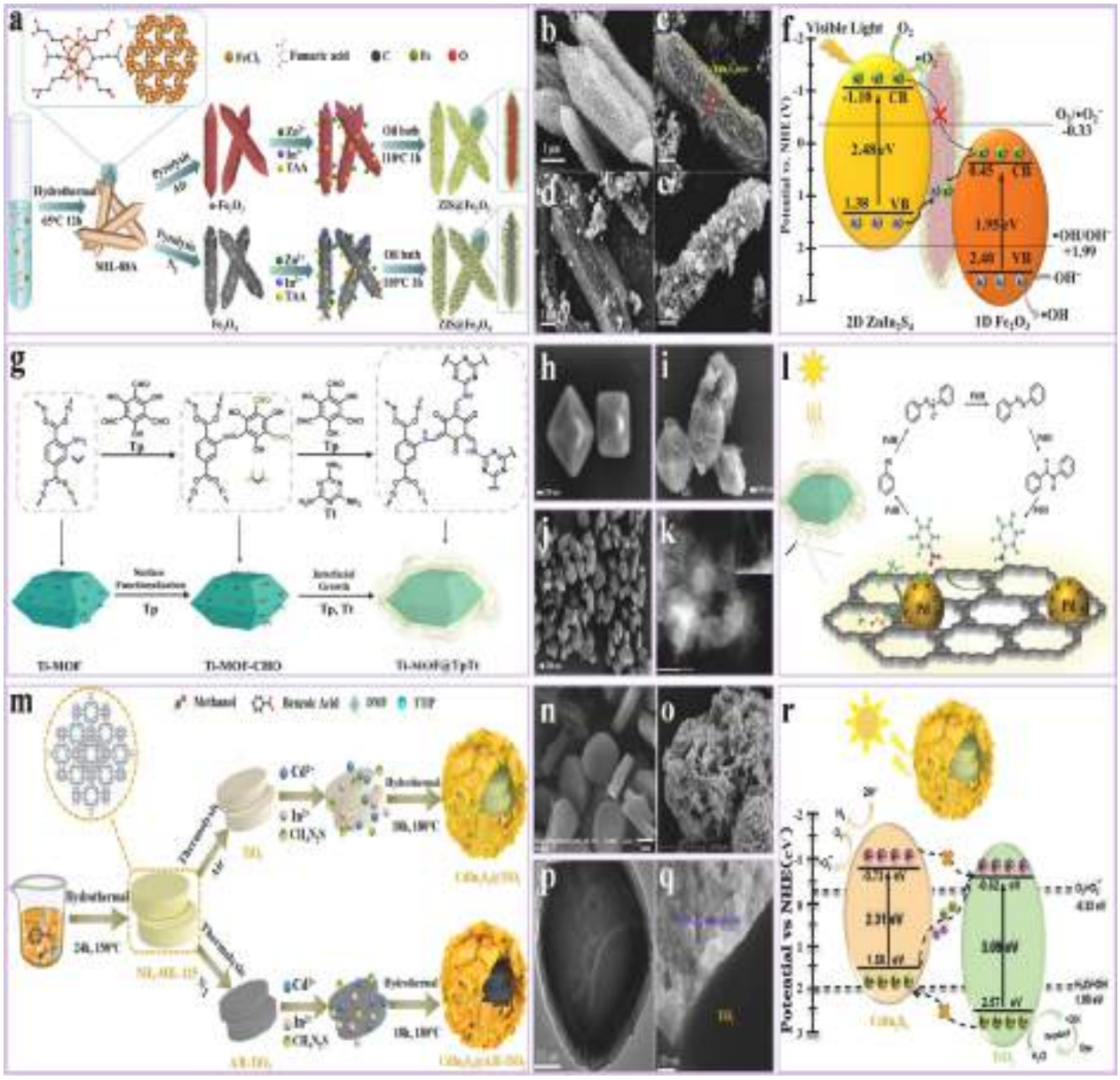

Fig. 17. (a) Synthesis process; (b, c) SEM; (d, e) TEM analysis of ZIS@Fe_2O_3 and ZIS@Fe_3O_4; (f) Suggested charge separation and transition routes of ZIS@Fe_2O_3 and ZIS@Fe_3O_4, reproduced with permission from ref [299] Copyright © 2020, Elsevier. (g) Synthesis process; (h–k) SEM analysis of Pd decorated Ti-MOF@TpTt hybrids; (l) The route of nitrobenzene hydrogenation during visible light over Pd@2, reproduced with permission from ref [155] Copyright © 2021, John Wiley and Sons. (m) Synthesis process; (n, o) SEM; (p, q) TEM analysis of CIS@ TiO_2-0.8 and CIS@ A/R-TiO_2-1.2; (r) Suggested charge separation and transition routes of CIS@ TiO_2-0.8 and CIS@ A/R-TiO_2-1.2, reproduced with permission from ref [300] Copyright © 2021, Elsevier.

96.7% degradation in 60 minutes. ZIS@Fe_3O_4-5 showed enhanced degradation efficiency for MB, BPA, and MO relative to ZIS@Fe_2O_3-5. Both composites exhibited exceptional stability and reusability, preserving photocatalytic efficiency after several cycles, making them advantageous for environmental cleanup (Fig. 17f). Their research presents an innovative approach to developing magnetic photocatalysts for wastewater treatment. Similarly, Zhang et al. [155] produced a Ti-MOF@TpTt hybrid treated with an ultra-thin COF nanobelt by a sequential growth approach. The Pd-doped Ti-MOF@TpTt catalyst showed considerable superior photocatalytic efficiency relative to Ti-MOF, TpTt-COF, and Ti-MOF@TpTt hybrids with a fibrillar-like COF shell. The improved effectiveness in photocatalytic processes, including ammonia borane hydrolysis and nitroarene hydrogenation, is attributed to the elevated BET surface area of catalysts, core-shell configuration, and type II heterojunction, which boost active sites mobility and carrier separation effectiveness (Fig. 17g). SEM analysis reveals that the Ti-MOF exhibits a truncated bipyramidal octahedral shape characterized by smooth surfaces. Following functionalization with Tp aldehyde via a Schiff base reaction, the Ti-MOF-CHO preserves its crystalline structure and shape. The existence of aldehyde groups is validated by FTIR, exhibiting a distinctive C═O stretching vibration at 1700 cm^{-1}. The aldehyde groups promote the development of TpTt-COF, leading to the effective synthesis of Ti-MOF@TpTt hybrids. SEM analysis demonstrate that the hybrids preserve the original Ti-MOF design, with TpTt-COF developing an ultra-thin nanobelt shell layer on the outside (Fig. 17h−k). The catalytic effectiveness of Pd@2 was assessed for one-pot cascade process, including ammonia borane hydrolysis and nitrobenzene hydrogenation at 298 K. Pd@2 demonstrated exceptional catalytic effectiveness, attaining full transformation with over 99% selectivity in 10 minutes under visible ligh in aqueous conditions. The absence of hydrogenation without AB underscores the significance of hydrogen derived via AB hydrolysis. The conversion rate decreased in the absence of light owing to less HER. Methanol inhibited the process, corroborating the essential role of active hydrogen from AB hydrolysis. Substituting AB with gaseous H_2 yielded just a 5% conversion, demonstrating that AB hydrolysis is more efficacious. Pd NP were identified as vital active sites, with no Pd leaching seen post-reaction (Fig. 17l). Their research presents a method to regulate COFs shell shape in MOF@COF composites, emphasizing its significance in improving photocatalytic performance and broadening potential applications in photocatalysis. Furthermore, Zhao et al. [300] synthesized 2D titanium oxide with a tunable phase utilizing NH_2-MIL-125 (Ti) as a template, yielding TiO_2 and A/R-TiO_2 by pyrolysis in varying atmospheres. Using in-situ self-assembly, they synthesized 2D/3D core-shell heterojunctions ($CdIn_2S_4$@TiO_2 and $CdIn_2S_4$@A/R-TiO_2). The 3D $CdIn_2S_4$ shell evenly enveloped the 2D TiO_2 core, with $CdIn_2S_4$@A/R-TiO_2 exhibiting a superior BET surface area of 106.54 m^2/g, boosting contact areas and active sites. $CdIn_2S_4$@A/R-TiO_2-1.2 exhibited enhanced photocatalytic degradation and HER to $CdIn_2S_4$@TiO_2-0.8 (Fig. 17m). SEM analysis revealed NH_2-MIL-125 as disk-shaped (~4.5 μm) and $CdIn_2S_4$ as flower-like microspheres (~4 μm). The pyrolyzed TiO_2 derived from NH_2-MIL-125 is diminutive and rectangular (Fig. 17n, o). $CdIn_2S_4$ synthesized on A/R-TiO_2 has a core-shell morphology characterized by a flower-like shell around a discernible A/R-TiO_2 core. TEM validates the core-shell structure and the existence of TiO_2 and $CdIn_2S_4$ phases (Fig. 17p, q). The photocatalytic HER experiments indicate that pure TiO_2 and A/R-TiO_2 produce little hydrogen due to inadequate response to visible ligh. Pure $CdIn_2S_4$ has a decreased HER rate (841.86 μmol g^{-1}) attributable to significant charge recombination. Among the composites, CIS@A/R-TiO_2-1.2 had the maximum HER (4306.86 μmol g^{-1}) in 3 hours, almost 5.1 times more than pristine $CdIn_2S_4$. The ideal CIS@TiO_2-0.8 exhibited an improved HER rate (3003.3 μmol g^{-1}). Excessive $CdIn_2S_4$ might decrease the production rate owing to its shielding impact. The optimal rates for CIS@A/R-TiO_2-1.2 and CIS@TiO_2-0.8 were 1435.62 and 1001.1 μmol $g^{-1}h^{-1}$, respectively. NH_2-MIL-125(Ti)@$CdIn_2S_4$-40 generated 868 μmol $g^{-1}h^{-1}$, inferior to the optimized CIS composites (Fig. 17r).

3.14. Yolk–shell

Yolk–shell morphology in MOFs is a special kind of structure in which a hollow or porous shell surrounds a core (yolk), leaving a gap between them [158]. This design improves photocatalytic efficiency through the integration of large surface area, structural stability, and effective mass transfer [160]. The yolk offers active sites for photocatalytic processes and enhances light absorption, whereas the hollow shell aids in the diffusion of reactants and products, thus decreasing transport resistance [159]. The void space diminishes electron-hole recombination by functioning as a charge-separation interface, thus enhancing the productivity of photoexcited charge carriers [301,302]. The shell additionally protects the core from structural degradation, improving stability in operational conditions [303–305]. In this regard, Zhou et al. [306] investigated the influence of the spatial arrangement of Pt NPs inside Ni/Zn-MOF on catalytic effectiveness, employing cinnamaldehyde (CAL) as a model substrate. Various catalysts were synthesized by manipulating the positioning of metal MNPs inside or on the MOFs throughout its development. The catalysts were classified based on the positioning of the metal nanoparticles (MNPs): inside the core (MNPs@MOF(S)), on the surface (MNPs/MOF(S)), inside the yolk-shell core (MNPsin@MOF(Y)), or within the interstitial space between the shell and core (MNPsvoid@MOF(Y)). Among the catalysts evaluated, Ptvoid@MOF(Y) exhibited the highest catalytic efficiency, achieving 98.2% selectivity for cinnamyl alcohol along with an impressive conversion rate of 97% (Fig. 18a). The structural characteristics of Pt/MOF material were examined using SEM and TEM. Smooth Ni/Zn-MOF(S) microspheres were generated after 1.5 hours of crystallization. Pt NP was then added to the mixture for a further 4.5 hours, yielding Ptvoid@MOF(Y) with an echinoidea-shaped morphology and a size of around 3 mm (Fig. 18b). The addition of Pt NP did not modify the original structure of Ni/Zn-MOF, as shown by comparable structural findings in pure Ni/Zn-MOF and PXRD data (Fig. 18c). The catalytic process of Ptvoid@MOF(Y) was investigated using hydrogen temperature-programmed desorption (H_2-TPD), revealing that Ptvoid@MOF(Y) exhibited the lowest desorption temperature (348°C), signifying enhanced HER activity and superior cinnamaldehyde (CAL) conversion. Findings indicated electronic interactions between Pt and Ni/Zn-MOF, shown by a positive change in Pt binding energies and a negative shift in $Ni_2p_{3/2}$, implying electron transfer. It further evidence validated electron transport from Pt NP to the Ni/Zn-MOF, hence boosting the performance of catalysts (Fig. 18d). Their research introduces an innovative method for improving the spatial arrangement of MNPs inside MOFs supports to improve catalytic effectiveness, providing a technique applicable to the design of additional embedded or supported metal NP catalysts. Similarly, Lv et al. [307] synthesized diverse Ni@carbon composites with Ni-MOF as a precursor, which preserved essential characteristics like a substantial surface area, porous structure, yolk-shell morphology, and elevated Ni content. The Ni@carbon materials were evaluated for their catalytic efficiency in reducing Cr(VI) with HCOOH as the reducing agent. The samples, pyrolyzed at varying temperatures, had a consistent spherical morphology (~2 μm), with Ni@carbon550 revealing a hollow, fragmented chamber on its smooth exterior (Fig. 18e). TEM analysis of Ni@carbon450 exhibited a yolk-shell morphology characterized by a shell thickness of around 300 nm and an inner yolk diameter of around 700 nm (Fig. 18f, g). HRTEM analysis displays five diffraction rings associated with Ni crystalline planes (111, 200, 220, 311, 420), with the lowest ring matching the (002) plane of graphene (Fig. 18h). Distinct lattice fringes in the HRTEM analysis reveal interplanar lengths of 0.34 nm for the (002) planes of graphene and 0.2 nm for the (111) planes of nickel (Fig. 18i). The suggested catalytic mechanism for Cr(VI) reduction with Ni@carbon450 entails HCOOH and Cr(VI) adsorption onto the surface of catalysts via electrostatic interaction. Cr(VI) readily permeates the

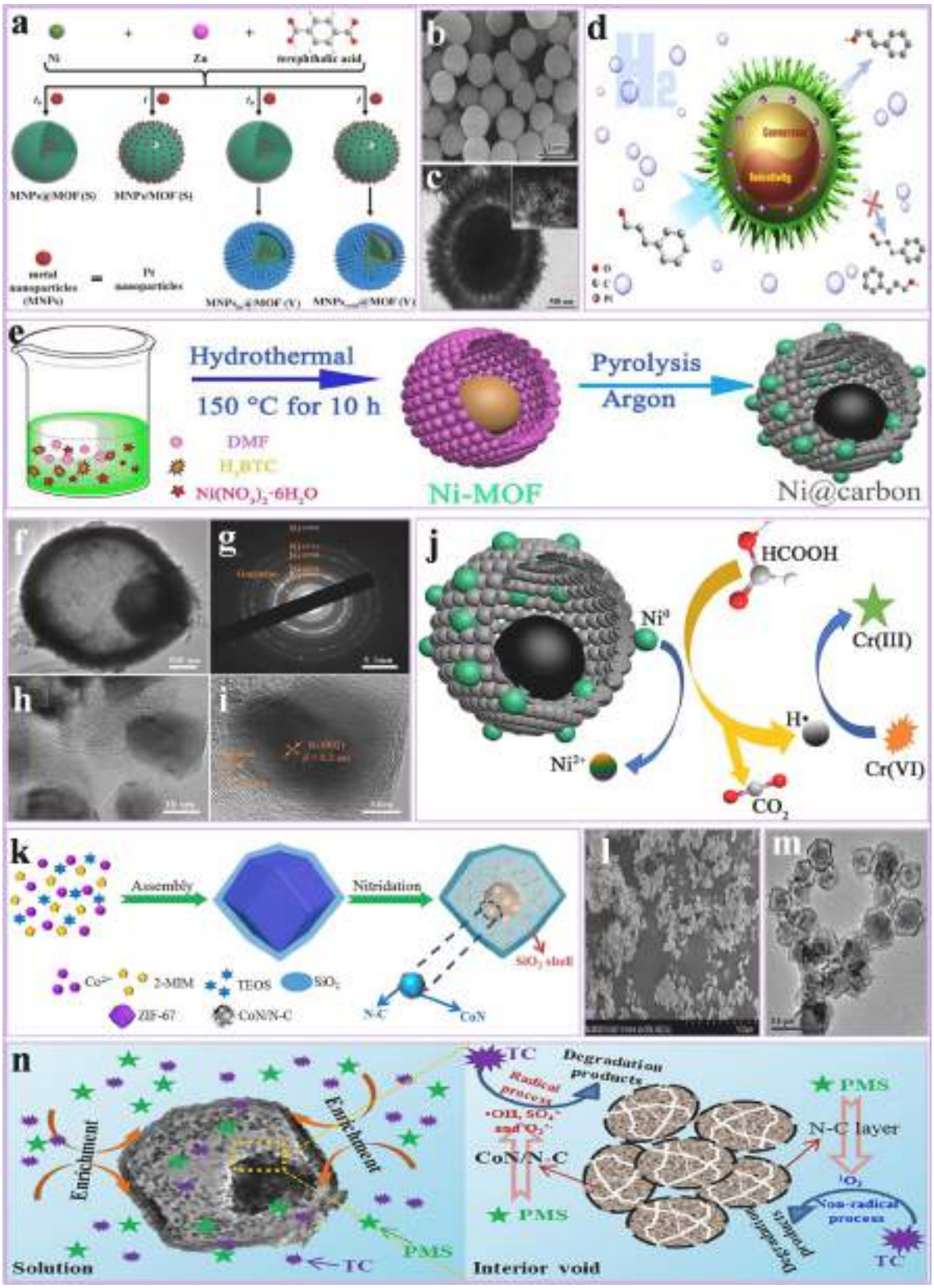

Fig. 18. (a) Synthesis process; (b) SEM; (c) TEM analysis of MNPs in Ni/Zn-MOF microspheres; (d) Proposed catalytic mechanism of Ptvoid@MOF(Y), reproduced with permission from ref [306] Copyright © 2019, John Wiley and Sons. (e) Synthesis process; (f, g) TEM; (h, i) HRTEM analysis of 3D yolk shell-like structure Ni@carbon; (j) Reduction process of Cr(VI) in Ni@carbon450 inside the HCOOH system, reproduced with permission from ref [307] Copyright © 2020, Elsevier. (k) Synthesis process; (l, m) TEM of yolk-shell CoN/N-C@SiO_2 nanoreactor; (n) Suggested route for TC degradation by CoN/N-C@SiO_2-500 + PMS systems, reproduced with permission from ref [308] Copyright © 2020, Elsevier.

material, enhancing its interaction with active sites. HCOOH undergoes dehydrogenation, yielding CO_2 and hydrogen (H•), which deposit on the surface of catalysts. Nickel facilitates the production of hydrogen radicals and is oxidized from Ni(0) to Ni(II). The hydrogen atoms facilitate the reduction of Cr(VI) to Cr(III) by electron transfer. Catalytic performance improves with elevated HCOOH concentration since more HCOOH molecules promote HER, aiding Cr(VI) reduction (Fig. 18j). Their research demonstrates that the fast synthesis, robust catalytic activity, and effective regeneration provide Ni@carbon450 a viable catalyst for the remediation of Cr(VI)-contaminated wastewater or groundwater, providing novel insights for the formation of non-precious metal catalysts. Furthermore, Zhang et al. [308] effectively fabricated a new yolk-shelled nanoreactor (CoN/N-C@SiO_2) with dual active sites using the nitridation of MOF@SiO_2. The catalyst, analyzed via several approaches, was evaluated as a PMS activator for removing TC. They assessed the impact of catalyst dose, PMS and TC concentrations, reactivity temperature, pH, and foreign ions on TC degradation. The catalytic efficiency was evaluated on additional dye and phenolic pollutants, thoroughly examining the degradation route and PMS activation process (Fig. 18k). TEM analysis demonstrated that the MOF@SiO_2 precursor (200–500 nm) preserved the octahedral morphology of ZIF-67, including a rough SiO_2 shell measuring 20 nm in thickness. Post-nitridation, the CoN/N-C@SiO_2-500 structure sustained its shape, exhibiting well-dispersed octahedrons with some fragmented particles, indicating a hollow architecture (Fig. 18l). TEM analysis further revealed that the CoN yolks, measuring 50–70 nm, were crystalline and encased by SiO_2 shells around 30 nm thick. Minute particles (5–10 nm) were detected inside the interstitial voids (Fig. 18m). The catalytic effectiveness of CoN/N-C@SiO_2 in PMS activation was evaluated using TC degradation. PMS alone showed vanity, with just 18.7% total carbon (TC) removal in 30 minutes, whereas CoN/N-C@SiO_2-500 had a negligible effect, with only 3.6% removal by static adsorption. Among several catalysts, CoN/N-C@SiO_2-500 had the greatest TC removal rate of 98.6% after 15 minutes, owing to its excellent nitridation temperature and yolk-shell morphology. Co_3O_4@SiO_2-500 and Co_3O_4/N-C@SiO_2-500 attained 67.2% and 89.4% total carbon removal, respectively. The efficiency of CoN/N-C@SiO_2-500 exceeds that of these catalysts, indicating that cobalt nitride provides enhanced catalytic activity for PMS stimulation (Fig. 18n). Their research presents a viable method for developing multifunctional yolk-shell nanojunction with enhanced structure and composition for environmental cleanup.

3.15. Aerogel

Aerogel morphology in MOFs represents a highly porous and ultralight structure characterized by a network of interrelated nanoscale structures [309]. This morphology features a high surface area, lower density, and significant porosity, rendering it suitable for improved photocatalytic processes [162]. The porous structure enhances light penetration and extends light-matter interactions, resulting in improved photocatalytic performance [310]. Aerogels offer a significant number of active sites for catalytic reactions, attributed to their elevated surface-to-volume ratio. Their interconnected structure enhances charge transfer and minimizes electron-hole recombination [311,312]. The lightweight and flexible characteristics of aerogels facilitate their integration into devices, rendering them versatile and practical for scalable applications [313]. In this regard, He et al. [314] fabricated a 3D porous g-C_3N_4/NH_2-MIL-53(Fe) aerogel via the electrostatic self-assembling of negatively charge g-C_3N_4 NS and positively charged NH_2-MIL-53(Fe) in an aqueous medium. The photocatalytic and recycling efficiency of the aerogel was evaluated by decomposing organic contaminants using visible ligh. The cooperative electron transport among the components improved carrier separation, leading to superior photocatalytic activity (Fig. 19a). The structural features of the generated samples were examined using SEM and TEM techniques. The SEM analysis indicated that the CN had a rough lamellar structure, while the TEM showed a 2D sheet-shaped nanostructure with a porous surface (Fig. 19b–d). NH_2-MIL-53(Fe) exhibited an angular, spindle-like microstructure with an average dimension of around 800 nm. The CNMIL-2 sample demonstrated NH_2-MIL-53(Fe) firmly attached to the CN surface, improving the CN shape and elevating its surface area to 99.4 m^2/g, in contrast to 77.2 m^2/g for pure CN (Fig. 19e–g). The mechanism of photodegradation comprises many stages. Visible ligh induces the formation of electron-hole pairs in both g-C_3N_4 and NH_2-MIL-53(Fe). The elevated CB level of g-C_3N_4 (−0.6 eV) relative to NH_2-MIL-53(Fe) (0.81 eV) facilitates the transport of electrons from g-C_3N_4 to NH_2-MIL-53(Fe). Simultaneously, holes from NH_2-MIL-53(Fe) migrate to g-C_3N_4, boosting the quantity of free holes in g-C_3N_4, so facilitating the division of photoexcited electrons and holes. The pores in g-C_3N_4 oxidize organic contaminants directly. Furthermore, Fe^{2+} generated by the reduction of Fe^{3+} on NH_2-MIL-53(Fe) interacts with H_2O to provide •OH radicals, further facilitating pollutant degradation. This method reduces electrons-holes recombination and promotes fast charge transfer and separation (Fig. 19h). Their research highlights novel insights into the usage of MOFs in g-C_3N_4-based aerogel photocatalysts for the remediation of organic contaminants in water usage. Similarly, Song et al. [315] synthesized photocatalytic aerogels by integrating MOF-808 with graphene, using its elevated surface area, stability, and facile production process. The aerogel demonstrated superior performance in converting CO_2 to CO and CH_4 relative to pristine MOF-808 and powder materials. The aerogel structure improved thermal conductivity, electron transport, visible ligh absorption, and photocatalytic efficiency (Fig. 19i). TEM and SEM were employed to analyze the structure of photocatalysts, surface morphological characteristics, and elemental content. MOF-808 exhibited a uniform octahedral morphology with a diameter of about 500 nm, while RGO displayed a porous, ultrathin lamellar morphology characterized by random folds (Fig. 19j–l). The conversion of GO to RGO was validated by enhanced surface roughness and irregularities. MOF-808 was consistently distributed inside the RGO lamellae, inhibiting RGO flake aggregation and producing bulkier, more voluminous macroscopic aerogels. The microscopic structure of the MR-5 powdery photocatalyst resembled that of M/R-5 (Fig. 19m–o). The photocatalytic CO_2RR process of MOF-808/RGO under sunshine demonstrates that sunlight excites electrons in MOF-808, which RGO captures, enhancing carrier separation. Adsorbed CO_2 interacts with electrons and protons derived from water vapor, forming CO and minor quantities of CH_4. The macroscopic aerogel exhibits enhanced catalytic efficiency attributable to the synergistic impacts of reduced graphene oxide (rGO) and its structural attributes, which optimize light usage and augment both photothermal and photovoltaic efficiencies (Fig. 19p). Their research underscores the significance of the aerogel structure in enhancing CO_2RR and presents a novel viewpoint on the use of MOF-based aerogels for photocatalysis. Furthermore, Yu et al. [84] devised a microwave-induced method to synthesize MXene/MOF conductive aerogel photocatalysts for effective acetone photodegradation under humid conditions. Ti_3C_2 MXene, recognized for its superior electron uptake and transport properties, was used to facilitate the formation of MOFs. Through the incorporation of 2-methylimidazole into the MXene surface and microwave-induced production, they attained substantial MOF loading (~80 wt.%) and efficient N-metal bridging. This method optimized the surface area and active sites of MOF while using the light-harvesting properties of MXene. The aerogels were analyzed to evaluate their shape, surface, and diverse characteristics (Fig. 19q). SEM analysis demonstrates that ultra-thin Ti_3C_2 NS (Ti_3C_2 NS) were effectively synthesized from Ti_3AlC_2 powders, exhibiting a consistent 2–3 nm thickness. The integration of modified Ti_3C_2 NS (Ti_3C_2 NS-m) into the aerogel raised pore size, hence improving the accessibility of catalytic sites and facilitating mass transfer. For MPA/U66N, little U66N proliferation occurred on Ti_3C_2 NS, indicating inadequate expansion. In the MPA-m/U66N-H composite, an increased quantity of U66N particles, about 200 nm in size, was noted as a result of the altered surface. The MPA-m/U66N-M composite exhibited extensive coverage of diminutive U66N

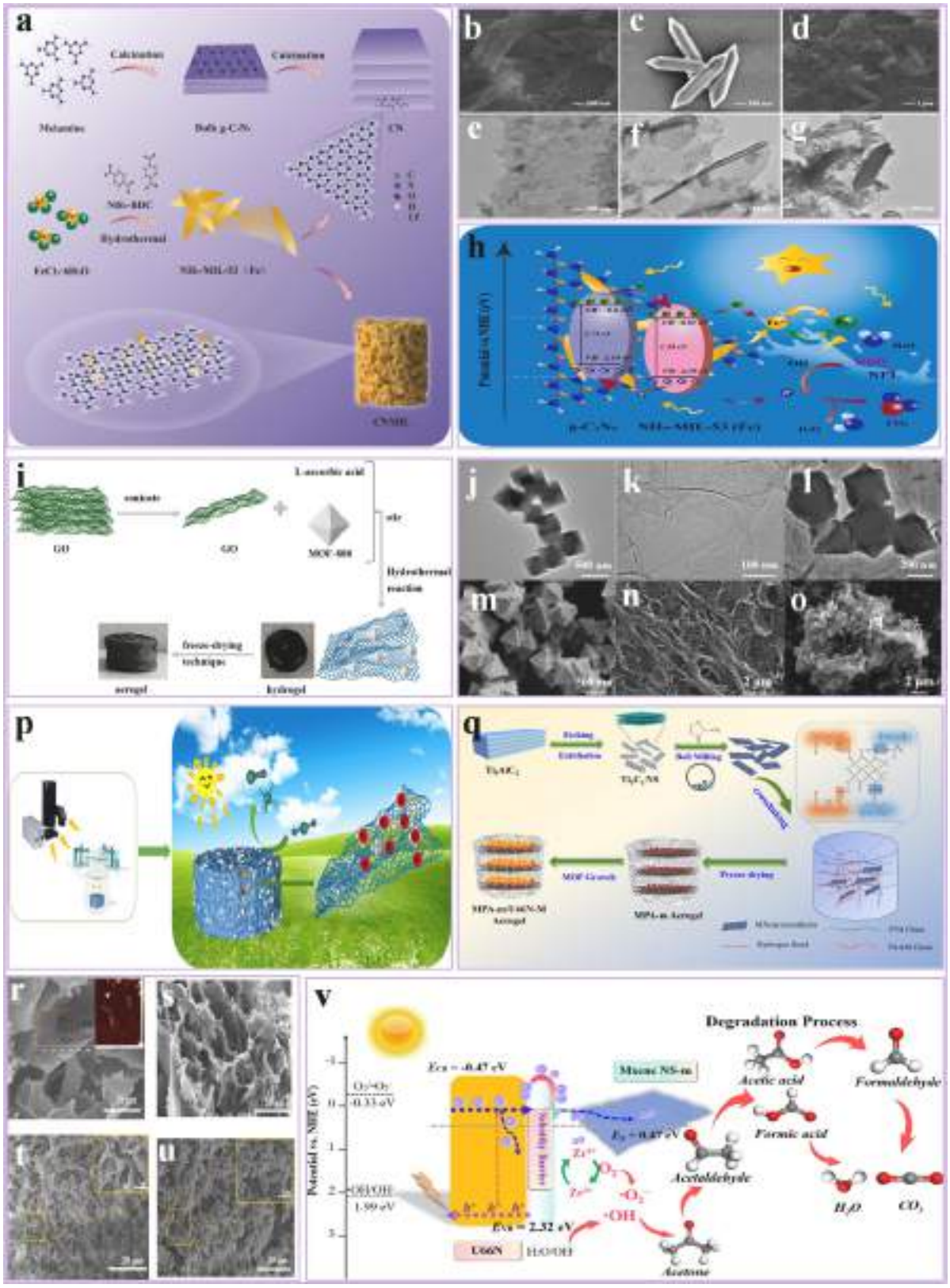

Fig. 19. (a) Synthesis process; (b–d) SEM; (e–g) TEM analysis of 3D porous g-C_3N_4/ NH_2-MIL-53(Fe) aerogel; (h) Schematic representation of the suggested photocatalytic degradation pathway for CNMIL composites, reproduced with permission from ref [314] Copyright © 2023, Elsevier. (i) Synthesis process; (j–l) TEM; (m–o) SEM analysis of M/R-5; (p) Proposed photocatalytic CO_2RR process on MOF–808/RGO macroscopic aerogel, reproduced with permission from ref [315] Copyright © 2024, Elsevier. (q) Synthesis process; (r–u) SEM analysis of MPA-m/U66N-M; (v) A hypothesized process for acetone photodegradation on MPA-m/U66N-M, reproduced with permission from ref [84] Copyright © 2023, Elsevier.

particles (~120 nm) as a result of microwave irradiation, which, owing to the robust microwave absorption of Ti_3C_2 NS, generated localized hot spots that enhanced N-Zr coordination and expedited U66N crystallinity (Fig. 19r–u). The suggested process for acetone photodegradation initiates in visible light, whereby photoelectrons are generated in U66N-M and then transported to MPA-m via the MI bridge, propelled by the disparity in work function. This establishes a Schottky barrier at the U66N-MPA-m contact, enhancing electrons-holes separation. Photoexcited holes in U66N decompose acetone contaminants, while photoelectrons interact with O_2 to prepare superoxide radicals ($\bullet O_2^-$). Adsorbed water is transformed into hydroxyl radicals (•OH), hence accelerating deterioration. In humid conditions, the rivalry for water and acetone adsorption diminishes, resulting in the oxidation of acetone into CO_2 and H_2O via radicals and holes (Fig. 19v). Their research indicates that the newly engineered MPA-m/U66N-M has potential as a material for the photodegradation of VOCs in future practical applications.

3.16. Nanoflowers

Nanoflower morphologies in MOFs boost photocatalytic applications by providing a substantial surface area and enhanced light absorption, attributable to their petal-like 3D structure. This morphology amplifies the quantity of active sites and improves the absorption and scattering of light, which is essential for effective photocatalysis [316]. The hierarchical and porous structure enhances charge separation, reduces electrons-holes recombination, and increases total photocatalytic performance. The linked structure of the nanoflower structure enhances the rapid mass transfer of reactants and products, hence expediting reaction kinetics [317]. Furthermore, the adequately exposed surfaces of nanoflower MOFs provide enhanced integration with other functional materials, generating synergistic impacts that further augment catalytic efficiency for energy and environmental applications [318,319]. In this regard, Li et al. [320] synthesized an innovative MOF-based Cu_2O/Cu/PDA/CF catalyst to effectively eliminate pollutants from environmental water. The catalyst comprises a nanoporous Cu_2O/Cu system obtained from a 2D nanoflower MOFs membrane and a polydopamine (PDA)-enhanced copper foam scaffold. The elevated aspect ratio of the nanoflower MOFs reveals several Cu^{2+} sites, facilitating the generation of well-dispersed NP. The PDA coating improves the distribution and stability of the catalyst. The as-synthesized materials showing performance in converting 4-nitrophenol (4-NP) to 4-aminophenol (4-AP) was methodically investigated, creating a continuous flow CFCR-HPLC system for real-time observation (Fig. 20a). The structural features of Cu foam, PDA/CF, NH_2-CuBDC/PDA/CF, and Cu_2O/Cu/PDA/CF were examined using SEM and TEM techniques. The conventional Cu foam had a smooth 3D network structure, but the PDA coating produced a textured surface characterized by leaf-like NS (Fig. 20b). Following the continued development of NH_2-CuBDC,2D NS arrays with a 5–10 μm thickness evenly enveloped the surface (Fig. 20c). Following in situ reduction, a 3D mesh structure was established, including NP having a median size of 13.5 nm. HRTEM validated the existence of Cu_2O and Cu nanocomposites, whereas BET analysis indicated a surface area of 5.0274 m^2/g and a pore diameter of 8.6725 nm (Fig. 19d). A suggested catalytic reaction mechanism has four stages: Cu(II) in the MOF precursor is decreased to Cu(I)-H by $NaBH_4$, forming active sites. 4-NP molecules adsorb onto the catalyst by π-π connection and hydrogen bonding. The 4-NP undergoes successive hydrogenation at Cu(I)-H sites, yielding 4-AP and H_2O. The catalyst reconstitutes Cu(I) for further cycles, whereas Cu(0) also facilitates the reduction of 4-NP. In addition, stability studies indicated that in a flow-through mode, the Cu_2O/Cu/PDA/CF catalyst sustained over 95% degrading efficiency of 4-NP for more than 300 minutes, markedly surpassing non-PDA-modified variants owing to the functionality of PDA in stabilizing metal nanoparticles (Fig. 20e). Their research provides significant insights into the creation of effective catalysts for wastewater treatment. Similarly, Zhang et al. [168] created innovative flower-like hierarchical nanostructures using a bifunctional Ru-MOF, which operate as efficient heterogeneous photocatalysts for visible ligh-induced CO_2 photoreduction. The distinctive nanoflower structure improved photocatalytic efficiency by 150% relative to solid microcrystals. The 3D structure enhanced the stability and recyclability of the Ru-MOF NS, hence enhancing photocatalytic rate (Fig. 20f). The structural features of the Ru-MOF nanoflowers were examined using SEM and TEM, demonstrating monodisperse structures with diameters ranging from 10 to 20 μm. The high-magnification SEM analysis reveals that these nanoflowers consist of tightly interwoven 2D NS, each measuring hundreds of nanometers in width and 50–70 nm in thickness (Fig. 20g–j). The NS radiates from the core, creating a hierarchically branch structure that minimizes surface energy and improves stability. TEM scans corroborate these characteristics, reinforcing SEM research's stability and intricate structure (Fig. 20k, l). The exceptional photocatalytic efficiency of Ru-MOF nanoflowers is ascribed to their distinctive shape. In a comparison of photocatalysts of varying sizes bulk crystals, micro-flakes, and nanoflowers, the nanoflowers exhibited superior CO_2RR productivity, with a catalytic rate of 77.2 mmol/g per hour and a quantum yielding of 0.67%. The improved performance results from two primary advantages: an expanded surface area that enhances active sites, facilitates reactant interaction, and increases productivity in excited-state energy transfer, enabling more excitons to arrive at reaction sites before quenching. These attributes significantly enhance the total photocatalytic performance (Fig. 20m). Their research presents a viable method to improve MOF-derived photocatalysts for CO_2RR. Furthermore, Zhao et al. [321] used an aliovalent-substitution approach to incorporate Co(II/III) into Ce-O clusters inside MOF precursors. This changed the cluster structure, affected crystallization, enhanced surface area, and controlled shape. Incorporating Co(II/III) also increased pore size to enhance mass transfer and boosted active sites for sulfate radical ($SO_4^{\bullet -}$) generation. Consequently, CeO_2•Co_3O_4 nanoflowers attained a 99% clearance rate of norfloxacin in 20 minutes and showed extensive efficiency against several antibiotics and organic contaminants (Fig. 20n). SEM analysis indicated the formation of solid spindle-like nanorods by the coordination of Ce-O clusters with TCPP ligands. The morphology was altered with different Ce/Co ratios. Nanoflowers exhibiting counterclockwise-rotating nanoscale petals (about 10 μm in diameter) were seen at a 1:1 ratio (Fig. 20o–r). TEM analysis indicated that these nanoflowers had inadequate light transmission. As the Ce/Co ratio rose to 1:2, the morphology transitioned to randomly stacked ultrathin NS exhibiting enhanced light transmission. Conversely, Co-TCPP formed quadrangular bevels of irregular dimensions (Fig. 20s–v). Their research suggests a coordination-assembly-calcination method for catalyst fabrication. TCPP molecules coupled with Ce-O clusters create Ce-TCPP nanorods, whereas the introduction of Co(II) results in a morphological transition from nanorods to nanoflowers and, subsequently, to NS. The inclusion of Co(II) affected the crystal structure and morphology, increasing porosity and creating oxygen vacancies. Post-calcination, the CeO_2•Co_3O_4 nanoflowers exhibited superior effectiveness in degrading antibiotics and organic contaminants. Significantly, 99.5% of AMX was decomposed after 50 minutes, while prevalent contaminants such as RhB, MO, and AO were eliminated within 5 minutes. The sample demonstrated extensive pollution removal performance (Fig. 20w). Their research proposes a method to augment MOF-based catalysts by including heterometals with diverse valence states and coordination numbers, enhancing mass transfer efficiency.

3.17. Nanoribbon

Nanoribbon catalysts employed in MOFs improve photocatalytic efficiency due to their distinctive shape and characteristics. Their 2D structure offers an extensive surface area and more active sites, enhancing catalytic processes [322]. The elongated configuration of nanoribbons enhances effective charge separation and transport, hence

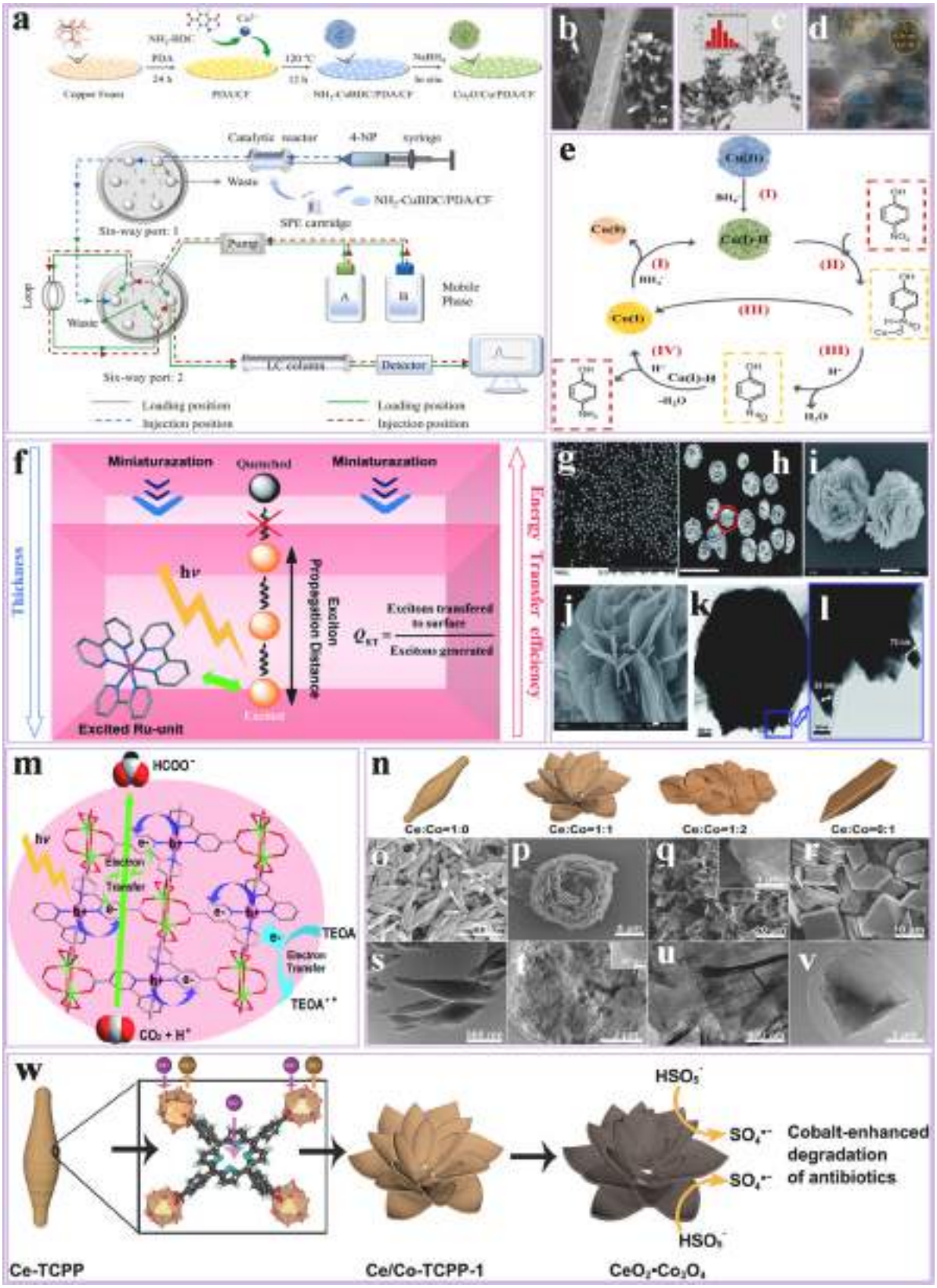

Fig. 20. (a) Synthetic process; (b) SEM; (c) TEM; (d) HRTEM analysis of Cu_2O/Cu/PDA/CF; (e) A potential catalytic reaction pathway for 4-NP to 4-AP involves NH_2-CuBDC/PDA/CF and excess $NaBH_4$, reproduced with permission from ref [320] Copyright © 2023, Elsevier. (f) Schematic representation of the intracrystalline excited-state energy transfer in the Ru-MOF; (g–j) SEM; (k, l) TEM analysis of Ru-MOF at different magnifications; (m) A depiction of the preliminarily suggested photocatalytic pathway for the conversion of CO_2 to HCOO by the Ru-MOF, reproduced with permission from ref [168] Copyright © 2015, Royal Society of Chemistry. (n) Synthetic process; (o–r) SEM; (s–v) TEM of CeO_2•Co_3O_4 nanoflowers; (w) Schematic representation of the design method for CeO_2•Co_3O_4 nanoflowers and the accelerated degradation mechanism, reproduced with permission from ref [321] Copyright © 2021, John Wiley and Sons.

reducing electron-hole recombination. When integrated with MOFs, they form synergistic heterostructures in which MOFs enhance light absorption, while nanoribbons contribute to improved conductivity [172]. Moreover, nanoribbons may be customized to achieve precise band gaps for enhanced light absorption, and their resilient structure enhances the stability of the photocatalyst, making them suitable for usages such as pollutant degradation and WS [323,324]. For example, Ma et al. [325] engineered a composite nanophotocatalyst, ZIF-8@TiO_2-NBS, exhibiting improved CO_2RR efficiency under visible ligh. The catalyst was created by functionalizing anatase-phase TiO_2 nanoribbons with zeolitic imidazolate framework-8 (ZIF-8) utilizing ultrasonic synthesis, improving the component ratio. The resultant composite attained a surface area of 1352.31 m^2/g and retained a stable mesoporous morphology. Under visible ligh, it demonstrated a remarkable methane (CH_4) production of 29.53 $\mu mol \cdot g^{-1} \cdot h^{-1}$ and a selectivity of 71.97%, indicating its effectiveness in photocatalytic CO_2RR. The assessment of

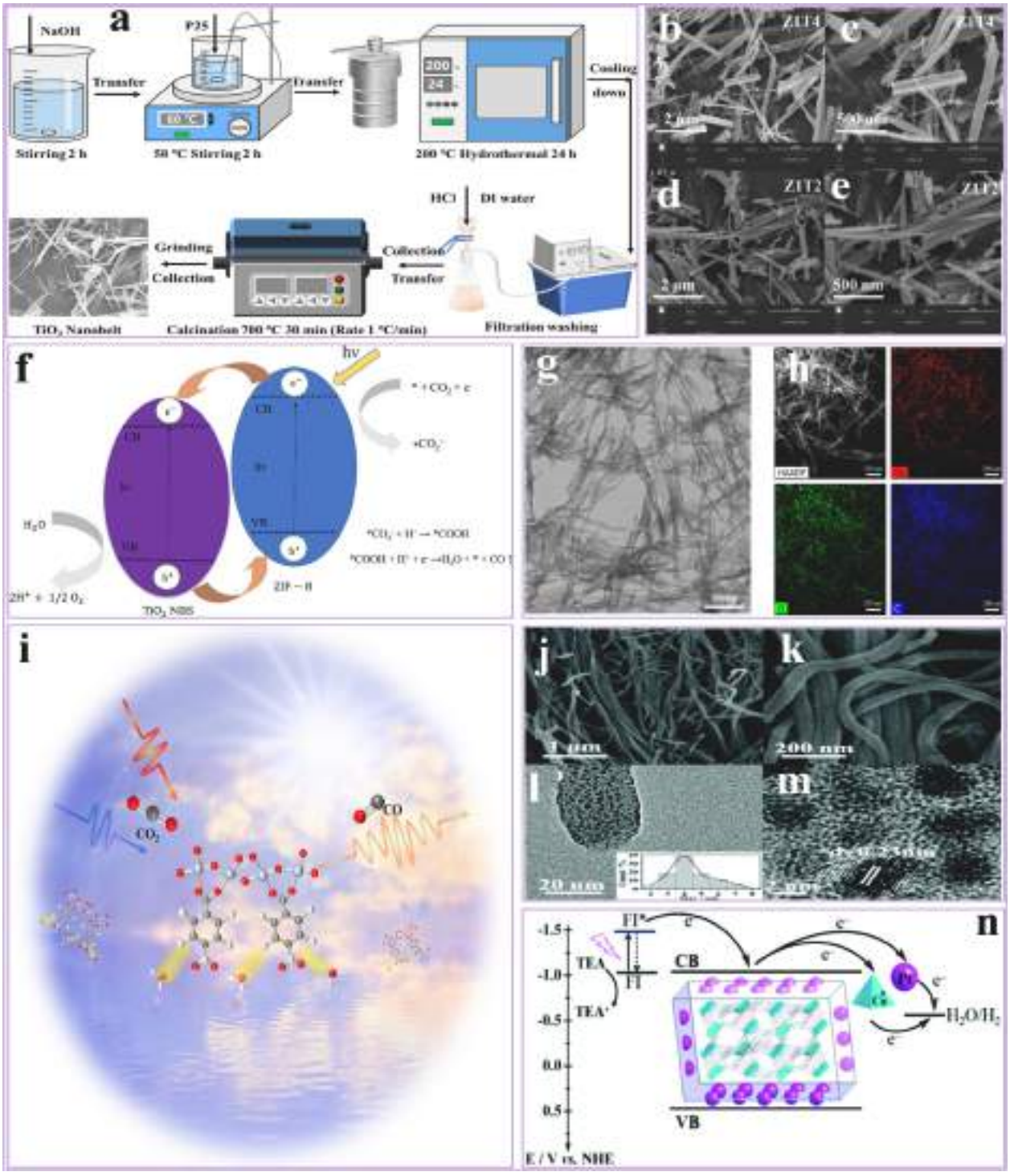

Fig. 21. (a) Synthesis process; (b–e) SEM analysis of TiO_2-NBS; (f) Proposed photocatalytic CO_2RR of TiO_2-NBS, reproduced with permission from ref [325] Copyright © 2023, American Chemical Society. (g) TEM analysis; (h) EDS mapping of Cu MOF nanoribbons; (i) Proposed CO_2 photoreduction mechanism of Cu MOF nanoribbons, reproduced with permission from ref [326] Copyright © 2024, John Wiley and Sons. (j, k) SEM; (l) TEM; (m) HRTEM analysis of Cu^{II}-MOF; (n) Proposed process for photocatalytic HER using the Pt/Cu^{II}-MOF composite, reproduced with permission from ref [327] Copyright © 2021, Royal Society of Chemistry.

CO_2 efficiency was performed in a sealed reactor fitted with a heating jacket, a sapphire glass light window, and a xenon light source (Fig. 21a). The catalyst underwent pretreatment at 300°C in an argon environment to eliminate moisture and impurities. For the experiment, 30 mg of catalyst was disseminated in 3 mL of deionized water, positioned in a 100 mL reactor, subjected to vacuum treatment, and then filled with 500 mL of CO_2 gas. The reactor was heated to 150°C and exposed to illumination of 1 kW/m^2. Upon stabilization, 1 mL of gas was originally removed for baseline analysis. Then, 1 mL gas samples were collected hourly and analyzed utilizing a gas chromatograph equipped with thermal conductivity and hydrogen ion detectors. Fig. 21b–e shows SEM analysis of ZIF-8/TiO_2 composite catalysts at various proportions. The photos demonstrate that NP is consistently and densely integrated into the TiO_2 nanoribbons, suggesting the successful inclusion of ZIF-8. Furthermore, the particle density on the TiO_2 surface escalates with increased ZIF-8 doping, indicating effective manipulation of ZIF-8/TiO_2 ratios by adjusting the precursor mixture. Furthermore, In-situ IR spectroscopy elucidated the reaction process by monitoring intermediate H_2O and CO_2RR products on the catalyst surface. The spectra exhibit clear vibrational absorption peaks that signify CO_2 adsorption and the production of intermediate species. $Z1T_2$ demonstrates enhanced adsorption and activation of CO_2 and H_2O relative to TiO_2. Upon heating to 150°C and exposure to light, both catalysts generate CH_4 and CO gasses; however, $Z1T_2$ displays supplementary peaks indicative of superior performance. Both TiO_2 and $Z1T_2$ exhibit analogous intermediate species, suggesting comparable reaction pathways, with *COOH potentially serving as a significant reactive material (Fig. 21f). Their research demonstrates that examining the CO_2RR routes, charge transfer kinetics, intermediate species generation, and surface reactions in the ZIF-8@TiO_2 nanoribbon catalysts would provide insights for enhancing their efficiency. Similarly, Zhao et al. [326] synthesized 2D MOFs with homogenous monometal active sites for efficient and selective CO_2RR. They synthesized water-stable Cu-derived MOF nanoribbons with unsaturated single Cu(II) sites. Characterization results demonstrated that synthesizing significant intermediates COOH* and CO* is exothermic and spontaneous, but the competing HER process is endothermic and non-spontaneous, resulting in selective CO_2RR. In an aqueous $KHCO_3$ mixture, these Cu-derived MOF nanoribbons attained an average CO production of 82 μmol g^{-1} h^{-1} with 97% selectivity over 72 hours, comparable to other photocatalysts under analogous conditions. Hydro-stable Cu-derived MOFs nanoribbons were produced by a facile wet chemical method, using benzenedicarboxylic acid as the organic linker and copper nitrate as the metal node. TEM analysis verified that the synthesized MOFs had a structure akin to previously documented nickel-based MOFs and demonstrated stability in water for six months (Fig. 21g). The EDS mapping demonstrated a uniform distribution of Cu, C, and O throughout the sample (Fig. 21h). Photocatalytic experiments were performed at air pressure and room temperature to evaluate the CO_2RR effectiveness of water-stable Cu MOFs nanoribbons. The primary result was CO, accompanied by a small quantity of H_2, in both CO_2-saturated water and potassium bicarbonate ($KHCO_3$) mixtures. No liquid goods containing carbon were identified. The Cu MOFs nanoribbons exhibited a CO evolution rate of 82 μmol g^{-1} h^{-1} with 97% selectivity in a 1 M $KHCO_3$ mixture and 56 μmol g^{-1} h^{-1} with 92% selectivity in purified water. The rate of CO evolution and selectivity improved with increasing $KHCO_3$ concentration, presumably owing to augmented CO_2 hydration and pH modulation, which inhibited H_2 production. The findings demonstrate that alkali salt in a mixture enhances the CO_2RR efficiency of Cu MOFs nanoribbons, rendering their activity and selectivity equivalent to other photocatalysts under analogous circumstances (Fig. 21i). Their research indicates that monometallic catalytic center MOFs photocatalysts may systematically control the activity and selectivity of CO_2RR. Furthermore, Li et al. [327] synthesized a crystalline microporous Cu^{II}-derived MOF (Cu^{II}-MOF) and created a series of Pt/Cu^{II}-MOF nanoribbons with varying loadings of Pt NPs. These materials served as photocatalysts for HER via WS. The improved Pt(4.38 wt%)/Cu^{II}-MOF nanoribbon exhibited a markedly improved HER rate of 2.51 μmol g^{-1} h^{-1}, surpassing pure Pt NPs and Cu^{II}-MOF by factors of 4.7 and 1.9, respectively. The enhancement was ascribed to the interaction of the catalytic Cu^{II} and Pt centers, where electronic interactions between Pt and Cu^{II} reduced charge transfere resistance and favorably affected the CB potential. The SEM analysis of Pt/Cu^{II}-MOF hybrids with differing Pt concentrations exhibit uniform nanoribbons. The amounts of Pt doping significantly affect the ribbon size, with dimensions varying from around 50 nm for Pt (3.50 wt.%)/Cu^{II}-MOF to about 10 nm for Pt(5.99 wt.%)/Cu^{II}-MOF (Fig. 21j, k). TEM analysis of Pt(4.38 wt.%)/Cu^{II}-MOF reveals that Pt NPs, about 4 nm in diameter, are evenly distributed on the ribbon surface. At the same time, their size exceeds the void window dimensions, potentially leading to instability during recycling (Fig. 21l). HR-TEM reveals a d-spacing of about 0.23 nm, which corresponds to the Pt (111) crystal plane (Fig. 21m). Fluorescence quenching investigations demonstrate that Cu^{II}-MOF and Pt(4.38 wt.%)/CuII-MOF proficiently receive photoelectrons from excited fluorescence (FI*), exhibiting substantial increases in quenching constants (*Ksv*) of 580 and 2610 M^{-1}, respectively. This signifies effective electron transport to the photocatalysts without physical adsorption disruption. The quadrupling of *Ksv* highlights the synergistic interactions between Pt and Cu^{II}. The suggested process entails the excitation of FI by visible light to FI*, leading to fast electron transfer to the CB of Pt(4.38 wt.%)/Cu^{II}-MOF, augmenting H_2 evolution. The Cu^{II} center also enhances the photocatalytic performance (Fig. 21n). Their research presents a novel perspective for the rational design of extremely resilient and structured microporous MOFs composites with many photoactive metal sites. More importantly, we have included a comprehensive table that summarizes the various MOFs morphologies, their notable characteristics, related challenges, and possible alternatives, including metal-free polymeric materials for comparison in Table. 2.

4. Conclusions and future prospective

The development of metal-organic frameworks (MOFs) has emerged as a transformative approach in the field of photocatalysis due to their tunable structures, high surface areas, and versatile chemical functionalities. However, the role of MOFs morphology in enhancing photocatalytic performance has remained underexplored. This review comprehensively examines, for the first time, the critical relationship between MOFs morphology and photocatalytic efficiency, offering significant insights into the rational design of advanced photocatalysts. Key factors influencing MOF morphology were systematically analyzed, such as defects, porosity, precursors, solvents, surfactants, post-synthesis treatments, and synthesis techniques, including hydrothermal, microwave-assisted, solvothermal, and sonochemical methods. These factors play a vital role in tailoring MOFs structures to achieve specific morphological features, ultimately influencing their photocatalytic performance. Seventeen distinct MOFs morphologies were thoroughly discussed, including nanosheets, nanofilms, nanotubes, nanorods, nanowires, nanoparticles, quantum dots, hollow structures, hierarchical architectures, sea urchin-like forms, monoliths, nanocages, core-shell, yolk-shell, aerogels, nanoflowers, and nanoribbons. Each morphology provides unique advantages in photocatalytic applications by enhancing key parameters such as charge transfer, light absorption, active site exposure, and reaction kinetics. For example, two-dimensional nanosheets and nanofilms exhibit excellent light-harvesting properties due to their large surface areas and short diffusion pathways, while hierarchical and hollow structures facilitate improved mass transfer and active site accessibility. In addition, the review underscores that morphology engineering significantly influences photocatalytic efficiency through three primary mechanisms: (1) enhancing charge carrier separation and transport, (2) optimizing light absorption across a broader spectral range, and (3) increasing active site availability for surface reactions. These mechanisms collectively lead to improved energy conversion

Table 2
The comparative evaluation of MOFs morphologies, challenges, and solutions.

Morphology	Key Properties	Challenges	Alternative Materials	Comparison with MOFs	Refs.
Nanosheets	Substantial surface area, significant active site accessibility	Fragile nature, stacking tendencies	Graphitic carbon nitride (g-C_3N_4)	g-C_3N_4 is metallic-free and feasible but has a smaller surface area	[328–333]
Nanofilms	Fragile, flexible, with variable conductivity	Poor stability and difficult creation	Conductive polymers	Conductive polymers provide mobility but reduced porosity	[334–339]
Nanotubes	Excellent electron transfer and durability	Complicated synthesis, low dispersion	Conductive polymers (e.g., PEDOT:PSS)	Conductive polymers are versatile, accessible, and reduced porous	[340–345]
Nanorods	Directional charge transfer, good conductivity	Controlled morphology, low porosity	Carbon nanotubes (CNTs)	Better electrical conductivity, reduced tunability in CNTs	[346–352]
Nanowires	Excellent aspect ratio, effective charge transfer	Flexibility and synthetic complexity	Metal-free nanowires	Metal-free solutions provide sustainability but diminish stability	[353–359]
Nanoparticles	Wide surface area, increased responsiveness	Weak stability, aggregation	Covalent organic frameworks (COFs)	Chemically stable and metallic-free COFs	[360–364]
Quantum Dots	Quantum confinement, adjustable band gap	Poor yield and scalability difficulties	Carbon quantum dots (CQDs)	CQDs are metallic-free and biocompatible, but with poorer stability	[365–368]
Hollow	Excellent porosity and efficient diffusion.	Structural collapse and challenging synthesis	Porous organic polymers (POPs)	POPs are thin, chemically adjustable, and have decreased crystallinity	[369–374]
Hierarchical	Multi-scale solubility and synergistic characteristics	Complicated production and repeatability issues	Hybrid organic-inorganic frameworks	Hybrids offer better stability but are harder to optimize	[375–380]
Sea Urchin-like	Substantial surface roughness leads to enhanced catalysis	Fragility and challenging synthesis	Hyper crosslinked polymers (HCPs)	HCPs have great mechanical stability but have a lesser surface area	[381–387]
Monolith	Excellent mechanical stability and scalable shape	Challenging shaping and processing restrictions	Metal-free aerogels	Aerogels are ultralight and feasible, but fewer crystalline	[388–392]
Nanocages	Hollow structure with high surface-to-volume ratio	Stability issues, synthesis complexity	Porous carbon frameworks	Porous carbon structure offer stability but have a lesser flexibility	[393–399]
Core-Shell	Versatility, customized interfaces	Insufficient interface durability and synthesis problems	Layered double hydroxides (LDHs)	LDHs are affordable but lack precision tuning capability	[400–403]
Yolk-Shell	Excellent structural stability with dual functionality	Complicated fabrication, minimal repeatability	Dendritic polymers	Dendritic frameworks offer high porosity but poor crystallinity	[404–408]
Aerogel	Ultralightweight, low porosity	Mechanical instability, costly production	Carbon aerogels	Carbon aerogels are feasible, but have less chemical flexibility	[409–412]
Nanoflowers	Strong active site density and biomimetic design	Challenging morphological regulation	Self-assembled polymeric systems	Polymers are simple to make yet unstable	[413–418]
Nanoribbons	Anisotropic charge transference and flexibility	Stability difficulties and synthesis issues	Boron nitride (BN) nanoribbons	Highly conductive BN nanoribbons are hard to synthesis	[419–424]

efficiency and better catalytic performance in applications such as water splitting, CO_2 reduction, and pollutant degradation. By establishing a direct correlation between morphology and photocatalytic functionality, this work provides a valuable roadmap for the rational design of high-efficiency, cost-effective MOF-based photocatalysts. The findings highlight the untapped potential of morphology engineering as a strategy to further optimize MOF performance.

Although this review has explored the effects of various morphological aspects of MOFs on enhancing photocatalytic applications, several areas still require further investigation, including:

- The ongoing advancements in MOFs morphology engineering open several exciting avenues for future research and application. As researchers continue to explore and refine various morphologies such as nanosheets, nanotubes, nanorods, and quantum dots, they are likely to unlock new levels of photocatalytic efficiency and versatility. The ability to fine-tune these structures at the nanoscale will further enhance light absorption, charge transfer, and active site accessibility, driving improvements in both environmental remediation and energy conversion.
- Future research may focus on developing more sophisticated morphologies, such as multi-dimensional nanostructures and hybrid materials, to achieve even greater catalytic performance. Investigating the synergistic effects of combining different morphological features within single MOFs could lead to breakthroughs in charge separation and electron lifetime, addressing current limitations in photocatalytic efficiency.
- Monolayer MOFs nanosheets exhibit excellent dispersion in various solvents and provide a higher number of accessible nitrogen sites, which can act as anchors for single atoms, bridging hetero- and homogeneous reactions. While precise control of reaction conditions is often required to achieve optimal catalytic performance in material synthesis, this degree of regulation is challenging to maintain in large-scale production.
- The investigation of metal-free polymeric materials, including g-C_3N_4, CMPs, and COFs, provides a green and environmentally friendly substitute. These materials demonstrate inherent semiconductor characteristics, adjustable band structures, and superior chemical stability. Morphological engineering including the fabrication of nanosheets, hollow spheres, or porous networks that can augment their surface area and separation of charged particles performance, comparable to methodologies used for MOFs.
- Future investigations may concentrate on the development of MOF-polymer hybrid structures or MOF-carbon materials that integrate the structural adaptability of MOFs with the reliability and photocatalytic performance of organic frameworks. These materials may use combined effects to surpass the confines of each component and enhance charge transmission and stability.
- Researchers must develop milder and more efficient synthesis techniques to enable large-scale commercial production of high-performance MOF-based catalysts. To further enhance catalytic efficiency, it is crucial to explore additional modification strategies, including investigating various forms of MOF and identifying novel doping agents.
- The developing domain of MOF-derived semiconductors presents promising prospects for improving photocatalytic efficiency by preserving the inherent crystal structure of their precursor MOFs. Through pyrolysis or calcination, these materials convert into carbonaceous materials, metal oxides, or carbon-metal mixtures that preserve essential structural characteristics such as porosity, surface area, and morphological integrity, hence enhancing their photocatalytic function. Future studies will probably concentrate on connecting MOF structure with the design and optimization of MOF-based semiconductors, using the morphological influence inherent

to MOF fabrication to modify the attributes of the resultant semiconductor materials.

- By precisely adjusting the synthesis parameters, including temperature, environment, and metal precursor selection, it is feasible to generate MOF-derived semiconductors with exact regulation of their shape and electronic characteristics. This methodology will facilitate the development of materials that maintain the advantageous features of the parent MOFs, particularly elevated surface area and adjustable porosity, while also exhibiting enhanced photocatalytic capabilities attributable to optimized semiconductor attributes, including improved separation of charged particles, electron accessibility, and light absorption.
- Further investigation is required to understand the interaction between defects and the various morphological aspects of MOFs and their impact on photocatalytic performance. Both experimental and computational approaches should be employed. Reports suggest that the combination of vacancies and dopants has a synergistic effect on photocatalysis. Therefore, a comprehensive study focusing on the interrelation and synergistic effects of defect-related factors in MOFs is essential.
- The diverse design strategies and vast potential for solar energy conversion highlight the immense possibilities for structural advancements in MOFs. This field remains highly promising, with great potential for future groundbreaking developments.
- Additionally, exploring novel applications of advanced MOFs morphologies, including in complex reaction systems and under varying environmental conditions, could expand the utility of these materials. The integration of MOFs into practical technologies, such as scalable photocatalytic reactors or devices for sustainable energy generation, represents a promising direction for future development.

Overall, the continued innovation in MOFs morphology and structure holds the potential to transform the landscape of photocatalysis, pushing the boundaries of what is achievable in both fundamental research and practical applications. Additionally, Scheme 2 illustrates the real-world uses of MOFs, highlighting their multipurpose and significance throughout several proficient technological fields. This illustration was developed to enhance the textual discourse and provide readers with a clear visual description of the many tasks that MOFs fulfill, owing to their highly adjustable architectures and attributes based on morphology. The image especially illustrates how MOFs, characterized by their tunable pore diameters, elevated surface areas, and diverse chemical capabilities, may be efficiently used in several domains.

Authors Contribution

The manuscript was written with contributions from all authors. All authors have approved the final version of the manuscript work.

CRediT authorship contribution statement

Hamid Ali: Conceptualization, Data curation, Writing – original draft, Writing – review & editing. **Obaid Iqbal:** Conceptualization, Data curation, Writing – original draft, Writing – review & editing. **Basem Al Alwan:** Validation, Methodology, Formal analysis. **Amal Abdulrahman:** Validation, Methodology, Formal analysis. **Yasin Orooji:** Validation, Methodology, Formal analysis. **Eida S. Al-Farraj:** Visualization, Investigation, Resources. **Muhammad Sadiq:** Visualization, Investigation, Resources. **Sajid Imran:** Visualization, Investigation, Resources. **Ahmed M. Abu-Dief:** Visualization, Investigation, Resources. **Dewu Yue:** Project administration, Funding acquisition, Supervision, Writing – review & editing. **Asif Hayat:** Project administration, Funding acquisition, Supervision, Writing – review & editing.

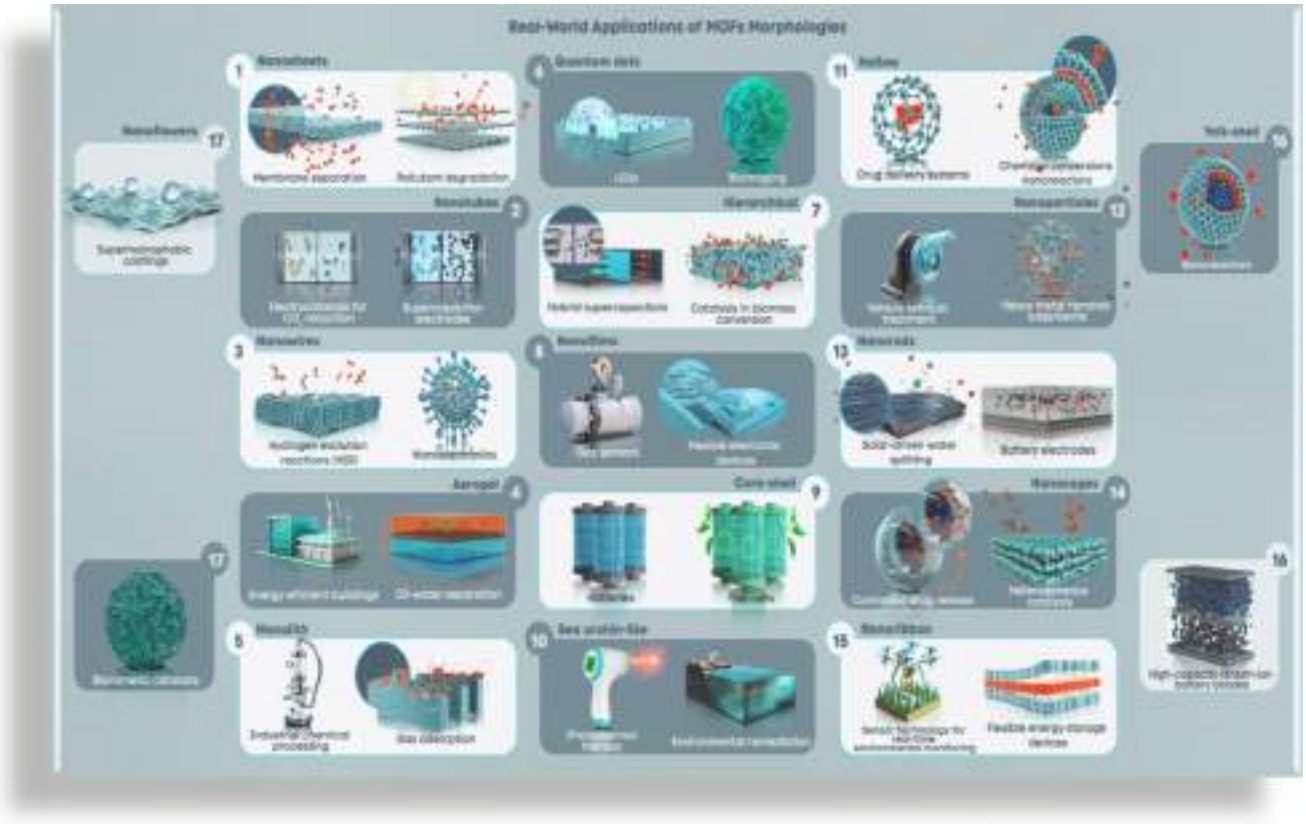

Scheme 2. Graphical depiction of commercial applications of morphology-based MOFs, emphasizing their many functions in environmental cleanup, conversion of energy, gas storage, and catalysis.

Declaration of competing interest

The authors declare that there are no known financial or personal conflicts of interest that could have influenced the work reported in this paper.

Acknowledgments

This work was supported by the King Khalid University, Abha, Saudi Arabia. The authors extend their appreciation to the Deanship of Scientific Research at King Khalid University for funding this work through the Large Groups Project under grant number (R.G.P. 2/335/46)). The authors also further extend their appreciation to the Guangdong Office of Research Projects at the Provincial University (2024KCXTD064).

Appendix A. Supplementary data

Supplementary data to this article can be found online at https://doi.org/10.1016/j.ccr.2025.216822.

Data availability

Data will be made available on request.

References

[1] F.P. Perera, Environ. Health Perspect. 125 (2017) 141–148.
[2] C.M. Anderson, K.A. Kissel, C.B. Field, K.J. Mach, Environ. Sci. Technol. 52 (2018) 10829–10838.
[3] N. Kittner, F. Lill, D.M. Kammen, Nat. Energy 2 (2017) 1–6.
[4] A.C. Ferreira, J. Silva, S. Teixeira, J.C. Teixeira, S.A. Nebra, Renew. Energy 154 (2020) 581–597.
[5] L. Pan, S. Wang, J. Xie, L. Wang, X. Zhang, J.-J. Zou, Nano Energy 28 (2016) 296–303.
[6] Z. Xiong, Z. Lei, Y. Li, L. Dong, Y. Zhao, J. Zhang, J Photochem Photobiol C: Photochem Rev 36 (2018) 24–47.
[7] J. Albero, Y. Peng, H. García, ACS Catal. 10 (2020) 5734–5749.
[8] C.-W. Huang, V.-H. Nguyen, S.-R. Zhou, S.-Y. Hsu, J.-X. Tan, K.C.-W. Wu, Sustainable Energy & Fuels 4 (2020) 504–521.
[9] S.A. Younis, E.E. Kwon, M. Qasim, K.-H. Kim, T. Kim, D. Kukkar, X. Dou, I. Ali, Prog. Energy Combust. Sci. 81 (2020) 100870.
[10] I. Ashraf, S. Rizwan, M. Iqbal, Frontiers Mater. 7 (2020) 181.
[11] A. Ray, S. Sultana, S.P. Tripathy, K. Parida, ACS Sustain. Chem. Eng. 9 (2021) 6305–6317.
[12] D. Kandi, S. Martha, A. Thirumurugan, K. Parida, J. Phys. Chem. C 121 (2017) 4834–4849.
[13] G. Swain, S. Sultana, K. Parida, Inorg. Chem. 58 (2019) 9941–9955.
[14] S. Subudhi, S.P. Tripathy, K. Parida, Inorganic Chem. Frontiers 8 (2021) 1619–1636.
[15] S. Subudhi, S. Mansingh, S.P. Tripathy, A. Mohanty, P. Mohapatra, D. Rath, K. Parida, Catal. Sci. & Technol. 9 (2019) 6585–6597.
[16] X. Deng, L. Yang, H. Huang, Y. Yang, S. Feng, M. Zeng, Q. Li, D. Xu, Small 15 (2019) 1902287.
[17] S. Kuppusamy, D. Jagadeesan, A.M. Mohan, A.P. Veedu, A.E. Jiji, A.M. John, P. Deivasigamani, J. Environ. Chem. Engineering 11 (2023) 110355.
[18] J. Sun, X. Li, J. Li, M. Mu, X. Yin, Colloids Surf. A Physicochem. Eng. Asp. 653 (2022) 129940.
[19] S.K. Sharma, A. Kumar, G. Sharma, T. Wang, A. Iglesias-Juez, P. Dhiman, J. Mol. Liq. 382 (2023) 121890.
[20] D. Mukherjee, B. Van der Bruggen, B. Mandal, Chemosphere 295 (2022) 133835.
[21] J. Ren, M. Ledwaba, N.M. Musyoka, H.W. Langmi, M. Mathe, S. Liao, W. Pang, Coord. Chem. Rev. 349 (2017) 169–197.
[22] X. Hou, J. Wang, B. Mousavi, N. Klomkliang, S. Chaemchuen, Dalton Trans. 51 (2022) 8133–8159.
[23] I. Bechis, A.F. Sapnik, A. Tarzia, E.H. Wolpert, M.A. Addicoat, D.A. Keen, T. D. Bennett, K.E. Jelfs, Chem. Mater. 34 (2022) 9042–9054.
[24] W. Xiang, Y. Zhang, Y. Chen, C.-J. Liu, X. Tu, J. Mater. Chem. A 8 (2020) 21526–21546.
[25] Z. Guo, X. Liu, Y. Che, H. Xing, Inorg. Chem. 63 (2024) 13005–13013.
[26] Y.L. Dong, Y. Jiang, S. Ni, G.W. Guan, S.T. Zheng, Q. Guan, L.M. Pei, Q.Y. Yang, Small 20 (2024) 2308005.
[27] D.K. Yoo, H.C. Woo, S.H. Jhung, ACS Appl. Mater. Interfaces 12 (2020) 34423–34431.
[28] Y. Sun, H. Ji, Y. Sun, G. Zhang, H. Zhou, S. Cao, S. Liu, L. Zhang, W. Li, X. Zhu, Angew. Chem. 136 (2024) e202316973.
[29] X. Zhang, B. Li, J. Xu, X. Zhang, Y. Shi, C. Zhu, X. Zhang, Y. Chen, Adv. Funct. Mater. 33 (2023) 2210456.
[30] V. Gargiulo, M. Alfè, F. Raganati, L. Lisi, R. Chirone, P. Ammendola, Fuel 222 (2018) 319–326.
[31] M. Lan, R.-M. Guo, Y. Dou, J. Zhou, A. Zhou, J.-R. Li, Nano Energy 33 (2017) 238–246.
[32] Y. Tian, Y. Liu, H. Zhu, D. Nie, S. Khan, X. Yang, Inorg. Chem. 63 (2024) 19885–19896.
[33] I. Hussain, C. Lamiel, S. Sahoo, M. Ahmad, X. Chen, M.S. Javed, N. Qin, S. Gu, Y. Li, T. Nawaz, Materials Today Phys. 27 (2022) 100844.
[34] D. Liu, F. Dai, Z. Tang, Y. Liu, C. Liu, Mater. Res. Bull. 65 (2015) 287–292.
[35] Y. Du, D. Du, Chem. Phys. Lett. 860 (2025) 141790.
[36] G. Song, X. Zhu, R. Chen, Q. Liao, Y.-D. Ding, L. Chen, RSC Adv. 6 (2016) 19069–19077.
[37] M. Radhika, R. Srilakshmi, V. Tejashree, K. Venkatesh, M.S. Kamath, K. Nagaraju, J. Energy Storage 61 (2023) 106766.
[38] J. Hao, Z. Jiang, H.A. Khan, O. El Tall, A. Farooq, Fuel 318 (2022) 123638.
[39] H. Chen, Z.-G. Gu, S. Mirza, S.-H. Zhang, J. Zhang, J. Mater. Chem. A 6 (2018) 7175–7181.
[40] S. Zang, X. Cai, Y. Zang, F. Jing, Y. Lu, S. Tang, F. Lin, L. Mo, Inorg. Chem. 63 (2024) 6546–6554.
[41] T. Gholami, H. Seifi, E.A. Dawi, M. Pirsaheb, S. Seifi, A.M. Aljeboree, A.-H. M. Hamoody, U.S. Altimari, M.A. Abass, M. Salavati-Niasari, Mater. Sci. Eng. B 304 (2024) 117370.
[42] A.A. Tezerjani, R. Halladj, S. Askari, RSC Adv. 11 (2021) 19914–19923.
[43] J. Łuczak, M. Kroczewska, M. Baluk, J. Sowik, P. Mazierski, A. Zaleska-Medynska, Adv. Colloid Interf. Sci. 314 (2023) 102864.
[44] J. Hwang, R. Yan, M. Oschatz, B.V. Schmidt, J. Mater. Chem. A 6 (2018) 23521–23530.
[45] Y. Li, D. Han, Z. Wang, F. Gu, ACS Appl. Mater. Interfaces 16 (2024) 7080–7096.
[46] N. Kaeosamut, P. Chaichana, A. Watwiangkham, S. Suthirakun, S. Wannapaiboon, N. Sammawipawekul, Y. Chimupala, S. Yimklan, Inorg. Chem. 62 (2023) 19908–19921.
[47] J. Zhao, X. Liu, Y. Wu, D.-S. Li, Q. Zhang, Coord. Chem. Rev. 391 (2019) 30–43.
[48] S. Wang, L. Zhang, M. Zhang, L. Xu, Q. Hu, T. Yang, K. Tu, M. Wu, D. Yu, Water 14 (2022) 1864.
[49] H.N. Abdelhamid, Nanotechnology 30 (2019) 435601.
[50] M.A. Molina, N.R. Habib, I. Díaz, M. Sánchez-Sánchez, Catal. Today 394 (2022) 117–124.
[51] N. Li, M. Wu, Z. Guo, Q. Li, G. Sun, W. Shen, M. Shi, J. Ma, Solid State Sci. 148 (2024) 107436.
[52] V. Valtchev, G. Majano, S. Mintova, J. Pérez-Ramírez, Chem. Soc. Rev. 42 (2013) 263–290.
[53] H.-G. Jin, P.-C. Zhao, Y. Qian, J.-D. Xiao, Z.-S. Chao, H.-L. Jiang, Chem. Soc. Rev. 53 (2024) 9378–9418.
[54] R.D.A. Bessa, (2021).
[55] Q. Chen, M. Yao, Y. Zhou, Y. Sun, G. Zhang, H. Pang, Coord. Chem. Rev. 517 (2024) 216016.
[56] M. Chen, M. Sun, X. Cao, H. Wang, L. Xia, W. Jiang, M. Huang, L. He, X. Zhao, Y. Zhou, Coord. Chem. Rev. 510 (2024) 215849.
[57] G. Luciani, C. Imparato, G. Vitiello, Catalysts 10 (2020) 103.
[58] X. Zhao, X. Gao, R. Ding, H. Huang, X. Gao, B. Liu, J. Colloid Interface Sci. 639 (2023) 59–67.
[59] W. Lian, Y. Huang, Q. Yin, Z. Guo, Y. Xu, T. Miao, J. Colloid Interface Sci. 675 (2024) 94–103.
[60] F.M. Sladek, Mol. Cell. Endocrinol. 334 (2011) 3–13.
[61] N.C. Burtch, K.S. Walton, Acc. Chem. Res. 48 (2015) 2850–2857.
[62] D. Zhao, D.J. Timmons, D. Yuan, H.-C. Zhou, Acc. Chem. Res. 44 (2011) 123–133.
[63] K.J. Gagnon, H.P. Perry, A. Clearfield, Chem. Rev. 112 (2012) 1034–1054.
[64] T.-H. Chen, I. Popov, W. Kaveevivitchai, O.S. Miljanić, Chem. Mater. 26 (2014) 4322–4325.
[65] J. Wang, A.S. Cherevan, C. Hannecart, S. Naghdi, S.P. Nandan, T. Gupta, D. Eder, Appl. Catal. B Environ. 283 (2021) 119626.
[66] Y. Liu, X. Xin, Y. Shi, Z. Zhao, J. Tan, D. Yang, Z. Jiang, Chem. Eng. J. 482 (2024) 149193.
[67] M. Ahmad, K.A. Siddiqui, J. Mol. Struct. 1265 (2022) 133399.
[68] Q. Yang, D. Liu, C. Zhong, J.-R. Li, Chem. Rev. 113 (2013) 8261–8323.
[69] M.U. Rahman, S. Khan, H. Khan, A. Ali, F. Sarwar, Chem. Prod. Process. Model. 19 (2024) 473–515.
[70] M.H. Zawawi, A. Saleha, A. Salwa, N. Hassan, N.M. Zahari, M.Z. Ramli, Z.C., Muda, in: AIP conference proceedings, AIP Publishing, 2018.
[71] T. Norton, D.-W. Sun, Trends Food Sci. Technol. 17 (2006) 600–620.
[72] M. Rashid, S. Parsaei, A. Ghoorchian, K. Dashtian, D. Mowla, J. Ind. Eng. Chem. 121 (2023) 275–286.
[73] Y. Chen, Q. Sun, Z. Ni, X. Tu, C. Sun, S. Zhu, X. Duan, M. Jiang, Z. Xie, M. Liu, Chem. Eng. J. 482 (2024) 148853.
[74] W. Chen, L. Du, C. Wu, Hydrothermal synthesis of MOFs, in: Metal-organic frameworks for biomedical applications, Elsevier, 2020, pp. 141–157.
[75] M. Muslim, A. Ali, M. Ahmad, Hydrothermal synthesis of metal–organic frameworks, in: Synthesis of Metal-Organic Frameworks Via Water-based Routes, Elsevier, 2024, pp. 73–92.
[76] N. Stock, S. Biswas, Chem. Rev. 112 (2012) 933–969.
[77] J. Zheng, L. Sun, C. Jiao, Q. Shao, J. Lin, D. Pan, N. Naik, Z. Guo, Colloids Surf. A Physicochem. Eng. Asp. 623 (2021) 126629.
[78] Y. Wang, S. Ge, W. Cheng, Z. Hu, Q. Shao, X. Wang, J. Lin, M. Dong, J. Wang, Z. Guo, Langmuir 36 (2020) 9658–9667.
[79] P.T. Phan, J. Hong, N. Tran, T.H. Le, Nanomaterials 13 (2023) 352.

[80] R. Vakili, S. Xu, N. Al-Janabi, P. Gorgojo, S.M. Holmes, X. Fan, Microporous Mesoporous Mater. 260 (2018) 45–53.
[81] J. Klinowski, F.A.A. Paz, P. Silva, J. Rocha, Dalton Trans. 40 (2011) 321–330.
[82] V. Isaeva, L. Kustov, Russ. Chem. Bull. 65 (2016) 2103–2114.
[83] X. Liu, Y. Li, Y. Liu, S. Li, L. Feng, J. Zhuang, J. Tang, J. Alloys Compd. 922 (2022) 165939.
[84] X. Yu, Y. Hu, X. Luan, S.J. Shah, L. Liu, C. Li, Y. Ren, L. Zhou, J. Li, J. Deng, Chem. Eng. J. 476 (2023) 146878.
[85] D. Sud, G. Kaur, Polyhedron 193 (2021) 114897.
[86] M.S. Khan, M. Shahid, Synthesis of metal-organic frameworks (MOFs): routes to various MOF topologies, morphologies, and composites, in: Electrochemical applications of metal-organic frameworks, Elsevier, 2022, pp. 17–35.
[87] P. Pachfule, R. Das, P. Poddar, R. Banerjee, Cryst. Growth Des. 11 (2011) 1215–1222.
[88] M. Mubeen, M. Tabish, N. Muhammad, M.A. Mushtaq, G. Yasin, Multifunctional Coordination Materials for Green Energy Technologies (2024) 37.
[89] W. Shen, X. Guo, H. Pang, Molecules 27 (2022) 8226.
[90] H. Li, D. Li, M. Long, X. Bai, Q. Wen, F. Song, Colloids Surf. A Physicochem. Eng. Asp. 658 (2023) 130646.
[91] X. Su, T. Xu, R. Ye, C. Guo, S.M. Wabaidur, D.-L. Chen, S. Aftab, Y. Zhong, Y. Hu, J. Colloid Interface Sci. 646 (2023) 129–140.
[92] C. Vaitsis, G. Sourkouni, C. Argirusis, Sonochemical synthesis of MOFs, in: Metal-organic frameworks for biomedical applications, Elsevier, 2020, pp. 223–244.
[93] S. Głowniak, B. Szczęśniak, J. Choma, M. Jaroniec, Molecules 28 (2023) 2639.
[94] M.R. Armstrong, S. Senthilnathan, C.J. Balzer, B. Shan, L. Chen, B. Mu, Ultrason. Sonochem. 34 (2017) 365–370.
[95] C. Vaitsis, G. Sourkouni, C. Argirusis, Ultrason. Sonochem. 52 (2019) 106–119.
[96] M. Bigdeli, A. Morsali, Ultrason. Sonochem. 27 (2015) 416–422.
[97] M. Tanhaei, A.R. Mahjoub, V. Safarifard, Ultrason. Sonochem. 41 (2018) 189–195.
[98] A. Dastbaz, J. Karimi-Sabet, M.A. Moosavian, Int. J. Hydrog. Energy 44 (2019) 26444–26458.
[99] O. Iqbal, J.C. Habumugisha, S. Feng, Y. Lin, W. Chen, W. Yu, L. Li, Polymers 13 (2020) 126.
[100] S. Barwich, J.M. de Araujo, A. Rafferty, C.G. da Rocha, M.S. Ferreira, J. N. Coleman, Carbon 171 (2021) 306–319.
[101] V. Guerra, C. Wan, V. Degirmenci, J. Sloan, D. Presvytis, T. McNally, Nanoscale 10 (2018) 19469–19477.
[102] P.H. Linh, P. Do Chung, N. Van Khien, L.T.M. Oanh, V.T. Thu, T.N. Bach, L. T. Hang, N.M. Hung, V.D. Lam, Diam. Relat. Mater. 111 (2021) 108214.
[103] W. Ahn, H.S. Song, S.-H. Park, K.-B. Kim, K.-H. Shin, S.N. Lim, S.-H. Yeon, Electrochim. Acta 132 (2014) 172–179.
[104] W. Xu, Y. Liang, Y. Su, S. Zhu, Z. Cui, X. Yang, A. Inoue, Q. Wei, C. Liang, Electrochim. Acta 211 (2016) 891–899.
[105] S. Kumar, S. Kumar, P. Sharma, V. Sharma, S. Katyal, J. Appl. Phys. 112 (2012).
[106] L. Pan, Z. Ji, X. Yi, X. Zhu, X. Chen, J. Shang, G. Liu, R.W. Li, Adv. Funct. Mater. 25 (2015) 2677–2685.
[107] Y. Chen, A. Huang, L. Zhang, Z. Bie, Microchim. Acta 187 (2020) 326.
[108] G. Xu, T. Yamada, K. Otsubo, S. Sakaida, H. Kitagawa, J. Am. Chem. Soc. 134 (2012) 16524–16527.
[109] W. Bai, S. Li, J. Ma, W. Cao, J. Zheng, J. Mater. Chem. A 7 (2019) 9086–9098.
[110] R.C. Arbulu, Y.B. Jiang, E.J. Peterson, Y. Qin, Angew. Chem. Int. Ed. 57 (2018) 5813–5817.
[111] X. Wang, A. Dong, Y. Hu, J. Qian, S. Huang, Chem. Commun. 56 (2020) 10809–10823.
[112] K.-Y. Zou, Y.-C. Liu, Y.-F. Jiang, C.-Y. Yu, M.-L. Yue, Z.-X. Li, Inorg. Chem. 56 (2017) 6184–6196.
[113] L. Zou, C.-C. Hou, Z. Liu, H. Pang, Q. Xu, J. Am. Chem. Soc. 140 (2018) 15393–15401.
[114] E. Mirzadeh, K. Akhbari, CrystEngComm 18 (2016) 7410–7424.
[115] Y.S. Li, H. Bux, A. Feldhoff, G.L. Li, W.S. Yang, J. Caro, Adv. Mater. 22 (2010) 3322–3326.
[116] L. Zou, M. Kitta, J. Hong, K. Suenaga, N. Tsumori, Z. Liu, Q. Xu, Adv. Mater. 31 (2019) 1900440.
[117] A.A. Ghassan, N.-A. Mijan, Y.H. Taufiq-Yap, Nanomaterials: an overview of nanorods synthesis and optimization, IntechOpen, 2019.
[118] M. Yuan, R. Wang, Z. Sun, L. Lin, H. Yang, H. Li, C. Nan, G. Sun, S. Ma, Inorg. Chem. 58 (2019) 11449–11457.
[119] N. Liu, Y. Yao, J.J. Cha, M.T. McDowell, Y. Han, Y. Cui, Nano Res. 5 (2012) 109–116.
[120] M. Meilikhov, K. Yusenko, D. Esken, S. Turner, G. Van Tendeloo, R.A. Fischer, Eur. J. Inorg. Chem. 2010 (2010) 3701–3714.
[121] C. Guo, Y. Zhang, Y. Guo, L. Zhang, Y. Zhang, J. Wang, Chem. Commun. 54 (2018) 252–255.
[122] L. Giri, S.R. Rout, R.S. Varma, M. Otyepka, K. Jayaramulu, R. Dandela, Nanotechnol. Rev. 11 (2022) 1947–1976.
[123] W. Lv, Y. Song, H. Pei, Z. Mo, J. Ind. Eng. Chem. 128 (2023) 17–54.
[124] D. Zhao, X. Wan, H. Song, L. Hao, Y. Su, Y. Lv, Sensors Actuators B Chem. 197 (2014) 50–57.
[125] D. Buso, J. Jasieniak, M.D. Lay, P. Schiavuta, P. Scopece, J. Laird, H. Amenitsch, A.J. Hill, P. Falcaro, Small 8 (2012) 80–88.
[126] M. Rahmani, A. Abbasi, M.-S. Hosseini, Appl. Surf. Sci. 648 (2024) 159014.
[127] Y. Pei, Z. Qi, X. Li, R.V. Maligal-Ganesh, T.W. Goh, C. Xiao, T. Wang, W. Huang, J. Mater. Chem. A 5 (2017) 6186–6192.
[128] T. Qiu, S. Gao, Z. Liang, D.G. Wang, H. Tabassum, R. Zhong, R. Zou, Angew. Chem. Int. Ed. 60 (2021) 17314–17336.
[129] Z.X. Cai, Z.L. Wang, J. Kim, Y. Yamauchi, Adv. Mater. 31 (2019) 1804903.
[130] P. Sarawade, H. Tan, D. Anjum, D. Cha, V. Polshettiwar, ChemSusChem 7 (2014) 529–535.
[131] Z. Wang, N. Yang, D. Wang, Chem. Sci. 11 (2020) 5359–5368.
[132] K. Li, J. Yang, J. Gu, Acc. Chem. Res. 55 (2022) 2235–2247.
[133] L. Feng, K.-Y. Wang, J. Willman, H.-C. Zhou, ACS Central Sci. 6 (2020) 359–367.
[134] K.-Y. Wang, L. Feng, T.-H. Yan, J.-S. Qin, C.-X. Li, H.-C. Zhou, ACS Mater. Lett. 3 (2021) 738–743.
[135] J. Cui, N. Gao, X. Yin, W. Zhang, Y. Liang, L. Tian, K. Zhou, S. Wang, G. Li, Nanoscale 10 (2018) 9192–9198.
[136] P. He, L. Hao, N. Liu, H. Bai, R. Niu, J. Gong, Chem. Eng. J. 423 (2021) 130268.
[137] L. Li, Y. Xu, H. Ye, D. Liu, P. Dai, X. Gu, T. Xing, Z. Li, M. Wang, M. Wu, J. Colloid Interface Sci. 687 (2025) 830–841.
[138] Y. Chen, X. Jin, W. Wang, W. Tang, C. Liu, S. Sun, Polym. Degrad. Stab. 230 (2024) 111052.
[139] J. Duan, Q. Liang, Y. Fu, J. Chang, Fuel 361 (2024) 130674.
[140] J. Ye, C. Li, L. Wang, Y. Yan, Y. Wang, J. Dai, Sep. Purif. Technol. 258 (2021) 117669.
[141] X. Qi, K. Liu, Z. Chang, Chem. Eng. J. 441 (2022) 135953.
[142] J. Hou, A.F. Sapnik, T.D. Bennett, Chem. Sci. 11 (2020) 310–323.
[143] P. Albacete, M. Asgari, Y. Yang, A.N. Al-Shanks, D. Fairen-Jimenez, Adv. Funct. Mater. 34 (2024) 2305979.
[144] F. Lorignon, A. Gossard, M. Carboni, Chem. Eng. J. 393 (2020) 124765.
[145] J. Fonseca, T. Gong, Coord. Chem. Rev. 462 (2022) 214520.
[146] Z. Zhang, Y. Chen, X. Xu, J. Zhang, G. Xiang, W. He, X. Wang, Angew. Chem. Int. Ed. 53 (2014) 429–433.
[147] Z. Jiang, Z. Li, Z. Qin, H. Sun, X. Jiao, D. Chen, Nanoscale 5 (2013) 11770–11775.
[148] S. Wu, G. Zhuang, J. Wei, Z. Zhuang, Y. Yu, J. Mater. Chem. A 6 (2018) 18234–18241.
[149] W. Li, X. Wu, N. Han, J. Chen, X. Qian, Y. Deng, W. Tang, Y. Chen, Sensors Actuators B Chem. 225 (2016) 158–166.
[150] Y. Fu, W. Wang, J. Wang, X. Li, R. Shi, O. Peng, B.N. Chandrashekar, K. Liu, A. Amini, C. Cheng, J. Mater. Chem. A 7 (2019) 17299–17305.
[151] H. Xu, Y. Yang, X. Yang, J. Cao, W. Liu, Y. Tang, J. Mater. Chem. A 7 (2019) 8284–8291.
[152] X. Jiang, B. Kang, X. Zhang, F. Yan, X. Zhang, F. Cao, Y. Chen, Carbon 225 (2024) 119114.
[153] Z. Zhao, J. Ding, R. Zhu, H. Pang, J. Mater. Chem. A 7 (2019) 15519–15540.
[154] M.-X. Wu, Y. Wang, G. Zhou, X. Liu, ACS Appl. Mater. Interfaces 12 (2020) 54285–54305.
[155] M.Y. Zhang, J.K. Li, R. Wang, S.N. Zhao, S.Q. Zang, T.C. Mak, Adv. Sci. 8 (2021) 2101884.
[156] J.A. Boissonnault, A.G. Wong-Foy, A.J. Matzger, J. Am. Chem. Soc. 139 (2017) 14841–14844.
[157] L. He, Y. Liu, J. Liu, Y. Xiong, J. Zheng, Y. Liu, Z. Tang, Angew. Chem. Int. Ed. 52 (2013) 3741–3745.
[158] Y. Liu, W. Zhang, S. Li, C. Cui, J. Wu, H. Chen, F. Huo, Chem. Mater. 26 (2014) 1119–1125.
[159] W. Wang, B. Xu, X. Pan, J. Zhang, H. Liu, Angew. Chem. 133 (2021) 7881–7887.
[160] J. Li, T. Bao, C. Zhang, H. Song, Y. Zou, L. Yuan, Y. Xi, C. Yu, C. Liu, Chem. Eng. J. 472 (2023) 144926.
[161] J. Li, D. Yan, S. Hou, T. Lu, Y. Yao, D.H. Chua, L. Pan, Chem. Eng. J. 335 (2018) 579–589.
[162] H. Peng, W. Xiong, Z. Yang, Z. Xu, J. Cao, M. Jia, Y. Xiang, J. Hazard. Mater. 432 (2022) 128684.
[163] K. Cao, W. Ye, Y. Zhang, Z. Chen, R. Zhao, W. Xue, Chem. Eng. J. 489 (2024) 151384.
[164] Z. Inonu, S. Keskin, C. Erkey, ACS Appl. Nano Mater. 1 (2018) 5959–5980.
[165] L. Zhu, L. Zong, X. Wu, M. Li, H. Wang, J. You, C. Li, ACS Nano 12 (2018) 4462–4468.
[166] B. Bueken, N. Van Velthoven, T. Willhammar, T. Stassin, I. Stassen, D.A. Keen, G. V. Baron, J.F. Denayer, R. Ameloot, S. Bals, Chem. Sci. 8 (2017) 3939–3948.
[167] F. Wu, Q. Li, Z. Liu, T. Shah, M. Ahmad, Q. Zhang, B. Zhang, Carbon 182 (2021) 484–496.
[168] S. Zhang, L. Li, S. Zhao, Z. Sun, M. Hong, J. Luo, J. Mater. Chem. A 3 (2015) 15764–15768.
[169] S.J. Lee, H. Jang, Nanoscale Adv. 5 (2023) 5165–5213.
[170] J. Zhao, P. Li, Q. Zhang, Z. Ye, Y. Wang, J. Tian, Z. Xu, N. Peng, H. Ren, X. Zhang, Chem. Eng. J. 499 (2024) 156184.
[171] P. Pachfule, D. Shinde, M. Majumder, Q. Xu, Nat. Chem. 8 (2016) 718–724.
[172] B. Wang, M. Zhao, L. Li, Y. Huang, X. Zhang, C. Guo, Z. Zhang, H. Cheng, W. Liu, J. Shang, Natl. Sci. Rev. 7 (2020) 46–52.
[173] T. Kitao, M.W. MacLean, K. Nakata, M. Takayanagi, M. Nagaoka, T. Uemura, J. Am. Chem. Soc. 142 (2020) 5509–5514.
[174] N. Ullah, A. Ramiere, W. Raza, P. Ye, W. Liu, X. Cai, Z. Peng, K.-H. Kim, J. Colloid Interface Sci. 623 (2022) 752–761.
[175] E. Choi, S.J. Hong, Y.J. Kim, S.E. Choi, Y. Choi, J.H. Kim, J. Kang, O. Kwon, K. Eum, B. Han, Adv. Funct. Mater. 31 (2021) 2011146.
[176] R. Wei, Y. Gu, L. Zou, B. Xi, Y. Zhao, Y. Ma, Y. Qian, S. Xiong, Q. Xu, Nano Lett. 20 (2020) 7342–7349.
[177] M. Osada, T. Sasaki, Adv. Mater. 24 (2012) 210–228.
[178] Y.-Z. Li, Z.-H. Fu, G. Xu, Coord. Chem. Rev. 388 (2019) 79–106.
[179] Y. Bai, C. Liu, Y. Shan, T. Chen, Y. Zhao, C. Yu, H. Pang, Adv. Energy Mater. 12 (2022) 2100346.
[180] A. Balapure, J.R. Dutta, R. Ganesan, RSC Appl. Interfaces 1 (2024) 43–69.

[181] T. Zhang, Y. Jin, Y. Shi, M. Li, J. Li, C. Duan, Coord. Chem. Rev. 380 (2019) 201–229.
[182] J. Liu, Y. Liu, Y. Yang, X. Bai, L. Liu, K. Yang, H. Ali, Y. Zhao, B. Wu, B. Sa, ACS Omega 6 (2021) 2956–2965.
[183] A. Hayat, S. Raza, M.A. Amin, Z. Ajmal, M.M. Alghamdi, A.A. El-Zahhar, H. Ali, D. Ghernaout, Y. Al-Hadeethi, M. Sohail, Mater. Sci. Eng. R. Rep. 157 (2024) 100771.
[184] P. Tian, X. He, L. Zhao, W. Li, W. Fang, H. Chen, F. Zhang, Z. Huang, H. Wang, Sol. Energy 188 (2019) 750–759.
[185] A.M. Idris, X. Jiang, J. Tan, Z. Cai, X. Lou, J. Wang, Z. Li, J. Colloid Interface Sci. 607 (2022) 1180–1188.
[186] M. Liu, P. Ye, M. Wang, L. Wang, C. Wu, J. Xu, Y. Chen, J. Environ. Chem. Engineering 10 (2022) 108436.
[187] O. Pluchery, H. Remita, D. Schaming, Gold Bull. 46 (2013) 319–327.
[188] A. Hayat, M. Sohail, T. Taha, S.K.B. Mane, A.G. Al-Sehemi, A.A. Al-Ghamdi, W. Nawawi, A. Palamanit, M.A. Amin, A.M. Fallatah, J. Colloid Interface Sci. 627 (2022) 621–629.
[189] A. Nawaz, S. Goudarzi, M.A. Asghari, S. Pichiah, G.S. Selopal, F. Rosei, Z. M. Wang, H. Zarrin, ACS Appl. Nano Mater. 4 (2021) 11323–11352.
[190] J. Liu, C. Wöll, Chem. Soc. Rev. 46 (2017) 5730–5770.
[191] S. Kumar, R. Sharma, S.J. Borah, A. Gupta, M.K. Gupta, R. Kumar, K.K. Dubey, Y. K. Mishra, V. Kumar, Sustainable Energy & Fuels 7 (2023) 4354–4395.
[192] A. Hayat, H. Ali, Z. Ajmal, A. Alshammari, M.M. Alghamdi, A.A. El-Zahhar, N. Almuqati, M. Sohail, A.M. Abu-Dief, S. Khan, Prog. Mater. Sci. 147 (2024) 101352.
[193] Y. Gao, J. Wu, J. Wang, N. Yan, N. Ma, W. Dai, Microporous Mesoporous Mater. 315 (2021) 110916.
[194] Y. Gao, X. Fang, D. Chen, N. Ma, W. Dai, J. Taiwan Inst. Chem. Eng. 131 (2022) 104146.
[195] P.G. Collins, P. Avouris, Sci. Am. 283 (2000) 62–69.
[196] H. Han, M.R. Khan, I. Ahmad, A. Al-Qattan, I. Ali, M.R. Karim, H. Bayahia, F. S. Khan, Z. Ahmad, S. Ullah, J. Water Process Engineering 61 (2024) 105346.
[197] I. Ahmad, S. Shukrullah, M.Y. Naz, E. Ahmed, M. Ahmad, A.J. Obaidullah, A. Alkhouri, A. Mahal, Y.Y. Ghadi, Mater. Sci. Semicond. Process. 172 (2024) 108088.
[198] A. Hayat, M. Sohail, A.Y.A. Alzahrani, H. Ali, A.M. Abu-Dief, M. Amin, A. M. Alenad, S.R. Al-Mhyawi, Y. Al-Hadeethi, Z. Ajmal, Prog. Mater. Sci. 150 (2024) 101408.
[199] X.-Y. Yang, A. Léonard, A. Lemaire, G. Tian, B.-L. Su, Chem. Commun. 47 (2011) 2763–2786.
[200] A. Hayat, M. Sohail, H. Ali, T. Taha, H. Qazi, N. Ur Rahman, Z. Ajmal, A. Kalam, A.G. Al-Sehemi, S. Wageh, Chem. Rec. 23 (2023) e202200149.
[201] Z.R. Usha, D.M. Babiker, R. Yu, J. Yang, W. Chen, X. Chen, L. Li, J. Membr. Sci. 660 (2022) 120840.
[202] Z. Tao, Y. Zhao, Y. Wang, G. Zhang, C 10 (2024) 69.
[203] H. Ali, Y. Orooji, Z. Ajmal, M. Abboud, A.M. Abu-Dief, K.A.A. Al-Ola, H. M. Hassan, D. Yue, S.-R. Guo, A. Hayat, Coord. Chem. Rev. 526 (2025) 216353.
[204] O. Iqbal, H. Guo, W. Chen, Macromolecules 54 (2021) 8381–8392.
[205] S. Liang, Y. Chen, W. Han, Y. Jiao, W. Li, G. Tian, J. Colloid Interface Sci. 630 (2023) 11–22.
[206] Y. Pi, X. Li, Q. Xia, J. Wu, Z. Li, Y. Li, J. Xiao, Nano Res. 10 (2017) 3543–3556.
[207] S. Zhao, Q. Liang, W. Gao, M. Zhou, C. Yao, S. Xu, Z. Li, Inorg. Chem. 60 (2021) 9762–9772.
[208] N. Cordente, M. Respaud, F. Senocq, M.-J. Casanove, C. Amiens, B. Chaudret, Nano Lett. 1 (2001) 565–568.
[209] B. Zhao, N. Wu, S. Yao, Y. Yao, Y. Lian, B. Li, Z. Zeng, J. Liu, ACS Appl. Nano Mater. 5 (2022) 18697–18707.
[210] R. Chen, Z. Ren, Y. Liang, G. Zhang, T. Dittrich, R. Liu, Y. Liu, Y. Zhao, S. Pang, H. An, Nature 610 (2022) 296–301.
[211] Z.R. Usha, D.M. Babiker, Y. Zhao, X. Chen, L. Li, J. Environ. Chem. Engineering 11 (2023) 110775.
[212] W. Wang, L. Qi, Adv. Funct. Mater. 29 (2019) 1807275.
[213] A. Hayat, M. Sohail, W. Iqbal, T. Taha, A.M. Alenad, A.G. Al-Sehemi, S. Ullah, N. A. Alghamdi, A. Alhadhrami, Z. Ajmal, J. Sci. Adv. Mater. Devices 7 (2022) 100483.
[214] H. Ali, O. Iqbal, S.S. Alarfaji, F. Liu, B. Hong, W. Zhao, D. Yue, Z. Muhammad, Chin. J. Phys. 92 (2024) 90–99.
[215] P. Shandilya, S. Sambyal, R. Sharma, P. Mandyal, B. Fang, J. Hazard. Mater. 428 (2022) 128218.
[216] S. Patial, P. Raizada, V. Hasija, P. Singh, V.K. Thakur, V.-H. Nguyen, Materials Today Energy 19 (2021) 100589.
[217] S. Mansingh, S. Subudhi, S. Sultana, G. Swain, K. Parida, ACS Appl. Nano Mater. 4 (2021) 9635–9652.
[218] H. Yang, J. Tang, Y. Luo, X. Zhan, Z. Liang, L. Jiang, H. Hou, W. Yang, Small 17 (2021) 2102307.
[219] R. Meng, Y. Lu, L. Zou, H. Du, X. Li, B. Zhu, D.K. Macharia, M. Amidpour, Z. Chen, L. Zhang, Desalination 578 (2024) 117455.
[220] S. Ye, I.E. Stewart, Z. Chen, B. Li, A.R. Rathmell, B.J. Wiley, Acc. Chem. Res. 49 (2016) 442–451.
[221] P. Zhang, T. Wang, X. Chang, J. Gong, Acc. Chem. Res. 49 (2016) 911–921.
[222] S.S.A. Shah, T. Najam, M.K. Aslam, M. Ashfaq, M.M. Rahman, K. Wang, P. Tsiakaras, S. Song, Y. Wang, Appl. Catal. B Environ. 268 (2020) 118570.
[223] Z.R. Usha, D.M. Babiker, J. Yang, X. Chen, L. Li, J. Environ. Chem. Engineering 11 (2023) 109670.
[224] S. Hooshmand, P. Kassanos, M. Keshavarz, P. Duru, C.I. Kayalan, İ. Kale, M. K. Bayazit, Sensors 23 (2023) 8648.
[225] H. Ali, S. Ahmed, A. Hsini, S. Kizito, Y. Naciri, R. Djellabi, M. Abid, W. Raza, N. Hassan, M.S.U. Rehman, Arab. J. Chem. 15 (2022) 104209.
[226] L. Weng, L. Su, N. Xu, C. Qian, Q. Cai, R. Chen, Y. Liu, Y. Zhao, F. Xu, H. Ali, Intermetallics 165 (2024) 108132.
[227] Z. Peng, S.C. Abbas, J. Lv, R. Yang, M. Wu, Y. Wang, Int. J. Hydrog. Energy 44 (2019) 2446–2453.
[228] Z. Hou, L. Wang, G. Liu, Y. Wang, Y. Wang, Y. Zhang, X. Wu, N. Li, J. Alloys Compd. 973 (2024) 172940.
[229] H. Wu, X.Y. Kong, X. Wen, S.P. Chai, E.C. Lovell, J. Tang, Y.H. Ng, Angew. Chem. Int. Ed. 60 (2021) 8455–8459.
[230] J.F. Banfield, H. Zhang, Rev. Mineral. Geochem. 44 (2001) 1–58.
[231] P. Hirschle, T. Preiß, F. Auras, A. Pick, J. Völkner, D. Valdepérez, G. Witte, W. J. Parak, J.O. Rädler, S. Wuttke, CrystEngComm 18 (2016) 4359–4368.
[232] M. Lismont, L. Dreesen, S. Wuttke, Adv. Funct. Mater. 27 (2017) 1606314.
[233] K. Mondal, A. Sharma, RSC Adv. 6 (2016) 83589–83612.
[234] M. Sayed, J. Yu, G. Liu, M. Jaroniec, Chem. Rev. 122 (2022) 10484–10537.
[235] A. Zada, P. Muhammad, W. Ahmad, Z. Hussain, S. Ali, M. Khan, Q. Khan, M. Maqbool, Adv. Funct. Mater. 30 (2020) 1906744.
[236] A.A. Ansari, M. Sillanpää, Renew. Sust. Energ. Rev. 151 (2021) 111631.
[237] H. Ali, R. Chen, H. Chen, Y. Zhao, P. Zhao, S. Yang, B. Wu, J. Wen, C. Zhang, L. Weng, Mater. Today Commun. 33 (2022) 104447.
[238] Z. Ajmal, S. Kizito, B. Alalwan, A. Kumar, A. El-Jery, G.A. Ashraf, I. Hussain, H. Ali, A. Alshammari, N. Almuqati, Mater. Today Chem. 39 (2024) 102140.
[239] X.-M. Cheng, P. Wang, S.-Q. Wang, J. Zhao, W.-Y. Sun, ACS Appl. Mater. Interfaces 14 (2022) 32350–32359.
[240] P. Zhu, C. Feng, Q. Liang, M. Zhou, Z. Li, S. Xu, Ceram. Int. 49 (2023) 20706–20714.
[241] D. Sun, D.-P. Kim, ACS Appl. Mater. Interfaces 12 (2020) 20589–20595.
[242] M.A. Reed, Sci. Am. 268 (1993) 118–123.
[243] J. Du, F. Shi, K. Wang, Q. Han, Y. Shi, W. Zhang, Y. Gao, B. Dong, L. Wang, L. Xu, TrAC Trends Anal. Chem. 175 (2024) 117707.
[244] Y. Wang, L. Wang, Z. Liu, E. Ye, J.H. Pan, G. Guan, Z. Li, Appl. Catal. A Gen. 644 (2022) 118836.
[245] H. Ali, R. Chen, B. Wu, T. Xie, L. Weng, J. Wen, Q. Yao, L. Su, Y. Zhao, P. Zhao, Arab. J. Chem. 15 (2022) 104278.
[246] Z. Ajmal, H. Ali, S. Ullah, A. Kumar, M. Abboud, H. Gul, Y. Al-hadeethi, A. S. Alshammari, N. Almuqati, G.A. Ashraf, Fuel 367 (2024) 131295.
[247] A.E. Stone, S. Irgen-Gioro, R. López-Arteaga, J.T. Hupp, E.A. Weiss, Chem. Mater. 34 (2022) 1921–1929.
[248] H. Ma, T. Wang, Y. Xu, W. Shi, R. Ma, Z. Xia, Q. Yang, G. Xie, S. Chen, Appl. Catal. B: Environ. and Energy 349 (2024) 123857.
[249] J. Qin, B. Liu, K.-H. Lam, S. Song, X. Li, X. Hu, ACS Sustain. Chem. Eng. 8 (2020) 17791–17799.
[250] L. Ding, Y. Ding, F. Bai, G. Chen, S. Zhang, X. Yang, H. Li, X. Wang, Inorg. Chem. 62 (2023) 2289–2303.
[251] S. Simov, J. Mater. Sci. 11 (1976) 2319–2332.
[252] X. Wang, J. Feng, Y. Bai, Q. Zhang, Y. Yin, Chem. Rev. 116 (2016) 10983–11060.
[253] G. Prieto, H. Tüysüz, N. Duyckaerts, J. Knossalla, G.-H. Wang, F. Schüth, Chem. Rev. 116 (2016) 14056–14119.
[254] I. Uddin, H. Ali, A.G. Al-Sehemi, S. Muhammad, N. Hamad, T. Taha, H.S. AlSalem, A.M. Alenad, A. Palamanit, A. Hayat, S. Afr. J. Bot. 149 (2022) 109–116.
[255] B. Li, H.C. Zeng, Adv. Mater. 31 (2019) 1801104.
[256] Z. Ajmal, X. Tu, W. Abbas, E.H. Ibrahim, H. Ali, I. Hussain, M.K. Al-Muhana, M. Khered, A. Iqbal, S. Rahaman, Fuel 378 (2024) 132903.
[257] H. Ali, Y. Orooji, A.Y.A. Alzahrani, H.M. Hassan, Z. Ajmal, D. Yue, A. Hayat, ACS Nano 19 (8) (2025) 7482–7545.
[258] H. Fan, Y. Jin, K. Liu, W. Liu, Adv. Sci. 9 (2022) 2104579.
[259] C. Han, X. Zhang, S. Huang, Y. Hu, Z. Yang, T.T. Li, Q. Li, J. Qian, Adv. Sci. 10 (2023) 2300797.
[260] M.-L. Xu, X.-J. Jiang, J.-R. Li, F.-J. Wang, K. Li, X. Cheng, ACS Appl. Mater. Interfaces 13 (2021) 56171–56180.
[261] G. Libben, J. Neurolinguistics 8 (1994) 49–55.
[262] M.Y. Tsang, A. Sinelshchikova, O. Zaremba, F. Schoefbeck, A.D. Balsa, M. R. Reithofer, S. Wuttke, J.M. Chin, Adv. Funct. Mater. 34 (2024) 2308376.
[263] W. Zhang, R. Taheri-Ledari, M. Saeidirad, F.S. Qazi, A. Kashtiaray, F. Ganjali, Y. Tian, A. Maleki, J. Environ. Chem. Engineering 10 (2022) 108836.
[264] Z.R. Usha, O. Iqbal, M.A. Aslam, S. Ali, C. Liu, N. Li, S. Zhang, Z. Wang, Int. J. Biol. Macromol. 252 (2023) 126375.
[265] M.J. Muñoz-Batista, A. Kubacka, A.B. Hungría, M. Fernández-García, J. Catal. 330 (2015) 154–166.
[266] M. Sohail, U. Anwar, T. Taha, H. Qazi, A.G. Al-Sehemi, S. Ullah, H. Algarni, I. Ahmed, M.A. Amin, A. Palamanit, Arab. J. Chem. 15 (2022) 104070.
[267] Q. Xiong, Y. Chen, D. Yang, K. Wang, Y. Wang, J. Yang, L. Li, J. Li, Mater. Chem. Frontiers 6 (2022) 2944–2967.
[268] A. Hayat, Z. Ajmal, A.Y.A. Alzahrani, S.B. Moussa, M. Khered, N. Almuqati, A. Alshammari, Y. Al-Hadeethi, H. Ali, Y. Orooji, Coord. Chem. Rev. 522 (2025) 216218.
[269] C. Rao, L. Zhou, Y. Pan, C. Lu, X. Qin, H. Sakiyama, M. Muddassir, J. Liu, J. Alloys Compd. 897 (2022) 163178.
[270] H. Jiang, M. Xu, X. Zhao, H. Wang, P. Huo, J. Environ. Chem. Engineering 11 (2023) 109504.
[271] S. Zhang, M. Du, Z. Xing, Z. Li, K. Pan, W. Zhou, Appl. Catal. B Environ. 262 (2020) 118202.
[272] F. Ma, Q. Li, J. Huang, J. Li, J. Cryst. Growth 310 (2008) 3522–3527.
[273] B. Wu, Y. Zhao, H. Ali, R. Chen, H. Chen, J. Wen, Y. Liu, L. Liu, K. Yang, L. Zhang, Intermetallics 144 (2022) 107489.

[274] A. Hayat, Z. Ajmal, A.Y.A. Alzahrani, M.H.A. Mughram, A.M. Abu-Dief, A.-F. Rawan, A.M. Alenad, Y. Al-Hadeethi, H. Ali, S.P. Vattikuti, Mater. Today 83 (2025) 331–354.
[275] D. Li, Q. Wen, C. Gao, Y. Zhang, J. Zhou, S. Liu, F. Song, K. Wang, Chem. Eng. J. 498 (2024) 155079.
[276] K. Hormann, T. Müllner, S. Bruns, A. Höltzel, U. Tallarek, J. Chromatogr. A 1222 (2012) 46–58.
[277] I. Nischang, J. Chromatogr. A 1287 (2013) 39–58.
[278] S. Bruns, T. Müllner, M. Kollmann, J. Schachtner, A. Höltzel, U. Tallarek, Anal. Chem. 82 (2010) 6569–6575.
[279] Z. Ajmal, T. Taha, M.A. Amin, A. Palamanit, W. Nawawi, A. Kalam, A.G. Al-Sehemi, H. Algarni, A. Qadeer, H. Ali, J. Mol. Liq. 368 (2022) 120617.
[280] V. Ntouros, I. Kousis, A.L. Pisello, M.N. Assimakopoulos, Energies 15 (2022) 1489.
[281] H. Ali, O. Iqbal, M. Sadiq, J.U. Hassan, B. Al Alwan, A. El Jery, A.M. Abu-Dief, R. El-Kasaby, A. Hayat, D. Yue, Renew. Sust. Energ. Rev. 215 (2025) 115570.
[282] H.Y. Niu, L.Q. Cao, X.L. Yang, K.N. Liu, L. Liu, J.D. Wang, Polym. Adv. Technol. 32 (2021) 3194–3204.
[283] T. Tian, J. Xu, A. Abdolazizi, C. Ji, J. Hou, D. Riley, C. Yan, M. Ryan, F. Xie, C. Petit, Mater. Today Nano 21 (2023) 100293.
[284] C. Li, X. Fang, F. Zong, M. Xiang, R. Liu, J. Duan, Colloids Surf. A Physicochem. Eng. Asp. 679 (2023) 132597.
[285] Y. Xia, W. Li, C.M. Cobley, J. Chen, X. Xia, Q. Zhang, M. Yang, E.C. Cho, P. K. Brown, Acc. Chem. Res. 44 (2011) 914–924.
[286] Y. He, W. Zhang, T. Guo, G. Zhang, W. Qin, L. Zhang, C. Wang, W. Zhu, M. Yang, X. Hu, Acta Pharm. Sin. B 9 (2019) 97–106.
[287] H. Ali, O. Iqbal, M. Sadiq, Y. Cheng, X. Yan, B. Al Alwan, A. El Jery, H. Ur Rahman, Y. Qian, A. Hayat, Nano Mater. Sci. (2025), https://doi.org/10.1016/j.nanoms.2024.08.008.
[288] L. Zhang, Y. Chen, R. Shi, T. Kang, G. Pang, B. Wang, Y. Zhao, X. Zeng, C. Zou, P. Wu, Inorg. Chem. Commun. 96 (2018) 20–23.
[289] A. Hayat, M. Sohail, A. El Jery, K.M. Al-Zaydi, K.F. Alshammari, J. Khan, H. Ali, Z. Ajmal, T. Taha, I. Ud Din, Chem. Rec. 23 (2023) e202200171.
[290] Q. Zhang, Y. Chen, X. Yu, Y. Yin, Y. Ru, G. Tian, J. Alloys Compd. 983 (2024) 173735.
[291] Y. Su, Z. Song, W. Zhu, Q. Mu, X. Yuan, Y. Lian, H. Cheng, Z. Deng, M. Chen, W. Yin, ACS Catal. 11 (2020) 345–354.
[292] P. Varma, M. Gopannagari, K.A.J. Reddy, T.K. Kim, D.A. Reddy, ChemCatChem 15 (2023) e202300316.
[293] D. Bochicchio, R. Ferrando, Physical Review B—Condensed Matter and Materials Physics 87 (2013) 165435.
[294] Y. Liu, Z. Tang, Adv. Mater. 25 (2013) 5819–5825.
[295] D. Wang, T. Li, Acc. Chem. Res. 56 (2023) 462–474.
[296] H. Ali, Z. Ajmal, I. Boukhris, A.M. Alenad, M. Al-Buriahi, A.M. Abu-Dief, N. S. Alsaiari, A. Hayat, H.M. Hassan, Y. Liang, Int. J. Hydrog. Energy 100 (2025) 79–128.
[297] A. Hayat, M. Sohail, A. El Jery, K.M. Al-Zaydi, S. Raza, H. Ali, Y. Al-Hadeethi, T. Taha, I.U. Din, M.A. Khan, Mater. Today 64 (2023) 180–208.
[298] Z.R. Usha, D.M. Babiker, X. Chen, L. Li, Surf. Coat. Technol. 494 (2024) 131360.
[299] Q. Liang, W. Gao, C. Liu, S. Xu, Z. Li, J. Hazard. Mater. 392 (2020) 122500.
[300] X. Zhao, Y. Zhou, Q. Liang, M. Zhou, Z. Li, S. Xu, Sep. Purif. Technol. 279 (2021) 119765.
[301] Q. Cao, Y. Xiao, N. Liu, R. Huang, C. Ye, C. Huang, H. Liu, G. Han, L. Wu, Sensors Actuators B Chem. 329 (2021) 129133.
[302] Z. Ajmal, A. Hayat, A. Qadeer, Y. Zhao, E.H. Ibrahim, M. Ul Haq, K. Iqbal, M. Imran, M. Kuku, I. Hussain, Coord. Chem. Rev. 523 (2025) 216226.
[303] S. Xiong, R. Tang, D. Gong, Y. Deng, C. Zhang, J. Zheng, L. Su, L. Yang, C. Liao, Appl. Mater. Today 21 (2020) 100798.
[304] A. Hayat, M. Sohail, A. El Jery, K.M. Al-Zaydi, S. Raza, H. Ali, Z. Ajmal, A. Zada, T. Taha, I.U. Din, Energy Storage Mater. 59 (2023) 102780.
[305] Z.R. Usha, C. Liu, S. Zhang, Z. Wang, Desalination 599 (2024) 118461.
[306] A. Zhou, Y. Dou, J. Zhou, J.R. Li, ChemSusChem 13 (2020) 205–211.
[307] Z. Lv, X. Tan, C. Wang, A. Alsaedi, T. Hayat, C. Chen, Chem. Eng. J. 389 (2020) 123428.
[308] S. Zhang, H. Gao, X. Xu, R. Cao, H. Yang, X. Xu, J. Li, Chem. Eng. J. 381 (2020) 122670.
[309] T. Guo, H. Mashhadimoslem, L. Choopani, M.M. Salehi, A. Maleki, A. Elkamel, A. Yu, Q. Zhang, J. Song, Y. Jin, Small 20 (2024) 2402942.
[310] M. Shiri, M. Hosseinzadeh, S. Shiri, S. Javanshir, Sci. Rep. 14 (2024) 15623.
[311] P. Cheng, C. Wang, Y.V. Kaneti, M. Eguchi, J. Lin, Y. Yamauchi, J. Na, Langmuir 36 (2020) 4231–4249.
[312] R. Chen, T. Xie, B. Wu, L. Weng, H. Ali, S. Yang, Y. Zhao, P. Zhao, C. Zhang, R. Cao, J. Alloys Compd. 935 (2023) 168016.
[313] M.Z.A. Ebrahim, V. Rahmanian, M. Abdelmigeed, T. Pirzada, S.A. Khan, Small Methods 8 (12) (2024) 2400596.
[314] X. He, L. Wang, S. Sun, X. Yang, H. Tian, Z. Xia, X. Li, X. Yan, X. Pu, Z. Jiao, J. Alloys Compd. 946 (2023) 169391.
[315] M. Song, J. Li, M. Xu, Z. Xu, X. Song, X. Liu, J. Zhang, Y. Yang, X. Xie, W. Zhou, J. Colloid Interface Sci. 668 (2024) 471–483.
[316] Y. Li, M. Lu, Y. Wu, H. Xu, J. Gao, J. Yao, Adv. Mater. Interfaces 6 (2019) 1900290.
[317] Y. Li, M. Lu, P. He, Y. Wu, J. Wang, D. Chen, H. Xu, J. Gao, J. Yao, Chem.–An Asian J. 14 (2019) 1590–1594.
[318] Y. Li, M. Lu, Y. Wu, Q. Ji, H. Xu, J. Gao, G. Qian, Q. Zhang, J. Mater. Chem. A 8 (2020) 18215–18219.
[319] O. Iqbal, H. Ali, N. Li, A.I. Al-Sulami, K.F. Alshammari, H.S. Abd-Rabboh, Y. Al-Hadeethi, I.U. Din, A.I. Alharthi, R. Altamimi, Materials Today Phys. 34 (2023) 101080.
[320] Y. Li, S. Zheng, S. Hou, T. Chen, Y. Bai, M. Zhang, D. Zhou, S. Yang, H. Xu, G. Zhang, J. Hazard. Mater. 460 (2023) 132376.
[321] S. Zhao, Y. Long, Y. Su, S. Wang, Z. Zhang, X. Zhang, Small 17 (2021) 2101393.
[322] Y.L. Liu, X.Y. Liu, L. Feng, L.X. Shao, S.J. Li, J. Tang, H. Cheng, Z. Chen, R. Huang, H.C. Xu, ChemSusChem 15 (2022) e202102603.
[323] Y.S. Wei, L. Zou, H.F. Wang, Y. Wang, Q. Xu, Adv. Energy Mater. 12 (2022) 2003970.
[324] Z. Ajmal, A. Qadeer, U. Khan, M.B. Hussain, M. Irfan, R. Mehmood, M. Abid, R. Djellabi, A. Kumar, H. Ali, Mater. Today Chem. 27 (2023) 101238.
[325] Z. Ma, B. Guan, J. Guo, Y. Chen, J. Chen, H. Dang, C. Zhu, L. Chen, K. Shu, K. Shi, Ind. Eng. Chem. Res. 62 (2023) 17658–17670.
[326] Y. Zhao, R. Chen, J. Luo, J. Zhu, Y. Wu, P. Qiao, W. Yan, Y. Pan, J. Zhu, X. Zu, ChemPhysChem 25 (2024) e202300368.
[327] L. Li, Y. Zhao, Q. Wang, Z.-Y. Liu, X.-G. Wang, E.-C. Yang, X.-J. Zhao, Inorganic Chem. Frontiers 8 (2021) 3556–3565.
[328] S. Soni, S. Teli, P. Teli, S. Agarwal, Sustain. Chem. Pharm. 41 (2024) 101693.
[329] S. Wang, J. Zhao, J. Phys. D. Appl. Phys. 58 (2025) 155503.
[330] I. Bertuol, L. Jiménez-Rodríguez, R.R. Solís, P. Canton, M. Selva, M.C. de Hoces, A. Perosa, D. Rodriguez-Padron, M.J. Muñoz-Batista, Sustainable Energy Fuel 9 (2025) 2031–2044.
[331] W. Iqbal, R. Liu, Y. Mao, M. Waqas, M. Rauf, C. Qin, Mater. Today Chem. 41 (2024) 102315.
[332] T. Wang, X. Liu, Q. Men, C. Ma, Y. Liu, Z. Liu, P. Huo, C. Li, Y. Yan, J. Mol. Liq. 268 (2018) 561–568.
[333] K. Pandi, K.P. Kangeyan, S.K. Lakhera, T.S. Kiong, N. Bernaurdshaw, Mater. Today Sustainability 27 (2024) 100942.
[334] S. Horike, D. Umeyama, S. Kitagawa, Acc. Chem. Res. 46 (2013) 2376–2384.
[335] T. Nezakati, A. Seifalian, A. Tan, A.M. Seifalian, Chem. Rev. 118 (2018) 6766–6843.
[336] S.I. Cho, S.B. Lee, Acc. Chem. Res. 41 (2008) 699–707.
[337] L. Sun, M.G. Campbell, M. Dincă, Angew. Chem. Int. Ed. 55 (2016) 3566–3579.
[338] R. Balint, N.J. Cassidy, S.H. Cartmell, Acta Biomater. 10 (2014) 2341–2353.
[339] S. Ravati, B.D. Favis, Polymer 52 (2011) 718–731.
[340] J. Kim, J. Lee, J. You, M.-S. Park, M.S. Al Hossain, Y. Yamauchi, J.H. Kim, Materials Horizons 3 (2016) 517–535.
[341] M. Yanılmaz, A.S. Sarac, Text. Res. J. 84 (2014) 1325–1342.
[342] Y. Shi, G. Yu, Chem. Mater. 28 (2016) 2466–2477.
[343] G. Schopf, G. Kossmehl, Polythiophenes-electrically conductive polymers, Springer, 1997.
[344] Y. Huang, S. Kormakov, X. He, X. Gao, X. Zheng, Y. Liu, J. Sun, D. Wu, Polymers 11 (2019) 187.
[345] C.-W. Liew, S. Ramesh, A. Arof, Int. J. Hydrog. Energy 40 (2015) 852–862.
[346] Q. Li, Y. Li, X. Zhang, S.B. Chikkannanavar, Y. Zhao, A.M. Dangelewicz, L. Zheng, S.K. Doorn, Q. Jia, D.E. Peterson, Adv. Mater. 19 (2007) 3358–3363.
[347] M. Miao, Carbon 49 (2011) 3755–3761.
[348] J.L. Blackburn, T.M. Barnes, M.C. Beard, Y.-H. Kim, R.C. Tenent, T.J. McDonald, B. To, T.J. Coutts, M.J. Heben, ACS Nano 2 (2008) 1266–1274.
[349] X. Zhang, W. Lu, G. Zhou, Q. Li, Adv. Mater. 32 (2020) 1902028.
[350] H. Liu, J. Gao, W. Huang, K. Dai, G. Zheng, C. Liu, C. Shen, X. Yan, J. Guo, Z. Guo, Nanoscale 8 (2016) 12977–12989.
[351] H. Wang, F. Meng, F. Huang, C. Jing, Y. Li, W. Wei, Z. Zhou, ACS Appl. Mater. Interfaces 11 (2019) 12142–12153.
[352] A.H.A. Hoseini, M. Arjmand, U. Sundararaj, M. Trifkovic, Mater. Des. 125 (2017) 126–134.
[353] T. Asefa, Acc. Chem. Res. 49 (2016) 1873–1883.
[354] C. Hu, Y. Lin, J.W. Connell, H.M. Cheng, Y. Gogotsi, M.M. Titirici, L. Dai, Adv. Mater. 31 (2019) 1806128.
[355] H. Lu, J. Tournet, K. Dastafkan, Y. Liu, Y.H. Ng, S.K. Karuturi, C. Zhao, Z. Yin, Chem. Rev. 121 (2021) 10271–10366.
[356] X. Liu, L. Dai, Nature Revi. Mater. 1 (2016) 1–12.
[357] J.W.D. Ng, M. Tang, T.F. Jaramillo, Energy Environ. Sci. 7 (2014) 2017–2024.
[358] C. Li, Y. Xu, W. Tu, G. Chen, R. Xu, Green Chem. 19 (2017) 882–899.
[359] C. Hu, Y. Xiao, Y. Zou, L. Dai, Electrochem. Energy Rev. 1 (2018) 84–112.
[360] C. Ding, L. Chen, Z. Ni, Z. Chen, J. Li, L. Chen, F. Su, Y. Huang, ACS Appl. Nano Mater. 4 (2021) 13132–13139.
[361] Y. Lu, B. Yan, J.-L. Liu, Chem. Commun. 50 (2014) 9969–9972.
[362] M. Wang, G. Liang, M. Wang, M. Hu, L. Zhu, Z. Li, Z. Zhang, L. He, M. Du, Chem. Eng. J. 448 (2022) 137779.
[363] Q. Ye, T. Dai, J. Shen, Q. Xu, X. Hu, Y. Shu, J. Anal. Test. 7 (2023) 16–24.
[364] B. Li, M. Zhou, C. Zhao, L. Xiao, T. Qi, H. Xu, L. Guo, G. Ning, X. Lu, K. Zhu, J. Anal. Test. (2024) 1–11.
[365] X. Lu, C. Yao, L. Sun, Z. Li, Biosens. Bioelectron. 203 (2022) 114041.
[366] H.A. Murthy, A.N. Wagassa, C. Ravikumar, H. Nagaswarupa, Functionalized metal and metal oxide nanomaterial-based electrochemical sensors, Functionalized Nanomaterial-Based Electrochemical Sensors, Elsevier, in, 2022, pp. 369–392.
[367] M. Shafi, M. Zhou, P. Duan, W. Liu, W. Zhang, Z. Zha, J. Gao, S. Wali, S. Jiang, B. Man, Sensors Actuators B Chem. 356 (2022) 131360.
[368] S. Andleeb, A.K. Singh, Potential Applications of Graphene, in: Carrier Modulation in Graphene and Its Applications, Jenny Stanford Publishing, 2021, pp. 83–128.
[369] S. Fajal, S. Dutta, S.K. Ghosh, Materials Horizons 10 (2023) 4083–4138.
[370] Z. Zhang, J. Jia, Y. Zhi, S. Ma, X. Liu, Chem. Soc. Rev. 51 (2022) 2444–2490.

[371] A. Giri, Y. Khakre, G. Shreeraj, T.K. Dutta, S. Kundu, A. Patra, J. Mater. Chem. A 10 (2022) 17077–17121.
[372] W. Song, Y. Zhang, C.H. Tran, H.K. Choi, D.-G. Yu, I. Kim, Prog. Polym. Sci. 142 (2023) 101691.
[373] D. Luo, M. Li, Q. Ma, G. Wen, H. Dou, B. Ren, Y. Liu, X. Wang, L. Shui, Z. Chen, Chem. Soc. Rev. 51 (2022) 2917–2938.
[374] P. Srinivasan, K. Dhingra, K. Kailasam, J. Mater. Chem. A 11 (2023) 17418–17451.
[375] R. Shorten, F. Wirth, O. Mason, K. Wulff, C. King, SIAM Rev. 49 (2007) 545–592.
[376] A.H. Fathima, K. Palanisamy, Renew. Sust. Energ. Rev. 45 (2015) 431–446.
[377] F.W. Allendorf, R.F. Leary, P. Spruell, J.K. Wenburg, Trends Ecol. Evol. 16 (2001) 613–622.
[378] R. Goebel, R.G. Sanfelice, A.R. Teel, IEEE Control. Syst. Mag. 29 (2009) 28–93.
[379] F. Borrelli, A. Bemporad, M. Morari, Predictive control for linear and hybrid systems, Cambridge University Press, 2017.
[380] L. Tao, Y. Zhou, L. Zicun, Chin. J. Aeronaut. 32 (2019) 1488–1503.
[381] J. Huang, S.R. Turner, Polym. Rev. 58 (2018) 1–41.
[382] Y. Gu, S.U. Son, T. Li, B. Tan, Adv. Funct. Mater. 31 (2021) 2008265.
[383] L. Tan, B. Tan, Chem. Soc. Rev. 46 (2017) 3322–3356.
[384] R. Kurihara, I. Maruyama, Cem. Concr. Res. 157 (2022) 106805.
[385] F. Wang, H. Liu, J. Ou, W. Li, Constr. Build. Mater. 278 (2021) 122385.
[386] Y. Qing, Z. Zenan, K. Deyu, C. Rongshen, Constr. Build. Mater. 21 (2007) 539–545.
[387] K. Somlo, B.H. Frodal, C. Funch, K. Poulios, G. Winther, O.S. Hopperstad, T. Børvik, C. Niordson, European J. Mechanics-A/Solids 94 (2022) 104506.
[388] J. Yang, Y. Li, Y. Zheng, Y. Xu, Z. Zheng, X. Chen, W. Liu, Small 15 (2019) 1902826.
[389] P. Liu, X. Chen, Y. Li, P. Cheng, Z. Tang, J. Lv, W. Aftab, G. Wang, ACS Nano 16 (2022) 15586–15626.
[390] Y. Si, J. Yu, X. Tang, J. Ge, B. Ding, Nat. Commun. 5 (2014) 5802.
[391] Z. Sheng, Z. Liu, Y. Hou, H. Jiang, Y. Li, G. Li, X. Zhang, Adv. Sci. 10 (2023) 2205762.
[392] Y. Chen, L. Zhang, Y. Yang, B. Pang, W. Xu, G. Duan, S. Jiang, K. Zhang, Adv. Mater. 33 (2021) 2005569.
[393] W. Tian, H. Zhang, X. Duan, H. Sun, G. Shao, S. Wang, Adv. Funct. Mater. 30 (2020) 1909265.
[394] H. Liu, X. Liu, W. Li, X. Guo, Y. Wang, G. Wang, D. Zhao, Adv. Energy Mater. 7 (2017) 1700283.
[395] L. Yao, Q. Wu, P. Zhang, J. Zhang, D. Wang, Y. Li, X. Ren, H. Mi, L. Deng, Z. Zheng, Adv. Mater. 30 (2018) 1706054.
[396] L.L. Zhang, Y. Gu, X. Zhao, J. Mater. Chem. A 1 (2013) 9395–9408.
[397] L. Zhang, X. Wang, R. Wang, M. Hong, Chem. Mater. 27 (2015) 7610–7618.
[398] J. Wu, F. Xu, S. Li, P. Ma, X. Zhang, Q. Liu, R. Fu, D. Wu, Adv. Mater. 31 (2019) 1802922.
[399] X. Zheng, J. Luo, W. Lv, D.W. Wang, Q.H. Yang, Adv. Mater. 27 (2015) 5388–5395.
[400] Q. Wang, D. O'Hare, Chem. Rev. 112 (2012) 4124–4155.
[401] W. Cao, T. Guo, J. Wang, G. Xu, J. Jiang, D. Liu, Coord. Chem. Rev. 497 (2023) 215450.
[402] X. Ju, Z. Yang, X. Duan, H. Zhu, B. Cui, J. Wang, Z. Du, Y. Liu, Y. Zheng, D. Wang, Appl. Mater. Today 34 (2023) 101908.
[403] G. Fan, F. Li, D.G. Evans, X. Duan, Chem. Soc. Rev. 43 (2014) 7040–7066.
[404] X. Zhang, J. Lu, J. Zhang, Chem. Mater. 26 (2014) 4023–4029.
[405] S. Ni, S. Tan, Q. An, L. Mai, J. Energy Chem. 44 (2020) 73–89.
[406] C. Li, S. Deng, W. Feng, Y. Cao, J. Bai, X. Tian, Y. Dong, F. Xia, Small 19 (2023) 2300066.
[407] J. Fonseca, T. Gong, L. Jiao, H.-L. Jiang, J. Mater. Chem. A 9 (2021) 10562–10611.
[408] G. Ding, J. Zhao, K. Zhou, Q. Zheng, S.-T. Han, X. Peng, Y. Zhou, Chem. Soc. Rev. 52 (2023) 7071–7136.
[409] J.-H. Lee, S.-J. Park, Carbon 163 (2020) 1–18.
[410] J. Biener, M. Stadermann, M. Suss, M.A. Worsley, M.M. Biener, K.A. Rose, T. F. Baumann, Energy Environ. Sci. 4 (2011) 656–667.
[411] J. Dong, J. Zeng, B. Wang, Z. Cheng, J. Xu, W. Gao, K. Chen, ACS Appl. Mater. Interfaces 13 (2021) 15910–15924.
[412] S. Nardecchia, D. Carriazo, M.L. Ferrer, M.C. Gutiérrez, F. del Monte, Chem. Soc. Rev. 42 (2013) 794–830.
[413] N. Grassie, G. Scott, Polymer degradation and stabilisation, CUP Archive, 1988.
[414] S. Herminghaus, Nat. Mater. 2 (2003) 11–12.
[415] G. Reiter, P. Auroy, L. Auvray, Macromolecules 29 (1996) 2150–2157.
[416] G. Scott, Why degradable polymers?, in: Degradable polymers: principles and applications, Springer, 2010, pp. 1–15.
[417] H. Li, T. Lee, T. Dziubla, F. Pi, S. Guo, J. Xu, C. Li, F. Haque, X.-J. Liang, P. Guo, Nano Today 10 (2015) 631–655.
[418] C. Huang, X. Jia, R. Tian, Z. Wang, H. Song, Chem. Eng. J. 507 (2025) 160697.
[419] Y. Lin, J.W. Connell, Nanoscale 4 (2012) 6908–6939.
[420] H. Zeng, C. Zhi, Z. Zhang, X. Wei, X. Wang, W. Guo, Y. Bando, D. Golberg, Nano Lett. 10 (2010) 5049–5055.
[421] L. Feng, P. Wei, Q. Song, J. Zhang, Q. Fu, X. Jia, J. Yang, D. Shao, Y. Li, S. Wang, ACS Nano 16 (2022) 17049–17061.
[422] J. Wang, D. Lu, W. Xuan, Y. Ji, R. Chen, S. Li, W. Li, W. Chen, S. Tang, G. Zheng, J. Adv. Ceram. 13 (2024).
[423] C. Chen, Y. Hang, H.S. Wang, Y. Wang, X. Wang, C. Jiang, Y. Feng, C. Liu, E. Janzen, J.H. Edgar, Adv. Mater. 35 (2023) 2303198.
[424] Z. Chen, A. Narita, K. Müllen, Adv. Mater. 32 (2020) 2001893.